

**SCATTERING OF ULTRASONICS WAVES  
BY FLAWS IN COMPOSITE MATERIALS :  
AN FEM ANALYSIS**

*by*

**IDAPALAPATI SRIDHAR**

**ME**

**1993**

**M**

**SRI**

**SCA**



**DEPARTMENT OF MECHANICAL ENGINEERING**

**INDIAN INSTITUTE OF TECHNOLOGY, KANPUR**

**JULY, 1993**

**SCATTERING OF ULTRASONIC WAVES  
BY FLAWS IN COMPOSITE MATERIALS :  
AN FEM ANALYSIS**

*A Thesis Submitted  
in Partial Fulfilment of the Requirements  
for the Degree of*

**MASTER OF TECHNOLOGY**

By

**IDAPALAPATI SRIDHAR**

to the

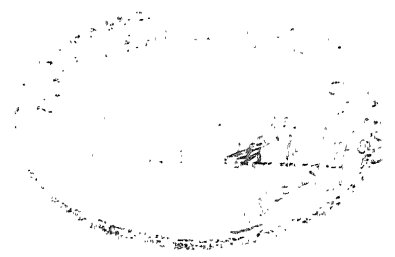
**DEPARTMENT OF MECHANICAL ENGINEERING  
INDIAN INSTITUTE OF TECHNOLOGY KANPUR**

**JULY, 1993**

ME-PH-D  
PH-S

ME-1995-M-SRI-SCA

18 AUG 1993 | ME  
CENTRAL LIBRARY  
I I T. KANPUR  
Acc. No. A1.16267



## CERTIFICATE

*It is certified that the work contained in the thesis entitled **SCATTERING OF ULTRASONIC WAVES BY FLAWS IN COMPOSITE MATERIALS AN FEM ANALYSIS** by IDAPALAPATI SRIDHAR has been carried out under my supervision and that this work has not been submitted elsewhere for a degree.*

*NN Kishore*  
N. N. KISHORE *6/7*

Professor  
Dept. of Mechanical Engineering  
Indian Institute of Technology  
Kanpur-208016, INDIA

JULY, 1993





Let noble thoughts come to us from every side !

- Rigveda.

*This small piece of work  
is dedicated to  
my beloved parents  
Pmt. & Pri. Sivaramaiah Eswaramma.*

## A C K N O W L E D G E M E N T

It gives me profound pleasure to express my deep gratitude to my supervisor Dr. N. N. Kishore, who introduced me to this fascinating area of wave propagation, in particular to Ultrasonic NDE & for his expert guidance and wise counsel, without which this work couldn't have realised. I wish that the stimulating discussions I had with him will guide me in future course.


I wish to place on record my sincere thanks to Professors who taught me well in the course work.

I am thankful to Venkat, Pradhan, Subbarao, Verma, PVM Rao, Jaleel, Ramakrishna, Sagar, Sudhakar and Srinivas for their timely help. I am fortunate to have the association of a host of friends specially Venkatesh, Chandra Sekhar(1,2 &3), Ravindra, Prasad(S,VD), Amit, Samuel, Gamar, Dixit, Ramesh, Sharma, Gopal who made my stay here a memorable one. I acknowledge every help I received from SMD friends and ESA lab mates.

I am grateful to Mrs Kishore and Mrs Subbarao for their encouragement and for providing a home away from home.

I will appreciate my dear friends Raghava, Rao (KV, GV, ES), Murthy, Krishna Sastri, Siva Ram, Bhavani, Nani, Sagi for their encouragement through their letters.

Words are failing in me to put on my sincere gratitude to my parents, brothers Kamala Prasad and Pavani Sudhakar, and sister Prabhavati Satyam for their constant support, love and understanding. Not only their words but actions gave me a lot of relief. My special thanks to Dr. G. Anasurya for her timely help. I like to mention Chy.Srikanth, Swathi, Praneeth and Kartheek for their lovable memory which used to refresh my mind, during my tedious work.

  
-Idanalanati Pridhar.  
24/07/93

## ABSTRACT

The role of non-destructive testing (NDT) in high technology industry is crucial and inescapable. The quality consciousness of the structural products in both the manufacturing stage and during the operating lifetime are the main reasons for the industry to be aware of this(NDT) tool. Two of the key areas where NDT is pivotal are aeronautics and nuclear research. Ultrasonic means have found to be very effective in the inspection of composite materials and austenitic steels, both are highly anisotropic in nature. Scattering knowledge of ultrasonic waves by various flaws provides all the information regarding the inverse characterization of the defects which has not been thoroughly solved yet.

Computer simulation is a powerful aid to the understanding of physical processes. In the present work it is shown how Finite Element Analysis can be used in the study of ultrasonic wave propagation and scattering in general anisotropic media. Pulsed compression and Rayleigh wave interactions with surface cracks and body defects in isotropic media has been modelled. Also studied is the scattering by a delamination and a hole in a orthotropic composite laminate. These simulations are based on the numerical approximation of the hyperbolic equations of infinitesimal elasticity with simplest boundary conditions. The two-dimensional FEM model takes account of short duration pulses, finite-width beams and of different polarisations.

The physics of scattering is clear from the results, which are shown in the form of snapshots to visualise the mode-conversion, reflection and diffraction of scattered ultrasonic waves. The qualitative results are in agreement with the photo elastic fringe patterns and experimental observations. A marked difference in the lobe structure of scattering cross sections of composite laminates explains the beam skewing effect in anisotropic media.

# CONTENTS

	Page No.
List of Symbols	i
List of Tables	ii
List of Figures	iii
 Chapter 1	
Introduction	1
1.1 General Introduction	2
1.2 Ultrasonic Inspection	3
1.3 Literature Survey	8
1.3.1 Separation of Variables	8
1.3.2 Volume Integrals	9
1.3.3 Surface Integrals	9
1.3.4 Diffraction Methods	9
1.3.5 Numerical Methods	10
1.4 Present Work and Thesis Layout	13
 Chapter II	
Basics of Ultrasonic Wave Propagation and Scattering	15
2.1 Field equations of Linear Elastodynamics	15
2.2 Formulation of Boundary Value Problem	18
2.2.1 Two dimensional problems	19
2.3 Plane Waves	21
2.3.1 Isotropic solids	22
2.3.2 Transversely isotropic solids	23
2.4 Propagation in a Half-Space	28
2.5 Waves in Layered Media	29
2.6 Scattering of Ultrasonic Waves	29

Chapter III	Formulation and Computer Implementation	34
3.1	Finite Element Formulation	34
3.1.1	Formulation	34
3.1.2	Spatial discretization	37
3.1.3	Temporal discretization	38
3.1.4	Accuracy and Stability	39
3.2	Boundaries of the Domain	40
3.3	Modelling of Input Pulse	40
3.4	Determination of Scattering Parameters	42
3.5	Computer Implementation	43
Chapter IV	Results and Discussion	45
4.1	Results for Isotropic Solids	45
4.1.1	Propagation in defect-free isotropic solid	48
4.1.2	Rayleigh wave interaction with surface crack	48
4.1.3	Compression wave interaction with a surface crack	49
4.1.4	Compression wave interaction with a hole	50
4.1.5	Scattering of SV wave with a hole	52
4.1.6	Compression wave interaction with wedge crack	53
4.1.7	Scattering of shear waves by wedge crack	54
4.2	Results for composite materials	54
4.2.1	Scattering by a hole in a layered composite material	57
4.2.2	Scattering of SV pulse by a hole in L-T and T-T lamianate	58
4.2.3	Scattering by a delamination in a layered composite material	59
4.2.4	Scattering of SV wave from an interlaminar crack in T-L and T-T laminate	60
Chapter V	Conclusions and Scope for Future Work	123
5.1	Conclusions	123
5.2	Scope for future work	124
	References	126

# LIST OF SYMBOLS

$\overline{\sigma}_{ij}$	Stress tensor
$\epsilon_{ij}$	Strain tensor
$\omega$	Rotation tensor
$\Delta$	Dilation tensor
$t$	Time
$\rho$	Density
$u$	Displacement vector
$x$	Position vector
$b$	body force vector
$n$	unit normal vector
$t_i$	Traction vector
$\lambda, \mu$	Lames constants
$C_{ijkl}$	Elastic constants
$V$	Volume
$S$	Surface
$c$	Wave velocity
$c_1$	Dilation wave velocity
$c_2$	Rotation wave velocity
$c_r$	Rayleigh wave velocity
$\Gamma_{ij}$	Green-Christoffel's stiffnesses
$N_i$	Element shape functions
$\eta, \xi$	Natural coordinates
$\Delta t$	Time step
$h$	Spatial resolution

## LIST OF TABLES

	Name of Table	Page No.
Table 1	Range of wavelengths and order of magnitude for feature size in studies of wave propagation and scattering in solids	7
Table 4.1	Finite Element simulation details for various defects in isotropic solids	47
Table 4.2	Analyticaly calculated values of phase velocities in Graphite/Epoxy laminate in different directions	56
Table 4.3	Finite Element simulation details for various defects in composite materials	56

# LIST OF FIGURES

Fig. No.	Figure Name	Page No.
Fig. 1.1	Schematic Representation of Ultrasonic Pulse - echo System	5
Fig. 1.2	Model of General Ultrasonic NDT.	6
Fig. 1.3	Fields of Study which Include the Investigation of elastic Elastic Wave Propagation Phenomenon.	7
Fig. 2.1	Coordinate Systems for Wave Propagation.	20
Fig. 2.2	Wave Speeds as Functions of Angle of Propagation in Graphite - Epoxy Composite.	
Fig. 2.3	Basic Scattering Situation.	27
Fig. 3.1	Four-noded Isoparametric Element.	37
Fig. 3.2	Specification of Force Vector on Boundary to simulate Transducer Pulse.	43
Fig. 4.1	Geometry of Defect-free Isotropic Solid.	61
Fig. 4.2	X - Displacement Field for Defect-free Isotropic Solid.	62
Fig. 4.3	Y - Displacement Field for Defect-free Isotropic Solid.	63
Fig. 4.4	Geometry of Isotropic Solid with A Surface Crack.	64
Fig. 4.5	X-Displacement: Rayleigh Wave Interaction with A Surface Crack.	65
Fig. 4.6	Y-Displacement: Rayleigh Wave Interaction with A Surface Crack.	66
Fig. 4.7	Scattered X-Displacement Field: Rayleigh Wave Interaction with A Surface Crack.	67
Fig. 4.8	Scattered Y-Displacement Field: Rayleigh Wave Interaction with A Surface Crack.	68
Fig. 4.9	Wave Field Components which result from the interaction of pulsed Rayleigh Waves with A Surface Crack.	69
Fig. 4.10	Polar Plot of the Scattered Amplitudes by A Rayliegh Wave Interaction with A Surface Crack.	70
Fig. 4.11	X-Displacement Field: Compression Wave Interaction with A Surface Crack.	71
Fig. 4.12	Y-Displacement Field: Compression Wave Interaction with A Surface Crack.	72



Fig. 4.13 Scattered X-Displacement Field: Compression Wave Interaction with A Surface Crack.	73
Fig. 4.14 Scattered Y-Displacement Field: Compression Wave Interaction with A Surface Crack.	74
Fig. 4.15 (a) Interpretation of Photoelastic Visualisation of the Field After A Plane Compression Wave has Scattered from a Slit. (b) Contours of Compression Wave to correspond with (a).(c) Contours of Shear Wave to correspond with (a).	75
Fig. 4.16 Basic compression to Rayleigh wave mode conversion configuration.	75
Fig. 4.17 Polar plot of Scattered Amplitudes by a Compression wave interaction with a surface crack.	76
Fig. 4.18 Finite Element Discretization of a plate with hole.	77
Fig. 4.19 X-Displacement Field: Compression Wave Interaction with Hole in Isotropic solid.	78
Fig. 4.20 Y-Displacement Field: Compression Wave Interaction with Hole in Isotropic solid.	79
Fig. 4.21 Snapshots of the Scattered X- Disp. Field : Compression Wave Interaction with Hole in Isotropic Solid.	80
Fig. 4.22 Snapshots of the Scattered Y- Disp. Field : Compression Wave Interaction with Hole in Isotropic Solid.	81
Fig. 4.23 Polar Plot of Scattered Amplitudes by A Compression wave Interaction with A Hole.	82
Fig. 4.24 A-SCAN plot at a point before the hole surface (Compression wave interaction)	83
Fig. 4.25 X-Displacement Field: Compression Wave Interaction with Hole in Isotropic solid. (Resonance Condition)	84
Fig. 4.26 Y-Displacement Field: Compression Wave Interaction with Hole in Isotropic solid.(Resonance Condition)	85
Fig. 4.27 Snapshots of the Scattered X- Disp. Field : Compression Wave Interaction with Hole in Isotropic Solid. (Resonance Condition)	86
Fig. 4.28 Snapshots of the Scattered Y- Disp. Field : Compression Wave Interaction with Hole in Isotropic Solid. (Resonance Condition)	87

Fig. 4.29 Polar Plot of Scattered Amplitudes by A Compression wave Interaction with A Hole. (Resonance Condition)	88
Fig. 4.30 Snapshots of the Scattered X- Disp. Field : Plane Shear Wave Interaction with Hole in Isotropic Solid.	89
Fig. 4.31 Snapshots of the Scattered Y- Disp. Field : Plane Shear Wave Interaction with Hole in Isotropic Solid.	90
Fig. 4.32 Polar Plot of Scattered Amplitudes by A Shear wave Interaction with A Hole.	91
Fig. 4.33 Finite Element Descretization of A Wedge Crack (Body Defect).	92
Fig. 4.34 X-Displacement Field: Compression Wave Interaction with Wedge Crack.	93
Fig. 4.35 Y-Displacement Field: Compression Wave Interaction with Wedge Crack.	94
Fig. 4.36 Snapshots of the Scattered X-Displacement Field After a Plane Compression Wave has Interacted with Wedge Crack.	95
Fig. 4.37 Snapshots of the Scattered Y-Displacement Field After a Plane Compression Wave has Interacted with Wedge Crack.	96
Fig. 4.38 Angular Distribution of Scattered Amplitudes after a Plane Compression Wave interaction with Wedge Crack.	97
Fig. 4.39 (a)A-Scan plot at a point before the Wedg crack. (b)A-Scan plot at a point after the Wedg crack.	98
Fig. 4.40 Snapshots of the Scattered X-Displacement Field After a Plane Shear Wave has Interacted with Wedge Crack.	99
Fig. 4.41 Snapshots of the Scattered Y-Displacement Field After a Plane Shear Wave has Interacted with Wedge Crack.	100
Fig. 4.42 Angular Distribution of Scattered Amplitudes after a Plane Shear Wave interaction with Wedge Crack.	101
Fig. 4.43 X-displacement field : Plane Compression wave interaction with a hole in Layered Structure.	102
Fig. 4.44 Y-displacement field : Plane Compression wave interaction with a hole in Layered Structure.	103
Fig. 4.45 Scattered X- disp. field : plane Compression wave interaction with a hole in Layered Structure.	104
Fig. 4.46 Scattered Y- disp. field : plane Compression wave interaction with a hole in Layered Structure.	105

Fig. 4.47	Polar plot of Scattered amplitudes after a Compression wave interacts with a hole in Layered Structure.	106
Fig. 4.48	X-displacement field : Plane Shear wave interaction with a hole in Layered Structure.	107
Fig. 4.49	Y-displacement field : Plane Shear wave interaction with a hole in Layered Structure.	108
Fig. 4.50	Scattered X- disp. field : plane Shear wave interaction with a hole in Layered Structure.	109
Fig. 4.51	Scattered Y- disp. field : plane Shear wave interaction with a hole in Layered Structure.	110
Fig. 4.52	Polar plot of Scattered amplitudes after a Shear wave interacts with a hole in Layered Structure.	111
Fig. 4.53	A- Scan plot at a point before the hole in a composite laminate. ( Shear wave interaction)	112
Fig. 4.54	Finite Element Discretization of Layered Composite Structure with an Interface Crack.	113
Fig. 4.55	X-displacement field : Plane Compression wave interaction with an Interface Crack in Layered Structure.	114
Fig. 4.56	Y-displacement field : Plane Compression wave interaction with an Interface Crack in Layered Structure.	115
Fig. 4.57	Scattered X- disp. field : plane Compression wave interaction with an Interface Crack in Layered Structure.	116
Fig. 4.58	Scattered Y- disp. field : plane Compression wave interaction with an Interface Crack in Layered Structure.	117
Fig. 4.59	Polar plot of Scattered amplitudes after a Compression wave interacts with an Interface Crack in Layered Structure.	118
Fig. 4.60	A- Scan plots comparision in a T-L & L-T composite laminate with and without interface crack.	119
Fig. 4.61	Scattered X- disp. field : plane Shear wave interaction with an Interface Crack in Layered Structure.	120
Fig. 4.62	Scattered Y- disp. field : plane Shear wave interaction with an Interface Crack in Layered Structure.	121
Fig. 4.63	Polar plot of Scattered amplitudes after a Shear wave interacts with an Interface Crack in Layered Structur	122

# CHAPTER I

## INTRODUCTION

### 1.1 GENERAL INTRODUCTION

The elastic wave propagation and scattering have been under investigation for several years, because of the technological needs associated with the seismology, nuclear test monitoring, structural response to high rates of loading, and non destructive evaluation. The effects of very short term impact loads on structures can be understood fully if analyzed in terms of propagation of stress waves. Crack propagation or the interaction of dynamic stress fields with existing cracks, voids or inclusions in a material can be predicted if the dynamic effects are taken into account. Further the knowledge of elastic wave propagation is essential in a host of other fields such as ultrasonics, geophysics, electronics etc.

The reliability and suitability/integrity of a structural component for its further service depends upon the current material state, failure modes and service conditions. Cracks are one feature which limit the strength of structures under stress and often causes its catastrophic failure. But voids, inclusions, interfaces, distribution of cracks and in general damaged regions of material will have dangerous effects on the performance of the components. Critical crack sizes vary from several tens of millimeters in thick steel structures down to fractions of a millimeter in turbine blades and other aero components, while in the case of ceramic materials these are of the order of few micrometers. Thus it is highly desirable to assess the material state. The role of quantitative non destructive measurements lies in identifying and sizing microscopic flaws that would ultimately lead to failure.

Because of their ability to penetrate into the interior of the metal, composite material or ceramic parts the elastic waves are one of the most important forms of probing energy. Ultrasonic waves are such

types of waves which exhibit rich propagation phenomena and can be utilized in extracting a wide range of information about the structural integrity of a component. The scattering, reflection and mode conversion of are the different phenomenon of pulsed elastic waves that provide the basis for ultrasonic NDT.

In general, ultrasonic flaw detection and characterization techniques can be carried in two approaches. The imaging approach seeks to process the scattered field in such a manner that a visual outline of the object is produced on a display. The inverse-scattering approach attempts to infer geometrical characteristics of a flaw from either the angular dependence of its far-field scattering amplitude at a fixed frequency, or from the frequency dependence of its far-field scattering amplitude at fixed angles. The solution to the direct scattering problem, that is, the computation of the field generated when an ultrasound wave is scattered by a known flaw, is a necessary step to understand the solution of an inverse problem.

In most of the ultrasonic non-destructive applications the material is taken to be homogeneous except for any defect. The wave propagation is then rectilinear with simple laws of reflection at plane boundaries except for the complex scattering phenomenon at the inhomogeneity. If the grains are larger than an ultrasonic wave length and there is a preferred texture then the material becomes anisotropic. Examples of materials where anisotropy is apparent are composite materials such as fiber-reinforced plastics, austenitic steels, crystalline semiconductor materials and rocks.

Composite materials are widely used in structural applications where high strength-to-weight and stiffness-to-weight ratios are required. Air crafts are typical weight sensitive structures in which composite materials are cost effective. Composite materials can be tailored to efficiently meet the design requirements of stiffness, strength and many other parameters in various directions. Unfortunately, the manufacturing process of composites may result in the presence of unwanted artifacts defects such as voids, resin rich areas, distorted fibers and inclusions. Damage and general material degradation

can also occur during the in-service operation of composite components. Typical causes of such damage are continuous cyclic/fatigue loading, rapid changes in local temperature and moisture, and impact loading [1]. So, tests are needed in both the manufacturing phase of composite structures in order to assure quality as well as during the operating lifetime of the components in order to predict and hence prevent failure.

Propagation of waves through homogeneous anisotropic media is more complicated than propagation in homogeneous isotropic media. The direction of energy flow is not necessarily at right angles to the wave front. This effect, known as *beam skewing*, has been interpreted as causing much of the difficulty in the inspection of composite structures. A large number of wave propagation studies in a laminated and fibrous composite medium are limited by the assumption that the structure is periodic or the distribution is deterministic [2].

The motivation of the present work is to study the wave propagation and scattering of ultrasonic waves in materials which are both anisotropic and inhomogeneous but with a scale of inhomogeneity varying from a fraction to a few times a ultrasonic wavelength. The defects in composite materials are just of this nature.

## 1.2 ULTRASONIC INSPECTION

In ultrasonic inspection short bursts of a few cycles of elastic wave energy, typically in the frequency range of 1-10 MHz, are injected into the part being inspected. The variation in the speed of wave propagation and energy loss by interaction with material microstructure are the wave parameters obtained for the characterization of material properties. A typical Ultrasonic NDT system is illustrated in Fig 1.1. Flaws are indicated by the reflection of the energy (echoes) back to the same transducer (pulse-echo) as shown or to a second transducer (pitch-catch/through-transmission). In state-of-the-art systems, the signal processing takes the form of amplification followed by rectification [3]. Flaws are detected when an echo appears that exceeds a preselected threshold. The size is then estimated based on either the

peak value of this echo or the variation of echo height as the probe is moved.

Unfortunately, quantitative characterization of a flaw i.e., the measurement of size, location, orientation and roughness, based on amplitude measurements may be very inaccurate unless the measurement is carefully calibrated. The reason is that part of the incident energy that insonifies the flaw is scattered rather than specularly reflected. Hence, the calculation of the total field which includes scattering effects is rather complicated. It was also an established fact that the attenuation coefficient of an ultrasonic wave highly depends upon scattering rather than absorption (due to internal friction and dislocation movement) at frequencies higher than 1 M Hz.

Three elements play a major role in the physical solutions of detecting and sizing flaws : transducer improvements, high-speed digital processing and elastic wave scattering theories. In practice, transducers do not follow theoretical expectations [4]. Hence, their individual properties (radiation pattern, impulse response etc.,) must be measured and taken into account when interpreting experimental data.

The essential feature of improved interpretation of ultrasonic signals is a fundamental understanding of elastic wave - flaw interaction. The limitations imposed by the analytical methods in these studies have been overcome in the recent years by numerical methods, which require high speed digital computing facilities. The whole range of modelling techniques are becoming increasingly attractive and practical with the developments in and the availability of super computers. Modelling studies can play an important role in Ultrasonic NDT by providing :

- (a) Physical insight into the nature of ultrasound/defect interaction by observing complete wave field visualisation.
- (b) Simulation results for ultrasonic testing situations too difficult or expensive to replicate in the laboratory.
- (c) Reflection coefficients.
- (d) Design data for planned ultrasonic tests.
- (e) The reliability of flaw detection.

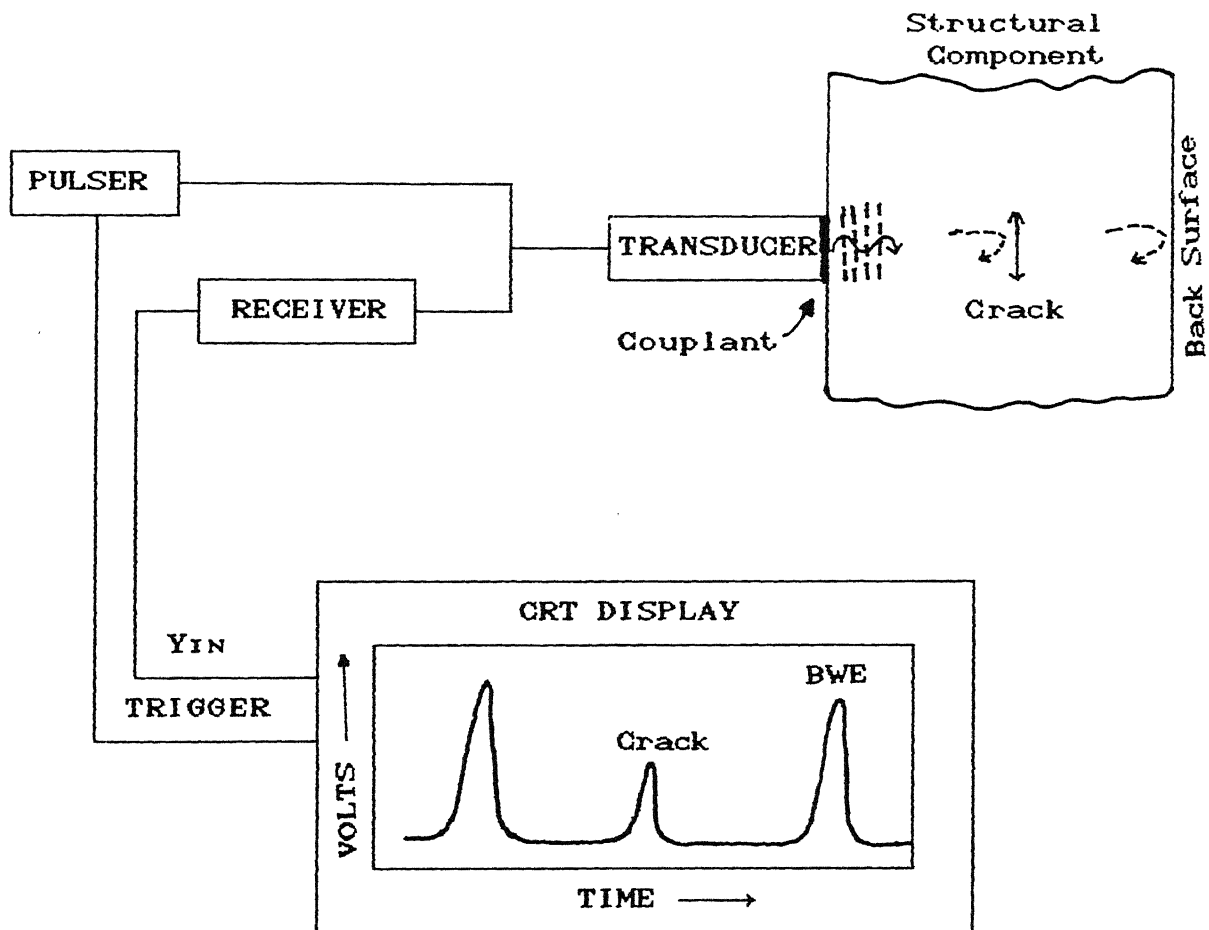


**Fig.4.1. Schematic Representation of Ultrasonic Pulse-echo System**



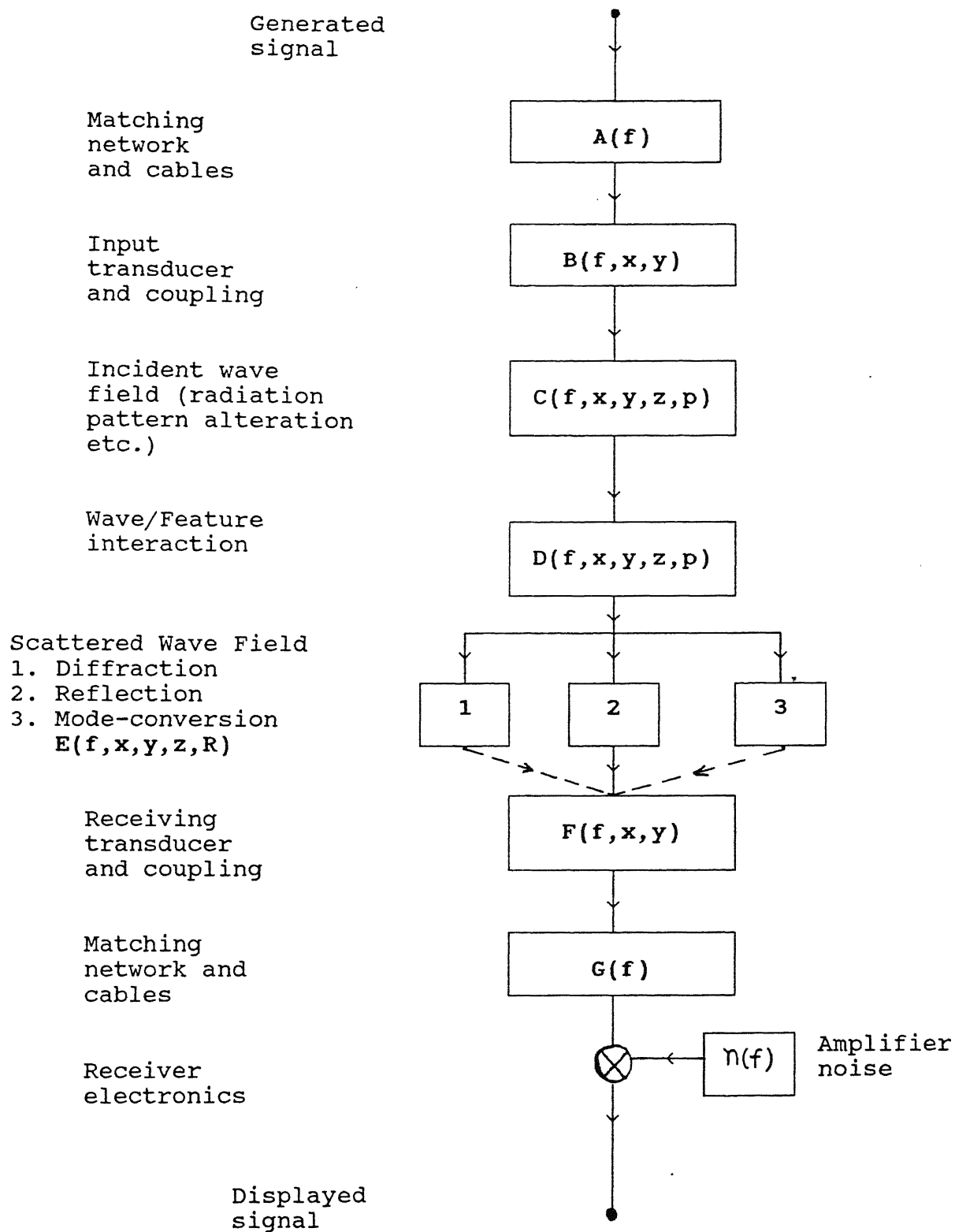


Fig 1.2 Model of general NDT

TABLE 1

Range of wavelengths and order of magnitude for feature size in studies of wave propagation and scattering in solids

Subject	Wave Length ( $\lambda$ )	Frequency ( $f$ )	Feature Size ( $d$ )	Order of Magnitude ( $M$ )
Geophysics	$\sim 40$ km	$\sim 0.05$ Hz	1000 km	$10^6$ m
Seismology	- -	- -	10-100 m	$10^2$ m
Civil Eng. Mech. Eng.	$\sim 10$ m	100s Hz	1-10 m	10 m
NDT	0.1-100 mm	0.025-15 MHz	1-10 mm	$10^{-3}$ m
Electronics (SAW)	$\sim 0.05$ mm	$> 40$ MHz	0.01 mm	$10^{-5}$ m

### ULTRASONIC NDT/NDE

Defect characterization  
Material property studies  
Acoustic emission  
Acoustic microscopy

### GEOPHYSICS AND SEISMOLOGY

Time series analysis  
Forward and inverse problems  
Earthquake studies  
Exploration seismology

### ELECTRONICS

Bulk and surface  
acoustic wave  
devices

ELASTIC  
WAVE  
PROPAGATION  
PHENOMENA

### CIVIL AND MECH. ENGINEERING

Site investigation  
Vibration studies  
Earth quake damage prediction

### MATHEMATICS/APPLIED MECH.

Fundamental elastic wave  
propagation and scattering  
Fracture mechanics &  
Dynamic crack propagation

Fig. 1.3 Fields of study which include the investigation of elastic wave propagation phenomena.

### 1.3 LITERATURE REVIEW

Understanding the propagation and scattering of waves through an elastic medium is of potential benefit in several fields. Fig 1.2 shows the fields of study which includes the investigation of elastic wave propagation phenomenon. An excellent research literature on the state of the art of stress wave propagation and scattering was reviewed by Pao [5]. The role of elastodynamic scattering problems in quantitative non-destructive evaluation has been reviewed by Gubernatis [6] and Bond et al [7]. Some practical applications have been discussed by Coffey and Chappman [8 ].

Most of the classical solutions of scattering by a flaw are applicable either at very high frequency range,  $ka \gg 10$ , or at very low frequency,  $ka \ll 1$ , where ' $k$ ' is the wave number and ' $a$ ' is the flaw major dimension. In the mid-frequency range, where the wave length of the elastic wave is approximately equal to the flaw dimension, the solution of elastic scattering problem become very complex because of mode-conversion phenomenon involved. In addition, the analytical solutions are restricted to infinite or semi-infinite medium, homogeneous and isotropic solids and idealized defect shapes. Results have been obtained for wave interactions with a penny-shaped crack, infinite strip, cylinder, sphere and wedge [43,44].

The following are the commonly used techniques to solve various elastodynamic scattering problems.

#### 1.3.1 Separation of Variables

The scattering of elastic waves by a circular cylinder or a sphere can be analyzed by expanding the scattered field in a series of wave functions [9]. For these shapes of flaws the wave equations are easily separable in an orthogonal curvilinear co-ordinate system to allow for the matching of boundary conditions. The solutions thus obtained have wide applications in analyzing dynamic stress concentration and interaction of structures with ground waves.

### 1.3.2 Volume Integrals

The waves scattered by an inhomogeneity are expressed by a volume integral of equivalent body force multiplied by the Green's function for the surrounding medium. The volume integral which contains the unknown total wave field can be solved by iteration, and the solution is called Born approximation, if the incident wave field is substituted for the unknown total wave as the first trial [10].

### 1.3.3 Surface Integrals

The surface integral formulation is useful for treating crack-like geometries. The governing differential equation for elastic waves is converted to an integral over the surface of the scatterer. The surface integral equation is solved numerically by using Hilbert-Schmidt method [11]. It can also be reduced to a system of linear algebraic equations for the scattered amplitude which are then solved numerically by matrix methods. Two such methods are transition matrix (T-matrix) theory [12] and the method of optimal truncation (Moot) [13].

### 1.3.4 Diffraction Methods

At high frequencies, the scattering of elastic waves are analyzed on the basis of elastodynamic ray theory [14]. In Keller's [15] Geometric Theory of Diffraction (GTD), the diffracted field is related to the incident field through diffraction coefficients. These are determined through the solution of an appropriate canonical problem. However, the lack of canonical solutions for elastic waves imposes a serious limitation of GTD method. A fully three-dimensional ray tracing computer code for anisotropic and inhomogeneous media was developed by Ogilvy [16]. The model takes into account correctly the amplitude and phase changes at boundaries between media and can therefore, be used to make quantitative as well as qualitative predictions. Ray tracing work has shown that angled compression and shear horizontal waves maintain their focus well, whereas shear vertical polarized waves are always greatly defocussed.

### 1.3.5 Numerical Methods

These are the computer-modelling techniques which are based on the numerical solution of the partial differential equations describing the scattering system. In fact, these are the only methods available in the complex mid frequency region, where the scatterer dimensions are of the same order as the ultrasonic wavelength. A survey of numerical methods used for solving the elastodynamics was discussed by Bond [17]; in particular to seismology was given by Chin et al; [18]. The following three families of techniques are commonly employed:

#### *1. Boundary Element Methods*

The Boundary Element Method involves the solution of an integral equation, which is obtained by dividing the surface of scatterer into small elements each of which then has an unknown displacement [19]. Schafbush et al [20] have applied three dimensional boundary element method to elastodynamic problems related to ultrasonic numerical differential equations. Hall and Robertson [21] have studied the scattering of a plane wave by a circular cylinder using 2D boundary element method and compared the results obtained for various elements with the analytical solution.

#### *2. Finite Difference Methods*

In numerical modelling applied to elastic waves much effort has been concentrated on the finite difference method. Finite difference models give a complete description of the time development of the wave-field of interest. The methodology involves the replacement of the governing partial differential equations by difference equations, and then solving them numerically. Alterman and Karal [22]; and Bore [23] have employed this method for seismology applications.

Developments in the finite difference modelling of ultrasonic wave propagation have been reported by C.J. Bond and his co-workers [17]. They have modelled a range of compressional, shear and Rayleigh wave systems on isotropic, homogeneous media, involving surface slots and

cracks. The results are shown in the form of a display in which vector displacements are scaled to appear as lines in the direction of displacement, and follow the progress of an elastic wave through the medium. These results have been found to agree with the photo-elastic visualisations. In addition, immersion inspection systems have been modelled where there is propagation in both an elastic solid and a viscous fluid [24].

To reduce the problems associated with the use of limited extent spatial grids absorbing boundaries have been investigated and incorporated into the models [25].

Bond [26] has emphasized on the "mode conversion" and "total-wave" concepts in particular to ultrasonic NDT and has given details of experimental results of crack characterisation by making use of the mode-conversion phenomenon.

Temple [27] has used a three dimensional finite difference model to study the propagation and scattering of elastic waves of different polarizations from a cylindrical hole in a transversely austenitic steel welds. Results in the form of A-scan display and scattering cross-section are given and compared with the experimental results of White [28].

Harumi and his co-workers [29] have produced various 'lumped mass' schemes which appear to overcome many of the limitations on the scatterer shape imposed by the conventional cartesian co-ordinates. Oglivvy and Temple [30] have applied both ray-tracing and finite difference methods for predicting the behaviour of ultrasound in typical manual-metal-arc-weldments. They have demonstrated that the two approaches are consistent and complementary.

### *3. Finite Element Methods*

The superiority of finite element method lies in its ability to handle complex domains, defect shapes, inhomogeneities, material non-linearities, applying the boundary conditions etc.

Smith [31] has developed a finite element code to study the body wave propagation problems in seismology. He modelled a deep earthquake zone realistically in two dimensions and earthquakes simulated at depth.

Lord and his co-workers have produced a scheme to solve the elastodynamic problem using a finite element formulation for spatial discretization and finite difference formulation for time marching. Ludwig and Lord [32] has reported the details of 2-D finite element code employing Newmark's algorithm to evaluate time integration. Results were given in the form of simulated A-scan and visualisation of wave-fields for a longitudinal pulse at different instants. Transmitter and receiver models have also been incorporated to take care of transducer effects [33]. The results were comparable with the practical ultrasonic NDT measurements. You and Lord [34] have reported improvements in the scheme from computational point of view, by employing a central-difference algorithm for time integration and a "lumped mass matrix" to avoid matrix inversion. They have also studied wave interactions with a rectangular slot and surface breaking cracks in an isotropic medium.

A detailed analysis of various computational aspects of different algorithms used in the finite element method for the wave equation, from the accuracy, speed and storage points of view, has been reported by Seron et al [35]. It is concluded that, although central-difference scheme is the best in terms of computational speed and cost, Newmark's constant average acceleration (CAA) scheme along with quadrilateral mesh gives the best accuracy.

Ludwig et al [36] have reported a 2-D finite element modelling of wave propagation in an orthotropic material. Results were discussed with respect to the focussing, defocussing and skewing of ultrasonic beam.

You and Lord [37] have demonstrated a finite element test bed for diffraction Tomography as an inverse-algorithm and used the normal component of the displacement data on the measure line to reconstruct an object function.

Recently Jaleel et al [38] have developed a Finite Element code to study the pulsed compression wave and Rayleigh wave interaction with cracks in isotropic and Graphite/epoxy composite laminate . It was found that for quasi-longitudinal wave the displacement along the fiber is prominent, whereas for quasi-transverse wave the displacement perpendicular to the fiber is prominent.

An important parameter in elastic wave scattering is the total power scattered by the flaw. It is customary to relate the scattered power to the power per unit area normal to the incoming wave. This ratio has the dimension of area and is known as *scattering cross-section*. Barrat and Collins [39] have considered the total field as a superposition of a plane wave field and scattered field. They have shown that cross section can be calculated from the far field amplitude of the scattered wave in the direction of propagation of the incident wave. Krenk and Schmidt [40] have reported an extensive results of elastic wave scattered by a circular crack in the form of maps of the scattered far field as scattering cross sections. White[29] has calculated the cross sections for the case of scattering by a hollow circular cylinder, fluid filled cylinder and the results are compared with his experiments.

Su et al. [41] have extended the unimoment method to elastic wave scattering problems. This method uses the finite element approximations for the field in the vicinity of the scatterer and the scattered field outside this region by wave function expansions that satisfy appropriate radiation conditions at infinity. Goetschel et al [42] have employed exterior wave functions to the wave field with finite element to the near field to study the cross sections for a variety of axisymmetric inclusions.

#### 1.4 PRESENT WORK AND THESIS LAYOUT

In the present work a two dimensional plane strain finite element model is developed to study the ultrasonic wave propagation and scattering in linear, elastic medium.



The model is capable of predicting the propagation of short pulses of ultrasonic waves in a finite width beam through a anisotropic medium and of predicting the amplitudes of waves scattered from wedge crack, side drilled holes type defects.

Pulsed compression and shear wave interaction with a wedge crack and cylindrical hole in an isotropic medium were studied. The scattered waves are clearly showing the mode conversion phenomenon. Elastic wave propagation and scattering in Graphite/Epoxy composite has been investigated. The material is modelled as homogeneous and orthotropic. Differential scattering cross section were drawn for all the above mentioned cases.

Chapter II of the thesis gives the basics of ultrasonic wave propagation and scattering. Wave propagation in elastic medium, plane waves in isotropic and transversely isotropic medium were discussed. Formulation of boundary value problem is given. Ultrasonic wave scattering by a single flaw is discussed and scattering cross section details were also described.

In Chapter III the finite element formulation of the hyperbolic wave equation is presented. Transducer considerations and artificial boundary problem are mentioned. Methodology employed to calculate the scattering cross section and computer implementation are also discussed.

Chapter IV gives the results and discussions of the simulations performed using the FEM code. Conclusions and scope for future work are given in the last chapter V.

## CHAPTER II

### BASICS OF PROPAGATION AND SCATTERING OF ULTRASONIC WAVES

When a solid is subjected to dynamic loads, the stresses become functions of both space and time, and the elastodynamics is that branch of solid mechanics, which determine these stresses. The mathematical treatment of elastodynamic problems is distinguished from that of the elastostatic case by the presence of the the acceleration term in Cauchy's equation of motion [43].

#### 2.1 FIELD EQUATIONS OF LINEAR ELASTODYNAMICS

Under the assumption of linearity, for a body of volume  $V$  enclosed by surface  $S = S_\sigma + S_u$ , where on  $S_\sigma$  tractions are prescribed and on  $S_u$  displacements are prescribed, the equation of motion [44] may be written as

$$\sigma_{ij,j} + \rho b_i = \rho u_{i,tt} \quad (2.1)$$

Where  $\sigma_{ij}$  is the stress tensor,  $u_i$  is the displacement vector,  $b_i$  is the body force per unit volume and  $\rho$  is the mass density of the material.

The linear constitute equations for a hyperelastic solid in the absence of thermal and other non-mechanical effects is of the form

$$\sigma_{ij} = C_{ijkl} \epsilon_{kl} = C_{ijkl} (u_{k,l}) \quad (2.2)$$

Where  $C_{ijkl}$  is the elastic stiffness tensor with the symmetry properties

$$C_{ijkl} = C_{jikl} = C_{ijlk} = C_{klij} \quad (2.3)$$

Upon substituting (2) in (1)

$$\frac{\partial}{\partial x_j} \left[ C_{ijkl} \frac{\partial u_k}{\partial x_l} \right] + \rho b_i = \rho \frac{\partial^2 u_i}{\partial t^2} \quad (2.4)$$

This is the Navier-Cauchy equation of motion for an anisotropic and inhomogeneous elastic solid. It will not be possible to seek an analytical solution to these three coupled equations. Solutions in directions of high symmetry can be found for homogeneous media such as single crystals [45], but even for arbitrary directions in homogeneous anisotropic media the solutions are best found numerically.

For an isotropic solid, the elastic stiffness tensor has the special form

$$C_{ijkl} = \lambda \delta_{ij} \delta_{kl} + \mu \left( \delta_{ik} \delta_{jl} + \delta_{il} \delta_{jk} \right) \quad (2.5)$$

Where  $\lambda$ ,  $\mu$  are the Lamé's constants and the stress strain relation becomes

$$\sigma_{ij} = \lambda \epsilon_{kk} \delta_{ij} + 2 \mu \epsilon_{ij} \quad (2.6)$$

The strain displacement relations are

$$\epsilon_{ij} = \frac{1}{2} \left( u_{i,j} + u_{j,i} \right) \quad (2.7)$$

Substitution from (2.2) and (2.7) into (2.1) leads to the governing equation of motion in terms of displacements as

$$\left( \lambda + \mu \right) u_{j,ji} + \mu u_{i,jj} + \rho b_i = \rho \frac{\partial^2 u_i}{\partial t^2} \quad (2.8)$$

The vector equivalent of this expression is

$$\left( \lambda + 2\mu \right) \nabla \nabla \cdot \vec{u} - \mu \nabla \times \nabla \times \vec{u} + \rho \vec{B} = \rho \frac{\partial^2 \vec{u}}{\partial t^2} \quad (2.9)$$

The equation of motion (2.9) represents a system of three coupled partial differential equations for the displacement components; they must be solved subjected to boundary conditions,

$$\begin{aligned} \sigma_{ij} n_j &= t_i & \text{on } S_\sigma & \quad (\text{Traction B.C.}) \\ u_i &= u'_i & \text{on } S_u & \quad (\text{Displacement B.C.}) \end{aligned} \quad (2.10)$$

and initial conditions,

$$\begin{aligned} u_i(x, 0) &= u_i^o(x, 0) \\ \dot{u}_i(x, 0) &= \dot{u}_i^o(x, 0) \end{aligned} \quad (2.11)$$

where  $t_i$ ,  $u'_i$ ,  $u_i^o$  and  $\dot{u}_i^o$  are prescribed quantities.

By defining the dilation and rotation vectors as

$$\Delta = \nabla \cdot \vec{u} = \epsilon_{ii} \quad (2.12)$$

$$\omega = \frac{1}{2} \nabla \times \vec{u} \quad (2.13)$$

The equation of motion (2.9) may be expressed as

$$\left( \lambda + 2\mu \right) \nabla \Delta - 2\mu \Delta \times \vec{\omega} + \rho \vec{B} = \rho \frac{\partial^2 \vec{u}}{\partial t^2} \quad (2.14)$$

The above form of representation explicitly displays the dilation and rotation. Another advantage is that the result is valid in any curvilinear coordinate system.

## 2.2 FORMULATION OF BOUNDARY-VALUE PROBLEM

The direct solution of the governing elastodynamic equations (2.9) is quite difficult due to the strong coupling between the three components of the displacement vector  $u$ . A convenient way for decoupling them is to introduce *scalar and vector potentials*, by using Helmholtz's theorem. The displacement and body force vector can be written as

$$u = \text{grad } \phi + \text{curl } \psi \quad (2.15)$$

where  $\nabla \cdot \psi = 0$ . In the above equation  $\phi$  and  $\psi$  are scalar and vector valued functions of position and time.

$$F = \text{grad } \Omega + \text{curl } \chi \quad (2.16)$$

The completeness of this representation has been discussed by Achenbach [44]. Substitution of  $u$  and  $F$  in (2.9) and after simplifying the terms leads to the following equation

$$\text{grad} \left( c_1^2 \nabla^2 \phi - \frac{\partial^2 \phi}{\partial t^2} + \Omega \right) + \text{curl} \left( c_2^2 \nabla^2 \psi - \frac{\partial^2 \psi}{\partial t^2} + \chi \right) = 0 \quad (2.17)$$

where  $c_1$  and  $c_2$  are longitudinal and shear wave velocities.

Clearly, if

$$\ddot{\phi} - c_1^2 \nabla^2 \phi = \Omega \quad (2.18)$$

and

$$\ddot{\psi} - c_2^2 \nabla^2 \psi = \chi \quad (2.19)$$

then  $u$  satisfies the equation of motion.

Hence  $\phi$  and  $\psi$  satisfy wave equations with two distinct wave speeds  $c_1$  and  $c_2$  respectively. Since  $c_1 > c_2$ , these are referred to as P-(primary) waves and S-(secondary) waves in geophysics literature. In

mechanics literature these are known as pressure or dilational or compressional waves and shear or equivoluminal waves, respectively. It is worth mentioning that the mechanical disturbances associated with these two fields  $\phi$  and  $\psi$  propagate unchanged only if there are no boundaries or scattering surfaces present i.e., anisotropic and homogeneous medium. Boundary conditions at such interfaces will, in general, couple the two fields, giving rise to the phenomenon of mode conversion. In other words, either P-waves or S-waves will generate both P-waves and S-waves on striking a boundary. This is a feature which does not have a counterpart in acoustics and electromagnetics.

### 2.2.1 Two-Dimensional Problems

If the field variables  $u, v, w$  are independent of one of the coordinates, then the equations of elastodynamics can be split into two independent systems of differential equations and boundary conditions; one system describes the in-plane deformation and the other, the antiplane deformation of the solid. Assuming that the displacement and stress components are independent of the coordinate  $z$ , then the components of the Navier's equation for an isotropic solid becomes,

$$\left( \lambda + \mu \right) \frac{\partial \Delta}{\partial x} + \mu \nabla^2 u = \rho \frac{\partial^2 u}{\partial t^2} \quad (2.20.a)$$

$$\left( \lambda + \mu \right) \frac{\partial \Delta}{\partial y} + \mu \nabla^2 v = \rho \frac{\partial^2 v}{\partial t^2} \quad (2.20.b)$$

$$\mu \nabla^2 w = \rho \frac{\partial^2 w}{\partial t^2} \quad (2.20.c)$$

where  $\Delta = u_{,x} + v_{,y}$

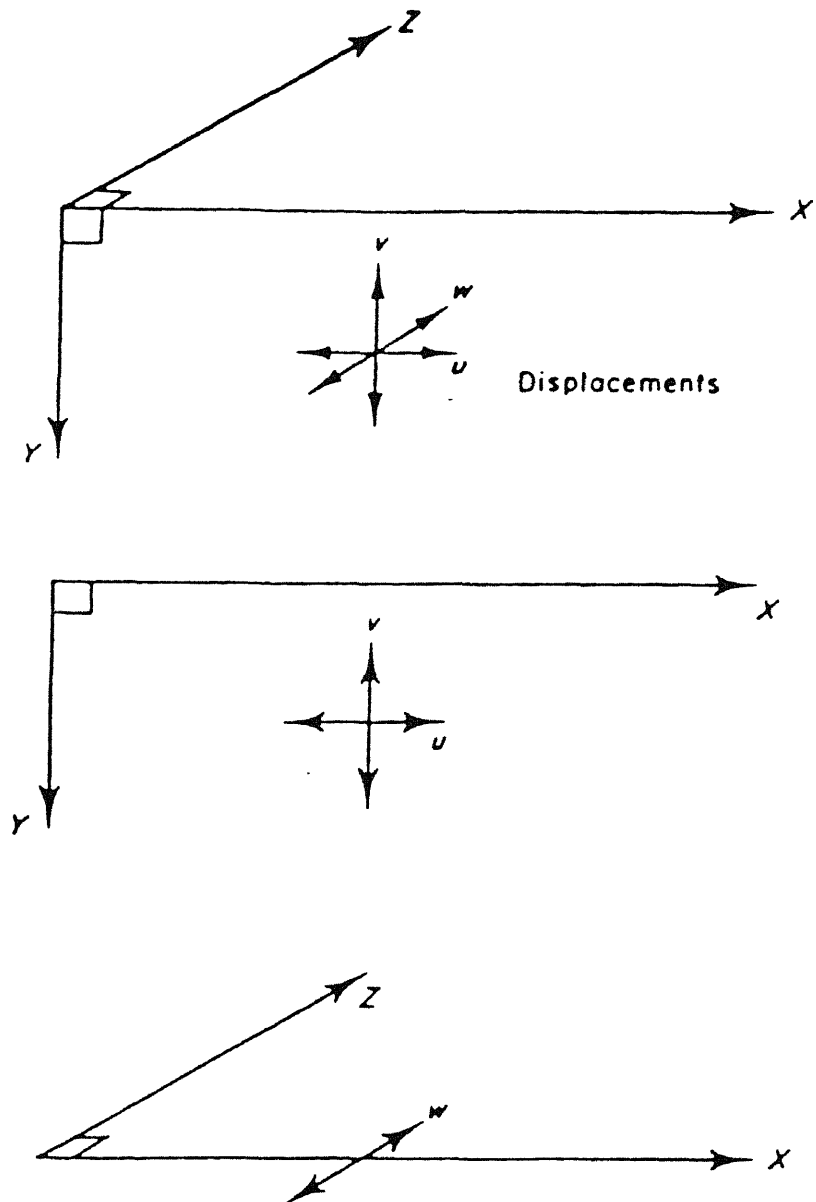


Fig.2.1 Coordinate systems: (a) Cartesian coordinates;  
 (b) two-dimensional XY (P-SV) coordinates;  
 (c) two-dimensional XZ (SH) coordinates.

The in-plane displacement components  $u$  and  $v$  satisfy the first two partial differential equations and the in-plane stress components. Thus, if the boundary conditions of the problem are given in terms of these variables, then the displacement component ' $w$ ' will play no role in the solution of the problem. In seismological problems, the  $xz$ -plane is often taken as the horizontal plane on the surface of the earth. Since the displacement vector  $(u,v,0)$  lies in the vertical plane through the direction of propagation, the  $S$  waves represented by the vector potential  $\psi$  are called vertically polarized shear waves, or, simply SV waves.

The antiplane displacement  $w$  satisfies the third partial differential equation (20.c) and the antiplane stress components  $\sigma_{xz}$  and  $\sigma_{yz}$ . Since the displacement component  $w$  is horizontal and is perpendicular to the direction of propagation, the waves represented by  $w$  are called horizontally polarized shear waves, or SH waves. Fig. 2.1 shows various combinations of displacements in a cartesian coordinate system, which are generally employed.

### 2.3 PLANE WAVES

The equation of motion for a linear anisotropic elastic solid in the absence of body forces is given by

$$C_{ijkl} u_{k,lj} - \rho u_{i,tt} = 0 \quad (2.21)$$

Consider a displacement vector in the following form

$$u(x,t) = a f \left( t - \frac{n \cdot x}{v} \right) \quad (2.22)$$

in index notation  $u_i(x,t) = a_i f \left( t - \frac{n \cdot x}{v} \right)$

where

$a$  = amplitude of displacement vector



$v$  = phase velocity

Substituting (22) into (22) yields,

$$\left[ \left( \frac{C_{ijkl} n_j n_l}{v^2} \right) a_k - \rho a_i \right] f''(\xi) = 0 \quad (2.23)$$

Since function  $f$  is arbitrary,  $f''(\xi) \neq 0$ , therefore,

$$\left( \rho v^2 \delta_{ik} - \Gamma_{ik} \right) a_k = 0 \quad (2.24)$$

where  $\Gamma_{ik} = C_{ijkl} n_j n_l$  known as Green-Christoffel Constants. Equation (2.24) gives a system of three homogeneous linear algebraic equations for the unknowns, the scalar  $v$  and the vector  $a$ . The matrix from (2.24) is

$$\left[ \rho v^2 \delta_{ij} - \Gamma_{ik} \right] \left\{ a_k \right\} = \left\{ 0 \right\} \quad (2.25)$$

i.e.. The three eigen values of the phase velocity  $v$  and three associated eigen vectors for the polarizations can be obtained from equation (2.25). Since  $[\Gamma_{ik}]$  is symmetric and real, equation (2.25) must have three real eigen values and three linearly independent eigen vectors. Hence  $\rho v^2$  satisfies the characteristic equation

$$\det \left[ \rho v^2 \delta_{ik} - \Gamma_{ik} \right] = 0 \quad (2.26)$$

The three eigen values of (2.26) gives the possible wave speeds in a given direction of propagation  $n$ , and the corresponding eigen vectors represent the direction of particle movement.

### 2.3.1 Isotropic Solids

For the case of isotropic solid, the elastic stiffness tensor is given by (2.5). So

$$\Gamma_{ik} = (\lambda + \mu) n_i n_k + \mu n_j n_j \delta_{ik} \quad (2.27)$$

Since  $n$  is a unit vector  $n_j n_j = 1$ , and so

$$\Gamma_{ik} = (\lambda + \mu) n_i n_k + \mu \delta_{ik} \quad (2.28)$$

Substituting the value of  $\Gamma_{ik}$  in (2.26) and simplifying the characteristic equation reduces to

$$\left[ \rho v^2 - (\lambda + 2\mu) \right] \left[ \rho v^2 - \mu \right] = 0 \quad (2.29)$$

Thus, the two possible wave speeds in an isotropic case are given by

$$v_1 = \left( \frac{\lambda + 2\mu}{\rho} \right)^{\frac{1}{2}} = c_l$$

and

$$v_2 = \left( \frac{\mu}{\rho} \right)^{\frac{1}{2}} = c_t \quad (2.30)$$

These wave speeds are independent of  $n$ , so the two waves propagate with the same speed in all directions. It can be easily shown that the particle motion associated with  $v_1$  and  $v_2$  are parallel and perpendicular to the direction of wave propagation.

### 2.3.2 Transversely Isotropic Solid

If an orthotropic solid exhibits symmetry with respect to arbitrary rotations about one of the axes, then it is called "transversely isotropic" solid. The linear stress-strain law for a transversely isotropic solid may be given in various forms. Without loss of generality, by assuming the symmetric axis of the material as coinciding with the  $x_1$  - axis, the elastic stiffness tensor may be represented as [46]

$$\begin{aligned}
C_{ijkl} = & \lambda \delta_{ij} \delta_{km} + \mu_t \left( \delta_{ik} \delta_{jm} + \delta_{jk} \delta_{im} \right) + \alpha \left( \delta_{k1} \delta_{m1} \delta_{ij} + \delta_{i1} \delta_{j1} \delta_{km} \right) \\
& + \left( \mu_l - \mu_t \right) \left( \delta_{i1} \delta_{k1} \delta_{jm} + \delta_{i1} \delta_{m1} \delta_{jk} + \delta_{j1} \delta_{k1} \delta_{im} + \delta_{j1} \delta_{m1} \delta_{ik} \right) \\
& + \beta \delta_{i1} \delta_{j1} \delta_{k1} \delta_{m1}
\end{aligned} \tag{2.31}$$

The stress - strain relation takes of the form

$$\begin{aligned}
\sigma_{ij} = & \lambda \epsilon_{kk} \delta_{ij} + 2\mu_t \epsilon_{ij} + \alpha \left( \delta_{i1} \delta_{j1} \epsilon_{kk} + \delta_{k1} \delta_{m1} \epsilon_{km} \delta_{ij} \right) \\
& + \left( \mu_l - \mu_t \right) \left( \delta_{i1} \delta_{k1} \epsilon_{kj} + \delta_{j1} \delta_{k1} \epsilon_{ki} \right) + \beta \delta_{i1} \delta_{j1} \delta_{k1} \delta_{m1} \epsilon_{km}
\end{aligned} \tag{2.32}$$

Where  $\lambda$ ,  $\mu_l$ ,  $\mu_t$ ,  $\alpha$  and  $\beta$  are the generalized lame's constants. The components of  $[ \Gamma_{ij} ]$  can be calculated from (2.31). The results are

$$\begin{aligned}
\Gamma_{11} &= ( \lambda + 2\alpha + \beta + 4\mu_l - 2\mu_t ) n_1^2 + \mu_l (n_2^2 + n_3^2) \\
\Gamma_{22} &= \mu_l n_1^2 + ( \lambda + 2\mu_t ) n_2^2 + \mu_t n_3^2 \\
\Gamma_{33} &= \mu_l n_1^2 + \mu_t n_2^2 + ( \lambda + 2\mu_t ) n_3^2 \\
\Gamma_{12} &= ( \lambda + \alpha + \mu_l ) n_1 n_2 \\
\Gamma_{13} &= ( \lambda + \alpha + \mu_l ) n_1 n_3 \\
\Gamma_{23} &= ( \lambda + \mu_t ) n_2 n_3
\end{aligned} \tag{2.33}$$

The determinant matrix takes the following form,

$$\begin{vmatrix} b_2 n_1^2 + b_5 (1-n_1^2) - v^2 & b_3 n_1 n_2 & b_3 n_1 n_3 \\ b_3 n_1 n_2 & b_5 n_1^2 + b_1 n_2^2 + b_4 n_3^2 - v^2 & (b_1 - b_4) n_2 n_3 \\ b_3 n_1 n_3 & (b_1 - b_4) n_2 n_3 & b_5 n_1^2 + b_4 n_2^2 + b_1 n_3^2 - v^2 \end{vmatrix} = 0 \quad (2.34)$$

where,

$$\begin{aligned} b_1 &= \frac{\lambda + 2 \mu_t}{\rho} \\ b_2 &= \frac{\lambda + 2 \alpha + \beta + 4 \mu_1 - 2 \mu_t}{\rho} \\ b_3 &= \frac{\lambda + \alpha + \mu_1}{\rho} \\ b_4 &= \frac{\mu_t}{\rho} \\ b_5 &= \frac{\mu_1}{\rho} \end{aligned} \quad (2.35)$$

Equation (36) can be factorized resulting in the two equations,

$$b_5 n_1^2 + b_4 (1 - n_1^2) - v^2 = 0 \quad (2.36a)$$

and

$$\begin{aligned} & (b_5 - v^2) + (b_5 - v^2) \left[ (b_2 - b_5) n_1^2 + (b_1 - b_5)(1-n_1^2) \right. \\ & \left. + \left[ (b_1 - b_5)(b_2 - b_5) - b_3^2 \right] n_1^2 (1 - n_1^2) \right] = 0 \end{aligned} \quad (2.36b)$$

One possible wave speed in the direction  $n$  is given by,

$$v(n) = \left[ b_5 n_1^2 + b_4 (1 - n_1^2) \right]^{\frac{1}{2}} \quad (2.37)$$

The other two wave speeds are the positive roots of equation (2.36b). Once the velocities are known, the direction of particle motion

associated with each wave can be obtained from (2.30). It can be showed that the particle motion associated with the speed given by equation (2.37) is always transverse, where as those associated with other two speeds are neither longitudinal nor transverse. A detailed discussion of the properties of the waves for general direction of propagation was given by Hearmon [47].

For a typical graphite/epoxy composite containing 60% graphite fibers by volume, the Engineering constants are

$$\begin{array}{lll} C_{11} = 160.73 \text{ GPa} & C_{22} = 13.92 \text{ GPa} & C_{12} = 6.44 \text{ GPa} \\ C_{23} = 6.92 \text{ GPa} & C_{55} = C_{66} = 7.07 \text{ GPa} & C_{44} = 3.5 \text{ GPa} \end{array}$$

In the units of mm/ $\mu$ s the wave velocities for propagation in the xz-plane are calculated to be

$$\begin{array}{ll} v_{11} = 10.1 & v_{23} = v_{31} = 2.1 \\ v_{31} = 2.97 & v_{33} = 1.49 \end{array}$$

A polar diagram of the wave speeds as functions of propagation direction is sketched in fig 2.2.

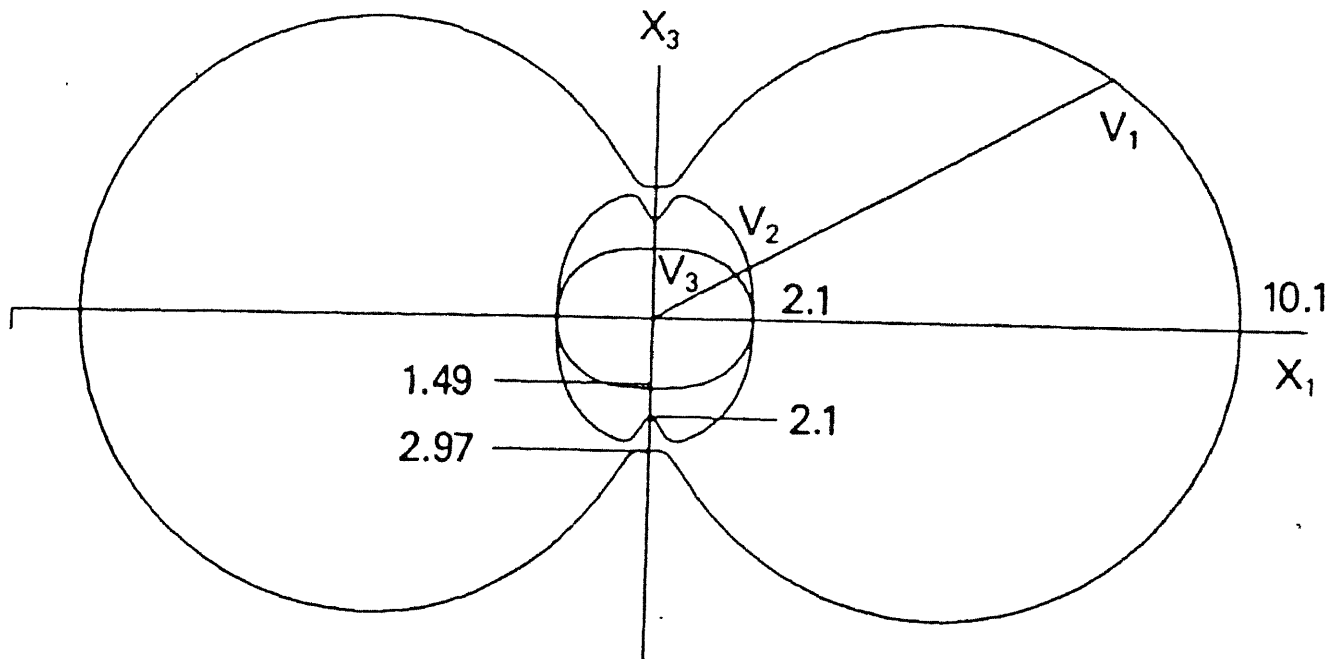


Fig. 2.2 Wave Speeds as Functions of Angle of Propagation in Graphite - epoxy Composite.

## 2.4 Propagation in a half-space

When an elastic wave encounters a boundary between two media, energy is reflected and transmitted (refracted) from and across the boundary. If the boundary is a free surface, pure reflections will occur. What distinguishes elastic wave-boundary interaction from other related fields is the phenomenon of mode-conversion. This describes the behaviour by which an incident wave, either compression or shear, is converted into both types on reflection.

### *Rayleigh surface Wave*

In an unbounded elastic media only two types of waves can be propagated. However, when there is a boundary, as in a half space problem, a third type of wave exists whose effects are confined closely to the surface. These are called Rayleigh surface waves and their effects decrease rapidly with depth and their velocity of propagation is smaller than that body waves.

By investigating the propagation in a half space the frequency equation for surface wave may be obtained as,

$$\frac{c^2}{c_2^2} \left( \left( \frac{c}{c_2} \right)^6 - 8 \left( \frac{c}{c_2} \right)^4 + (24 - 16k^{-2}) \left( \frac{c}{c_2} \right)^2 - 16(1 - k^{-2}) \right) = 0 \quad (2.38)$$

Where  $c$  is the surface wave velocity and  $k = 1/c_2$

Out of the three roots of the equation, it has been shown that for all real media ( $0 < \nu < 0.5$ ) there is only one real root. The resulting surface wave propagating with the velocity established from the above equation is the Rayleigh wave. An approximate expression has been developed for Rayleigh wave velocity, which is slightly less than shear wave velocity, given by,

$$\frac{c_R}{c_2} = \frac{(0.87 + 1.12 \nu)}{(1 + \nu)} \quad (2.39)$$

The particle motion can be shown to be elliptical in nature and retrograde with respect to the direction of propagation (i.e, it is counter-clockwise for a wave travelling to the right). The amplitude decreases exponentially away from the surface. Rayleigh waves are essentially two dimensional. Hence, energy associated with these waves will not disperse as rapidly as that of three dimensional waves of dilatation and rotation.

## 2.5 Waves in Layered Media

In many situations waves originate and propagate in a media having a layered structure, where interface between dissimilar materials exist. An important example of such a case is composite laminates. The impedance mismatch (the product of density and wave velocity) between the adjacent layers is responsible for the reflection, refraction and transmission of the waves. Interface waves may also generated. It has been shown that the existence of such a wave required that the shear-wave velocities of the two media has to be nearly the same. These interface waves are usually referred to Stonley waves in the literature.

Through composite materials are inherently inhomogeneous and anisotropic, when the scattering by defects which are large compared to the fiber dimension is considered, it may be assumed to be homogeneously orthotropic. In this case, the wavelengths involved are much larger than the fiber dimension.

## 2.6 SCATTERING OF ULTRASONIC WAVES

In this section the formal aspects of wave scattering by a single flaw are discussed. These aspects are independent of the specification of the inhomogeneity/flaw.

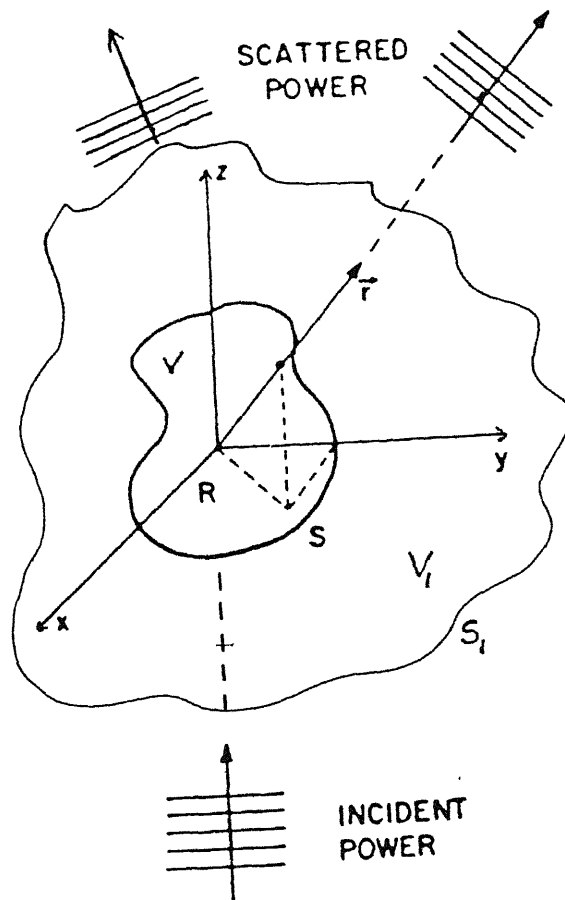
The scattering problem refers to a solution of the field equations in the regions interior or exterior to the volume  $V$  of the scatterer. The scatterer is excited by a source exterior to  $V$ . The field produced by the source in the absence of the scatterer is called the incident

field  $u^o$ . The difference between  $u^{tot}$ , the total field outside  $V$  in the presence of the scatterer and  $u^o$  is called the scattered field  $u^s = u^{tot} - u^o$ . All three fields,  $u^{tot}$ ,  $u^o$  and  $u^s$  separately satisfy the field equations in their respective regions of validity.

Scattering may be viewed as a two step process. According to Huygens principle, the incident field excites sources on the surface  $S$  of the scatterer, which in turn radiate to the exterior and the interior producing the scattered field and the interior field respectively. Since the sources of the scattered field are confined to  $S$ , physical considerations require that  $u^s$  must be finite and decay in a particular manner at distances far from  $S$ . This requirement is called the Sommerfeld radiation condition. A solution of the field equations, that simultaneously satisfies the boundary conditions on  $S$  as well as the radiation conditions at infinity, formally defines the scattered field. If the known sources are inside  $V$  or distributed on  $S$ , then the corresponding problem is called the radiation problem.

The basic scattering problem is shown in fig 2.3. In a material having elastic stiffness constants  $C_{ijkl}$  and density  $\rho$ , there exists a flaw defining a region of space  $R$  and having a surface  $S$ . The material inside the flaw has stiffness constants  $C'_{ijkl}$  and density  $\rho'$  which, in general, differ from those of the host material. For many cases of interest,  $C'_{ijkl} = \rho' = 0$  (void). In ultrasonic flaw detection experiments power generated by a piezo-electric transducer through a longitudinal/shear wave is directed towards the flaw. The presence of the flaw, however, prevents the incident power from propagating unhindered, and flaw selectively scatters part of the incident power into various directions. The transfer of energy takes place at least in both shear and compressional modes. In addition it was found that part of the incident wave energy striking a stress-free cavity is converted into a surface or boundary wave which "creeps" around the cavity radiating energy in all directions (like a light-house beam). The measurement of the scattered power into a given direction, relative to the incident power is of practical interest. Such a measurement may serve to differentiate between flaw geometries, and hence, would be an useful ultrasonic NDE measurement.





$$S = S + S_1$$

$$V^{\text{tot}} = V + V_1$$

Fig. 2.3 The Basic Scattering Situation; the Flaw Occupies Volume  $V$  Bounded by the surface  $S$ , embeded by  $S$  &  $S_1$ .

The physical quantity that measures the scattering effectiveness is the " cross section " of the flaw. This is related to, but not equal to, the effective geometrical cross-sectional area of the flaw.

An *intensity vector*  $I_i$  associated with a stress field  $\sigma_{ij}$  and a velocity field  $\dot{u}_i$  may be defined as,

$$I_i = \sigma_{ij} \dot{u}_j \quad (2.40)$$

The term intensity means the rate at which transfer of energy per unit area normal to the direction of propagation, i.e.,

$$I = I_i n_i \quad (2.41)$$

Where,  $n_i$  is the unit normal to the direction of wave propagation. For a plane wave incidenting along the z-axis, the incident intensity is calculated by considering the rate per unit area in which energy is carried across an infinite plane perpendicular to the z-axis. Thus,

$$I^o = \sigma_{3i}^o \dot{u}_i^o \quad (2.42)$$

The *power flux* or rate at which energy is carried across a surface A with unit normal  $n_i$  is given by,

$$\begin{aligned} P &= \int I_i n_i \, dA \\ &= \int n_i \sigma_{ij} \dot{u}_j \, dA \end{aligned} \quad (2.43)$$

For a given angular frequency, corresponding to a period T, the *total cross-section*  $P(\omega)$  is the ratio of the average power flux scattered into all directions to the average intensity of the incident fields.

$$P(\omega) = \frac{\langle P^s \rangle}{\langle I \rangle} \quad (2.44)$$

Where the angular brackets denote the time averaging,

$$\langle f(t) \rangle = \frac{1}{T} \int_0^T f(t) dt \quad (2.45)$$

For a given frequency, a measure of the fraction of incident power scattered into a particular direction is known as " *differential cross section* " and denoted by  $\frac{dP(\omega)}{d\Omega}$  where,  $d\Omega$  is the differential element of solid angle.

The average power flux, relative to the average total incident intensity directed across an element of area  $dA$  normal to  $n_i$  is given by,

$$dP(\omega) = \frac{\langle n_i \sigma_{ij} u_i^s \rangle dA}{\langle I^o \rangle} \quad (2.46)$$

At a distance  $r$  from the origin,  $dA = r^2 d\Omega$ . Thus,

$$\frac{dP(\omega)}{d\Omega} = \frac{\langle r^2 n_i \sigma_{ij} \dot{u}_j^s \rangle}{\langle I^o \rangle} \quad (2.47)$$

In more precise terms,

$$\frac{dP(\omega)}{d\Omega} = \lim_{r \rightarrow \infty} \frac{\langle r^2 n_i \sigma_{ij}^s \dot{u}_j^s \rangle}{\langle I^o \rangle} \quad (2.48)$$

The limiting process is necessary since differential cross section measurements are made at distances very far from the scatterer (the flaw). It has been found that as  $r \rightarrow \infty$ ,  $\sigma_{ij}^s$  and  $\dot{u}_j^s$  are of the order of  $\frac{1}{r}$ . Therefore, as  $r \rightarrow \infty$ , equation (2.48) represents that portion of the scattered power in  $d\Omega$  which is independent of the distance from the flaw.

Gubernatis et al. [48] have showed that the general expression for differential scattering cross section for a plane wave incidenting on an arbitrary shaped flaw in an isotropic medium as

$$\frac{dp(\omega)}{d\Omega} = \frac{\alpha (\lambda+2\mu) |A_i|^2 + \beta\mu |B_i|^2}{\alpha (\lambda+2\mu) |a_i|^2 + \beta\mu |b_i|^2}$$

where  $\alpha$  and  $\beta$  are the square of the wave numbers of longitudinal and shear wave respectively,  $|A_i|$  and  $|B_i|$  are the scattered wave amplitudes.  $|a_i|$  and  $|b_i|$  are the amplitudes of incident longitudinal and shear waves.

# CHAPTER III

## FORMULATION AND COMPUTER IMPLEMENTATION

This chapter deals with the finite element formulation of the governing wave equation which is a hyperbolic partial differential equation. Spatial and temporal discretization problems, accuracy and stability requirements were discussed. Transducer effects were taken into account to some extent. Methodology of differential cross-section measurement is given. A brief account of computer implementation of the model is discussed.

### 3.1 FINITE ELEMENT FORMULATION

#### 3.1.1 FORMULATION

The governing hyperbolic partial differential equation for a linear homogeneous and anisotropic elastic solid neglecting body forces is,

$$C_{ijkl} u_{k,lj} = \rho \frac{\partial^2 u_i}{\partial t^2} \quad (3.1)$$

The total potential of a linear elastic body using D'Alembert's principle is given by

$$\Pi = \int_V u_{i,j} \sigma_{ij} dV - \int_S u_i t_i dS + \int_V u_i \rho \frac{\partial^2 u_i}{\partial t^2} dV + \int_V u_i \xi \frac{\partial u_i}{\partial t} dV \quad (3.2)$$

where the first term is the strain energy, second term is the work done by the surface traction  $t_i$  and the third term is the work done by the inertia forces and the last term is energy dissipation due to the internal friction with  $\xi$  being coefficient of damping.

The finite element solution involves the discretization of the domain into a number of elements, approximation of the field values

interior to the elements in terms of its nodal values through the shape functions of the chosen element and the determination of the nodal values through the minimization of the above energy functional. Invoking the first variation of  $\Pi$ , i.e,  $\delta\Pi = 0$ , the following equation is obtained

$$\int_V \delta u_{i,j} \sigma_{ij} dV - \int_S \delta u_i t_i dS + \int_V \delta u_i \rho \dot{u}_i dV + \int_V \delta u_i \xi \dot{u}_i dV = 0 \quad (3.3)$$

For the field variable  $u_i$  in eqn.(3.3) it requires  $C^0$  continuous element. Approximating the field values  $u_i$  within an element in terms of the nodal values (U) as

$$\left\{ u^{(e)}(x,y,z,t) \right\} = \left[ N^{(e)}(x,y,z) \right] \left\{ U(t) \right\}^{(ne)} \quad (3.4)$$

where  $[N^e]$  is the set of shape functions.

The strain-displacement now, is represented as

$$\left\{ \epsilon^{(e)}(x,y,z,t) \right\} = \left[ B^{(e)}(x,y,z) \right] \left\{ U(t) \right\}^{(ne)} \quad (3.5)$$

where  $[B^e]$  is the strain-displacement matrix.

The constitutive equation is

$$\left\{ \sigma^{(e)}(x,y,z,t) \right\} = \left[ D^{(e)} \right] \left\{ \epsilon^{(e)}(x,y,z,t) \right\} \quad (3.6)$$

where  $[D^e]$  is the material property matrix and depends on the problem type whether it is plane stress or plane strain.

Combining equations (3.3) - (3.6) and several algebraic manipulations gives the equation of motion in the matrix form as

$$\left[ M \right] \left\{ \frac{\partial^2 u}{\partial t^2} \right\} + \left[ C \right] \left\{ \frac{\partial u}{\partial t} \right\} + \left[ K \right] \left\{ U \right\} = \left\{ F \right\} \quad (3.7)$$

where,

$$\begin{aligned} \left[ M \right] &= \sum \left[ M \right]^e = \int_{V_e} \rho \left[ N \right]^T \left[ N \right] dV \\ \left[ C \right] &= \sum \left[ C \right]^e = \int_{V_e} \xi \left[ N \right]^T \left[ N \right] dV \end{aligned} \quad (3.8)$$

$$\left[ K \right] = \sum \left[ K \right]^e = \int_{V_e} \left[ B \right]^T \left[ D \right] \left[ B \right] dV$$

$$\left\{ F \right\} = \sum \left\{ F \right\}^e = \int_{S_e} \left[ N \right] \left\{ t \right\} dS$$

The matrices  $[M]$ ,  $[C]$ ,  $[K]$  and  $\{F\}$  are well known as mass matrix, damping matrix, stiffness matrix and forcing vector, respectively. Mass, damping and stiffness matrices are sparse, symmetric and positive-definite. Since the matrices are very large and sparse, so they were condensed efficiently by skyline storage algorithm. Smith et al [31] have examined the accuracy of finite element solutions and found a ringing phenomenon which dies away only gradually. These oscillations can be suppressed efficiently in the presence of damping matrix. But it is a tedious job to find out  $\xi$  distribution. It was observed that in wave propagation problems the frequency of ringing is related to the size of the elements used in the FE mesh, and found to be predominant at frequencies of about 4-6 nodes per wavelength. But perfectly elastic formulation is incorporated in this analysis by taking 10 nodes per wavelength.

### 3.1.2 Spatial Discretization

For wave propagation problems low-order elements were recommended [36]. Because of this reason linear quadrilateral isoparametric elements have been chosen for spatial discretisation. A typical element is sketched in fig (3.1).

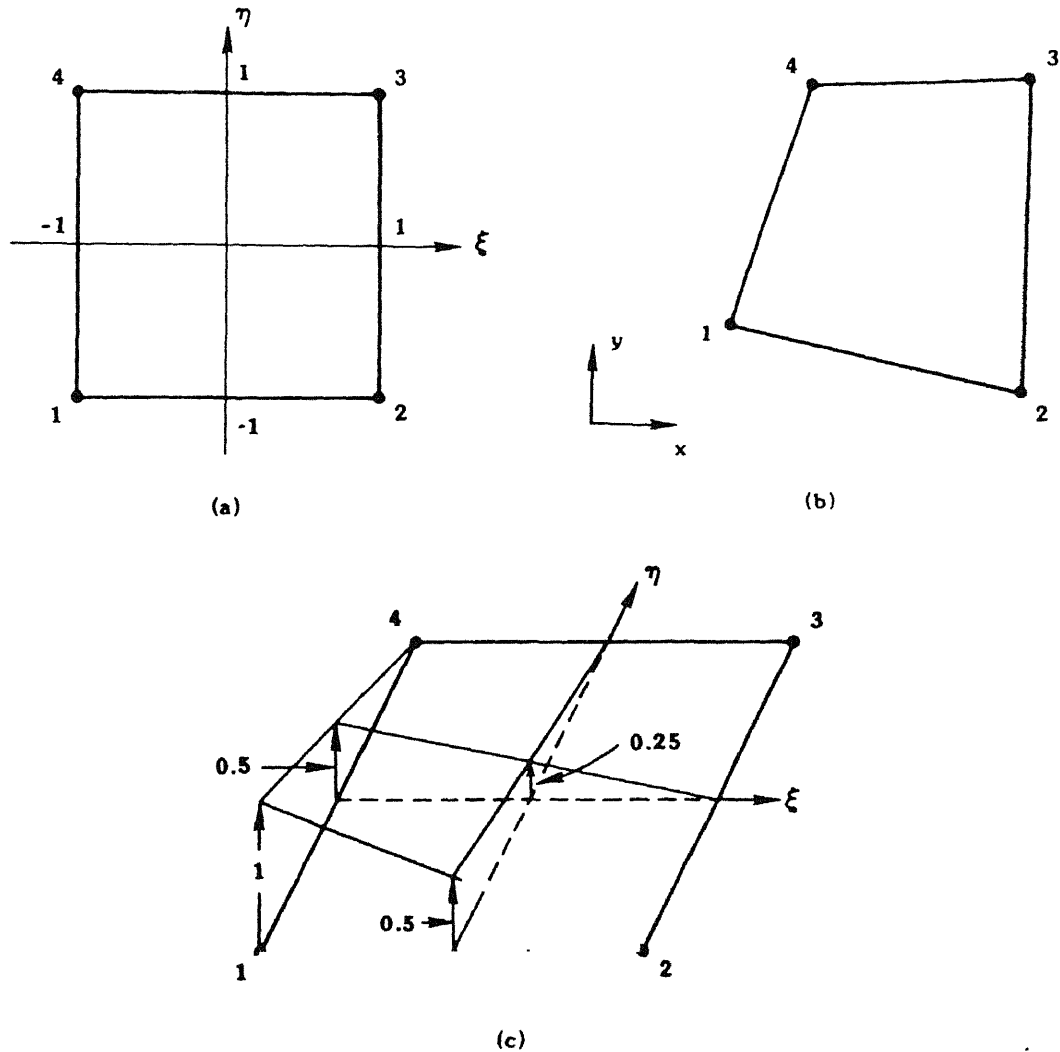


Fig. 3.1 (a) Natural Coordinate and Rectangular Parent Element.

(b) Isoparametric Element (Mapped on Cartesian Coordinate; Quadrilateral Element.)

(c) Shape Function.



### 3.1.3 TIME DISCRETIZATION

The system of linear, second order, and ordinary differential equations with constant coefficients (eqn. 3.7) has to be integrated in the time interval (0,T) by discretising the time variable as  $t_n = n \Delta t$ ,  $0 \leq n \leq N$  where  $\Delta t = T/N$ .

#### NEWMARKS METHOD

It was reported that Newmark's algorithm is more accurate than central difference scheme and therefore it is adequate to understand the physical phenomenon of wave propagation and to study arrival times and amplitude effects [35]. The Newmark's constant-average acceleration scheme makes the following assumptions,

$$\frac{^{t+\Delta t}\partial U}{\partial t} = \frac{^t\partial U}{\partial t} + \left[ (1-\delta) \frac{^t\partial^2 U}{\partial t^2} + \delta \frac{^{t+\Delta t}\partial^2 U}{\partial t^2} \right] \Delta t \quad (3.9)$$

$$^{t+\Delta t}U = ^tU + \frac{^t\partial U}{\partial t} \Delta t + \left[ (0.5-\alpha) \frac{^t\partial^2 U}{\partial t^2} + \alpha \frac{^{t+\Delta t}\partial^2 U}{\partial t^2} \right] \Delta t^2$$

where  $\alpha$  and  $\delta$  are parameters that can be determined to obtain integration accuracy and stability. Newmark [49] originally proposed an unconditionally stable scheme known as constant average acceleration method, in which  $\alpha = 0.25$  and  $\delta = 0.5$

In addition to the above difference equations, for solution of displacements, velocities and accelerations the equilibrium equations at time  $t+\Delta t$  are considered:

$$M \frac{^{t+\Delta t}\partial^2 U}{\partial t^2} + K ^{t+\Delta t}U = ^{t+\Delta t}F \quad (3.10)$$

Using equations (3.9) in (3.10) we obtain the following equation

for  $^{t+\Delta t}U$ ,

$$\left( M + \frac{\Delta t^2}{4} K \right) {}^{t+\Delta t}U = \frac{\Delta t^2}{4} {}^{t+\Delta t}F + M \left( {}^tU + \Delta t \frac{{}^t\partial U}{\partial t} + \frac{\Delta t^2}{4} \frac{{}^t\partial^2 U}{\partial t^2} \right) \quad (3.11)$$

It is seen that this is an implicit scheme and requires the factorization of the stiffness matrix.

#### 3.1.4 ACCURACY AND STABILITY CONSIDERATIONS

Numerical modelling of elastic wave equation introduces several errors due to time and space discretization. These errors can be minimized by the careful selection of spatial grid size and time step. At least eight nodes per shortest wave length are chosen to minimise the error with the spatial resolution. In order to represent all the frequencies to pass through the mesh uniform low order elements are chosen.

The time step size should be such that the wave travels less than the spatial grid size in one time step. In other words, the energy should not propagate right across one mesh volume in one step.

The stability conditions are related to the wave velocities by,

$$\Delta t = \frac{h}{c_m} \quad (3.12)$$

where  $h$  is the minimum spatial resolution and  $c_m$  is the maximum propagation velocity, i.e, that of dilation wave velocity for isotropic solids and maximum phase velocity of quasi-compression waves for anisotropic solids. Another criteria suggested are [27].

$$\Delta t \leq \frac{h}{(c_1^2 + c_2^2)^{0.5}} \quad \text{for isotropic solids.} \quad (3.13a)$$

where  $c_1$  and  $c_2$  are the compression and shear wave velocities.

$$\Delta t \leq \frac{h}{1.732 c_m} \quad \text{for anisotropic solids.} \quad (3.13b)$$

where  $c_m$  is the velocity of quasi-compression waves.

### 3.2 BOUNDARIES OF THE DOMAIN

The physical region modelled is very small compared with regions considered in any experiment. It was observed that in numerical modelling of wave propagation problems the presence of artificial boundaries introduces spurious reflections which contaminate the solution. The problem in this present work has been overcome by constructing a domain of sufficient size by properly locating the flaw so that the required solution is obtained before the reflections from the external boundaries arrive.

In the literature nonreflecting, absorbing and transmitting boundaries were proposed[25,50,51], so that very little reflections takes place. These techniques involve the superposition of solutions with different boundary conditions and thus much more costly than a single solution with respect to computational time and cost.

### 3.3 MODELLING OF INPUT PULSE

A main step towards the successful modelling of elastic fields associated with NDE is the generation of realistic pulsed ultrasonic waves through the use of piezo-electric transducers. Neglecting the internal transducer mechanisms, the necessary transient excitation pulse can be specified by either force or displacement variations across the aperture of the transducer. Of these two possible choices, force type boundary conditions are chosen in this present work. These force excitations will have an amplitude and polarizations imposed on them to represent the transducer pulse.

The forcing vector chosen is specified as shown in Fig (3.2) and mathematically it can be represented as,

$$F(x,y,t) = p a \delta(x) w(y) f(t-\theta(y)) \quad (3.14)$$

where

$p$  is the polarisation associated with  $F$

$a$  is the amplitude of forcing vector

$\delta(x)$  ensures that  $F$  is applied on the surface of the solid only.

$w(y)$  takes into account the possible non-uniform distribution of the force across the aperture. In other words, it acts as a weighting function a uniform distribution  $w(y)=1$

for  $-\frac{a}{2} < y < \frac{a}{2}$  is presently assumed.

$f(t-\theta(y))$  stimulates a realistic transducer signal that is to be determined experimentally by measuring the received transducer voltage signal in a pulse-echo experiment. The signal is subsequently digitized to be used as an excitation. A good analytical approximation is given by[52],

$$f(t) = \begin{cases} \left[ 1 - \cos(\omega t) \right] \cos(3\omega t) & t \leq 1 \mu s \\ 0.0 & t > 1 \mu s \end{cases} \quad (3.15)$$

where,  $\omega = 2\pi$  (transducer frequency). This approximation models the transducer with a harmonic time dependency modified by a cosine-shaped weight. The possible phase delay  $\theta(y)$  for beam steering purposes is set to zero.

The boundaries away from the transducer aperture are set to traction-free conditions i.e.,  $\sigma_{ij} n_j = 0$ .

The initial conditions for starting the iterations used are,

$$U(t=0) = 0$$

$$U(t=-\Delta t) = 0 \quad (3.16)$$

$$\frac{\partial U}{\partial t} (t=0) = 0$$

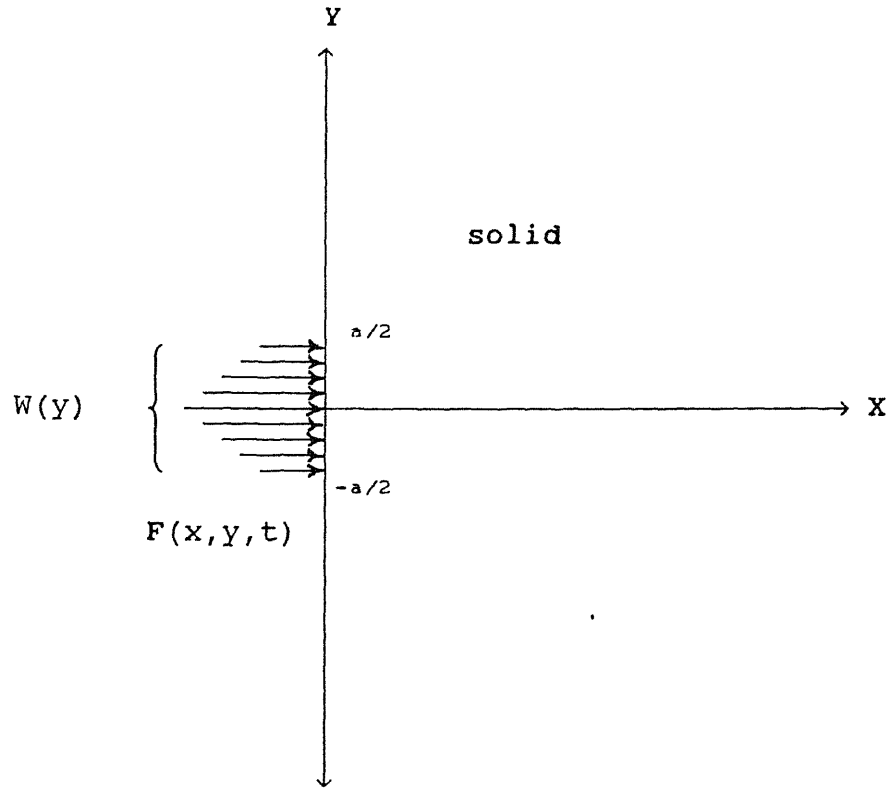


Fig. 3.2 Specification of force vector on boundary  
to simulate transducer pulse

#### 3.4 DETERMINATION OF SCATTERING PARAMETERS

Estimates of differential scattering cross sections can be easily obtained with this model. To obtain these cross sections, the calculations are first performed with the flaw present for the given source position and its polarisations. Reference calculations are then performed. These are the same as the original calculations in terms of mesh size used in the domain, time step, source location and duration of pulse application, but differ only in the absence of the defect. The vector displacements from the appropriate reference calculation are then subtracted from each original calculation at every mesh point and at all time steps. The resulting displacements are entirely due to the

scattering effects of the defect.

Mathematically,

$$\begin{aligned} u^{tot} &= \text{displacement field obtained with the defect} \\ u^{in} &= \text{incident field (obtained when there is no} \\ &\quad \text{defect)} \\ u^{scat} &= \text{scattered field} \\ &= u^{tot} - u^{in} \end{aligned}$$

The energy in the various pulses is proportional to the square of the displacements and so, it is a simplified measure of the energy scattered. So, the expression for the energy scattered is given by [28],

$$E = \int_{t_1}^{t_2} \left( u^2 + v^2 \right) dt \quad (3.17)$$

where  $u, v$  are the displacements at a detector. The integral is performed over the whole time trace i.e., from 0 to the A-scan limit. The integral here is performed using Simpson's rule. The value of displacements  $u, v$  at any point in an element are interpolated from the nodal values.

### 3.5 COMPUTER IMPLEMENTATION

The two-dimensional finite element code has been implemented on CONVEX C220 to model pulsed ultrasonic wave propagation in linear elastic solids with a scale of inhomogeneity. The block structure of the program consists of three parts : a preprocessor, a processor and a postprocessor.

The preprocessor generates the required data for the discretization of the domain. It consists of co-ordinates of nodes and the nodal connectivity of quadrilateral elements used for the

discretization. The material properties, problem type, transducer characteristics are also included in it. A graphics program was developed for drawing the finite element mesh and it also checks the connectivity of elements.

The processor is the main body of the code and models the wave propagation. It will predict the vector displacements at all nodes in the domain at all time steps using Newmark's algorithm. Separate routines were incorporated to calculate the strains and stresses in the elements. These can be used to find out the strain in the elements at different time instants. Similarly kinetic energy can also be calculated.

The postprocessor is a starbase graphics program. It visualizes the complete scattered wave field at any desired instant. A scan data can also be plotted. Differential scattered cross-sections can be drawn with graphics code.

## CHAPTER IV

### RESULTS AND DISCUSSION

This chapter presents the details of various simulations performed on homogeneous and composite materials with the Finite Element code being described in the earlier chapters. These results are shown in the form of A-scan plots, differential scattering cross-sections and complete wave field visualizations at different instants (snapshots) and thus giving ultrasonic testing.

#### 4.1 RESULTS FOR ISOTROPIC SOLIDS

Three cases have been studied for the homogeneous and isotropic medium. For each case both the longitudinal pulse and shear pulse interactions with the flaw are studied. Aluminium is chosen as the material. In all the finite element calculations only one half of the domain has been discretized taking the advantage of symmetry.

Four noded quadrilateral elements for spatial discretization and Newmark's algorithm for time marching were chosen in the present analysis [38]. Numerical experiments have been conducted to select the optimum spatial discretization and time step values. For selecting the maximum spatial discretization value the pulse arrival time at a particular location is compared with the theoretically computed value. The time step value has been obtained from the equation 3.13.

The Finite Element main processor output includes the x and y displacements at all nodes for each time step. These results are presented as "snapshots". A snapshot represents the displacement field ( either x or y ) at a particular time step, which is plotted normal to the plane of the two - dimensional domain. Incidentally this type of presentation shows the mode-conversion, diffraction and interface effects which are also observed in photoelastic experiments.

The scattered amplitudes of the displacements are obtained by



subtracting the incident field, which were obtained from a defect free plate, from the total field. In order to minimise the computational time, uniform mesh has been chosen for the defect free plate. The displacements at the corresponding nodes of the defective plate are calculated using interpolations. But some spurious displacement field is noticed in the snapshots which were taken before the start of scattering time. This important observation may be attributed to the dispersion of wave when it propagates through the finite element mesh. This phenomenon can be explained in the following physical terms:

Any transducer pulse signal contains all frequencies whereas the finite element mesh has a limit on frequencies it can describe [53]. Thus a pulse tends to broaden as it propagates, if there is an artificial boundary, caused by the expanding cell, there is reflection of the dispersing wavefront, which leads to noticeable effects. (An element which is incapable of describing a particular frequency may also act as an artificial boundary). In the absence of these reflections, dispersion leads to a stable waveform which is formed from the given input wave profile after a small number of time steps. This new waveform propagates without further detectable change in shape. In order to minimise this peculiar effect of wave propagation, the domain discretization of defect free plate is closely maintained with that of the plate with a defect.

In the present analysis the differential scattering cross-sections are plotted as the angular distribution of scattered component of wave amplitude. For this reason these plots can be better termed as a polar plot of scattered amplitudes. The angular distribution of scattered component of wave amplitudes are determined by observing the displacements at three to four mesh spaces away from the maximum size of the flaw. Final traces are obtained by integrating the  $u$  and  $v$  components of scattered displacements over the entire A-scan period, so as to cover the first few scattered signals. Obviously, waves will propagate back and forth along the flaw, so that some scattered energy will arrive later; it is in this respect that the present analysis differs from the analytical calculations.

The elastic constants of Aluminium are taken as :

$$E = 70 \text{ GPa}$$

$$\nu = 0.33$$

$$\rho = 2275 \text{ Kg/m}^3$$

The calculated compressional, shear and Rayleigh wave velocities in Al are :

$$c_1 = 6750 \text{ m/sec}$$

$$c_2 = 3375 \text{ m/sec}$$

$$c_R = 3150 \text{ m/sec}$$

TABLE 4.1

FE simulation details for various defects in isotropic solids

Problem	No. of elements	No. of nodes	$\Delta t$ $\mu\text{sec}$	$F_c$ M Hz	Flaw Size mm
1. Defect free	7500	7676	0.04	0.75	----
2. Surface Crack	7500	7691	0.04	0.75	15
3 WEDGE CRACK					
a. With wedge	6656	6839	0.04	1.0	15
b. Defect free	6656	6825	0.04	1.0	----
4. Drilled Hole					
a. With Hole	5722	5887	0.04	1.0	2.4 dia
b. Defect free	5632	5785	0.04	1.0	----

Care has been taken to use about twelve nodes per longitudinal wavelength. The domain modelled is of 30 mm x 80 mm for the defect free and surface crack modelling, 31.2 mm x 44.4 mm in the case of a wedge crack and 35 mm x 50 mm in the case of a hole. In each case of the defect, the pulse is polarised along x-axis and then along y-axis

to resemble the longitudinal and shear pulses.

#### 4.1.1 Propagation in defect-free isotropic solid

The geometry modelled is as shown in fig. 4.1 along with a typical finite element mesh. The transducer pulse width is assumed to be 4.0 mm and is uniformly distributed over the surface nodes situated above and below the symmetric portion.

Figs 4.2 and 4.3 shows the snapshots of X and Y displacement fields at different instants of time after the application of pulse (1 $\mu$ sec). At 1.8  $\mu$ s, which is just 0.8  $\mu$ s after the application of pulse, and the details were not clear. The next three plots (3.6, 5.0 & 6.0 $\mu$ sec) clearly show the fast and radially propagating compression wave front (Pressure wave, P) and the compressed or expanded parts are also seen. Outside the source no deformation exists. A very strong shearing deformation is observed (rotational wave, S) between the deformed area of the longitudinal waves and the undeformed area. These transverse waves propagate obliquely. Also a Rayleigh (Rl) wave propagating along the surface with a velocity slightly less than that of the shear wave is seen. At the instant of 6.0  $\mu$ sec the compression pulse has reached the back wall and is reflected with a negative reflection coefficient and is travelling towards the front side of the block.

In fact, real transducers produce more than one type of waves that they are designed to give, e.g. compression wave transducers also produce shear waves. So, the use of the waves generated by all the components of the incident wave field provides more information for defect characterization [26] .

#### 4.1.2 Rayleigh wave interactions with a surface crack

Surface breaking cracks (such as fatigue crack, debris) are the most commonly encountered flaws on the structural components. In the present analysis this crack is modelled as a narrow cut of essentially

zero width in the mesh. A schematic representation of the domain considered and the typical finite element mesh are as shown in the fig. 4.4. Two surface cracks assumed to be present in the model to make the domain symmetric.

It is observed from the previous result that a compression wave produces a strong surface/Rayleigh wave. Figs 4.5 and 4.6 show the X and Y displacement fields, when a wave polarised in X- direction interacts with the surface crack. Strong scattering of Rayleigh wave by the surface crack can be seen from the shots of 5.0  $\mu$ sec and 6.0  $\mu$ sec. Only a small part of the incident Rayleigh wave is transmitted beyond the surface crack.

Figs 4.7 and 4.8 show the waves generated entirely due to the scattering of Rayleigh wave by the surface crack. (These are obtained by subtracting the incident displacement field from the total field). As the incident Rayleigh wave reaches the crack corner, a part of its energy is reflected back to the transceiver (in pulse-echo mode) and the rest travels down the crack face as a Rayleigh wave. In addition there is also mode-conversion to compression and shear energy from the crack corner. The Rayleigh wave travelling down the crack face mode-converts itself to a shear wave at the crack tip which propagates into the material. The shot at 6.0  $\mu$  sec clearly visualises this and the radial distribution of mode-converted compression from the surface crack corner. This mode-conversion is in agreement with the experimental observation of Bond [26]. A schematic diagram of this Ultrasonic NDT is sketched in fig. 4.9.

A polar plot of scattered amplitudes for this case is shown in fig 4.10. The amplitude is seen to be maximum in the forward scattering direction rather than in the backward direction ( $180^\circ$ ). The lobe structure indicates that the apparent area, blocking the incident wave, in forward-scatter is much more than the back-scatter.

#### 4.1.3 Compression wave interaction with a surface crack

Figs 4.11 and 4.12 show the X and Y displacements when a wave polarised in a direction perpendicular to the propagation direction

(SV wave) interacts with the surface crack. The snapshot at  $3.6 \mu$  sec clearly shows the compression wave interaction with the surface crack. The strongly reflected Rayleigh wave and shear waves have in turn interacted with the incoming Rayleigh and shear waves respectively. The final shot shows the reflection of the pressure wave from the back wall. In the Y- displacement, the  $6.0 \mu$  sec shot shows the reflected compressive wave and the generated Rayleigh wave on the back wall.

The scattered X and Y displacements for this case are as shown in figs 4.13 and 4.14. Because of the interaction of compression wave with the surface crack, the strongly reflected compression, shear waves which are propagating into the material and the reflected Rayleigh waves which are propagating along the surface are clearly revealed in these snapshots. From the final snapshot, one can clearly see, that the angular distribution of the scattered shear wave, which originates at the crack tip, and also the curvature of the pressure wave front. This observation is in agreement with the photo elastic experiments [53] and a line diagram of the scattered wave fronts is shown in fig 4.15.

The reflected Rayleigh wave seems to be travelling outwards from the sides of the surface crack. In a practical situation, if two receiving Rayleigh wave transducers are placed on either side of the surface defect, the relative amplitude and the shape of the received Rayleigh pulses at the two receivers contain information about the orientation and size of the surface crack [26]. A schematic representation of this is as shown in fig. 4.16.

Fig 4.17 shows a polar plot of scattered amplitudes when a compression wave interacts with the surface crack. The curve seems to be similar in the forward and back-scatter except for their amplitudes. There is an enormous decrease in the scattered energy in the  $180^\circ$  direction compared to the  $0^\circ$  direction. As expected a relatively low amount of energy is scattered in  $90^\circ$  direction. The energy is likely to be maximum in the  $65^\circ$  direction in both forward and back-scatter.

#### 4.1.4 Compression wave interaction with a hole

Cylindrical defects like side drilled holes, voids are another class of structural encountered flaws. Fig 4.18 shows a typical finite element mesh generated to incorporate this type of defects. The hole is of 2.4 mm in diameter. The transducer pulse is of 3.2 mm in width.

Figs 4.19 and 4.20 show the X and Y displacement fields when a pulse, which is polarised along X-axis is applied, interacts with the hole. The differentiation of pressure and shear pulses is very clear. The complex interaction of Compression pulse with the hole is observed in the snapshot at 3.8  $\mu$ sec. The slightly reflected compression pulse is also seen here. The snapshot taken at 5.0  $\mu$ sec clearly visualises the incident wave and scattered wave fields.

Figs 4.21 and 4.22 shows the scattered X- and Y- displacement fields. There is no scattered field till 2.8  $\mu$ sec shot as there is no interaction of the wave with the hole. A high and complex scatter field is observed surrounding the hole at 3.8  $\mu$ sec shot. The scattered pressure pulse, which is propagating at a higher speed and radially distributed from the center of the hole, is followed by the mode converted shear pulse. The distinction between scattered compression and shear wave fronts is predominant in scattered Y-displacement field. The mode converted Rayleigh wave is not clearly seen in these plots.

The angular distribution of scattered component of wave amplitude is as plotted in fig 4.23. There is a sharp lobe structure in both the forward-scatter and back-scatter directions. The main contribution to this plot seems to be due to the scattered compression wave as it is also radially distributed.

Fig 4.24 shows the A-scan display at a point before the hole and 45° with the line of propagation. The compression pulse expected arrival time is 2.5  $\mu$ sec. The reflected pressure pulse, the mode converted shear pulse and the direct shear pulses can also be seen in the figure.

When the wavelength of the elastic wave is approximately equal to the diameter of the hole, the incident pulse would be expected to excite normal modes of vibration in the target. In order to study this a hole of diameter equal to 6.4 mm in a domain of 45mm x 58 mm is modelled. Figs. 4.25 and 4.26 show the X- and Y- displacement fields and Figs. 4.27 and 4.28 show the scattered X- and Y- displacements. When compared with the earlier case the scattered displacements are showing a wave(surface) which is creeping around the circumference of the hole and radiating energy in all directions. These creeping waves at an eigen-frequency match phases during repeated excursions round the hole circumference, and by constructive interference build up to resonance [26]. The effect of this is felt in the differential scattering cross-section shown in fig. 4.28, where two distinct lobes are seen. The scattered energy seems to be maximum along  $55^{\circ}$  direction in forward-scatter.

#### 4.1.5 Scattering of SV wave with a hole

To study the shear wave interaction with the hole, the transducer input is polarised in Y- direction and the wave is set to propagate along X- direction.

The scattered X- and Y- displacements are shown in figs 4.30 and 4.31 which are magnified greatly. The scattered field at 3.8  $\mu$ sec is due to the head wave interaction with the hole. The snapshot taken at 5.0  $\mu$ sec clearly reveals the radial distribution of mode-converted compression pulse and scattered shear pulse. Here also the creeping wave distribution is not clearly seen as the surface area available for its motion is less than that of the wave length.

Fig 4.32 shows the angular distribution of the scattered amplitudes. Here three sharp peaks are observed, two lobes in the forward-scatter and one in the back-scatter areas. These peaks may be due to the small size of the hole when compare with the incident pulse wavelength.

#### 4.1.6 Compression wave interaction with a wedge crack

A typical finite element mesh to model a wedge crack is shown in the fig. 4.33. The FE mesh is fine near the crack surface and is uniform away from the crack tip. The transducer pulse width is equal to the wedge length i.e., 15mm.

Figs 4.34 and 4.35 show the visualisation of X and Y displacement fields respectively when the compression pulse interacts with the crack surface. At 3.0  $\mu\text{sec}$  the compression wave front has just reached the crack surface. The snapshots followed by it (i.e at 3.8  $\mu\text{sec}$  and 4.8  $\mu\text{sec}$ ) clearly shows the scattered, incident and transmitted waves. The edge diffraction of the incident wave can also be seen.

The scattered field is visualised in figs 4.36 and 4.37 from the snapshots of 3.0  $\mu\text{sec}$  and onwards. Since the magnification factor used is quite large, so the distinction between reflected pressure pulse and mode-converted shear pulse is not very clear in fig 4.30. But the strong reflection of compression pulse may be sensed by transmitting transducer itself in the pulse-echo mode of testing. The distribution of scattered fields is very clear in Y displacement field. These scattered waves are sometimes called the edge waves as they emanate from the crack tip. The mode-converted Rayleigh wave seems to be present surrounding the wedge surface. But the available surface for its propagation is negligible, so it may again convert itself into the body pulses.

The angular distribution of scattered amplitudes is sketched in fig 4.38. Here three different plots are plotted, each one is computed at different radial distance. There is a complete similarity in these curve shapes, but the change is only in their amplitudes. As we go far away from the crack position, the amplitudes are decreased as is generally expected. There is no scattering at all in the  $90^\circ$  direction. The amplitudes are maximum at around  $50^\circ$  in both back-scatter and forward-scatter directions.



Fig. 4.39 shows the difference between the A-scan plots taken on the symmetric surface with and without the wedge crack. The direct and reflected pulses are noted in the figure. The input pulse amplitude is gradually decreasing in the absence of wedge crack at the point considered. The effect of input pulse force distribution is clearly seen in these plots.

#### 4.1.6 Scattering of Shear waves by a wedge crack

In order to study the shear pulse interaction with the wedge crack a pulse polarised in Y- direction is applied. The radial distribution of mode-converted shear pulse and reflected shear pulse can be observed in the scattered displacement fields shown in figs 4.40 and 4.41. The scattered field is more or less similar to the earlier case, except for the difference in the amplitude.

The angular distribution of scattered amplitudes are plotted as a polar plot in fig 4.42. There are two lobes in both forward and back-scatter plots. Very less scatter amplitude can be observed in both  $0^\circ$  and  $180^\circ$  directions. One can observe that a little amount of energy is scattered in the  $90^\circ$  direction. The area blocked by the crack in forward-scatter is much higher than that of back-scatter direction.

#### 4.2 RESULTS FOR COMPOSITE MATERIAL

Composite materials are anisotropic in nature and in the present analysis it is assumed that it is homogeneous and orthotropic, for the purpose of studying the wave interaction with flaws which are much larger than fiber size. The composite material chosen for the analysis is Graphite/Epoxy, the material properties of which are given below. Symmetry has been incorporated in all the scattering geometries modelled to simplify the finite element discretization.

The properties of Graphite/Epoxy are,

$$\begin{array}{lll} E_l = 181.0 \text{ GPa.}, & E_t = 10.3 \text{ GPa.}, & G_{lt} = 7.17 \text{ GPa.} \\ \nu_{lt} = 0.28 & \nu_{tt} = 0.42 & \rho = 1580.0 \text{ kg/m}^3 \end{array}$$

The corresponding orthotropic elastic constants for 2-D analysis can be calculated to be,

$$\begin{aligned} C_{11} &= 181.8 \text{ GPa.}, & C_{12} &= 10.34 \text{ GPa} \\ C_{22} &= 10.34 \text{ GPa.}, & C_{44} &= 3.63 \text{ GPa} \\ C_{66} &= 7.17 \text{ GPa.}, & C_{23} &= 3.09 \text{ GPa} \\ C_{16} &= C_{26} = 0.0 \text{ GPa} \end{aligned}$$

Due to the anisotropy of the material the propagation velocities for each wave are different in different directions. The analytical calculations of the phase velocities for Graphite/Epoxy laminate in different directions can be calculated using Green-Christoffel equations (Eqn 2.25). Some salient values are tabulated in Table 4.2. The calculated values of maximum and minimum phase velocities and the corresponding wavelengths of quasi-longitudinal (QL) wave are given below. The QL wave has a maximum velocity at  $90^\circ$ , i.e., along the direction of lowest stiffness and minimum at  $5^\circ$ .

$$\begin{aligned} C_{mxql} &= 10700 \text{ m/sec.}, & C_{mnql} &= 2468 \text{ m/sec} \\ \lambda_{mxql} &= 10.7 \text{ mm.}, & \lambda_{mnql} &= 2.5 \text{ mm} \end{aligned}$$

The corresponding values for quasi-transverse (QT) wave are calculated as,

$$\begin{aligned} C_{mxqt} &= 2698 \text{ m/sec.}, & C_{mnqt} &= 2130 \text{ m/sec} \\ \lambda_{mxqt} &= 2.7 \text{ mm} & \lambda_{mnqt} &= 2.13 \text{ mm} \end{aligned}$$

The maximum is at an angle of  $12^\circ$  and minimum at  $0^\circ$  and  $90^\circ$ .

TABLE 4.2

Angle : deg	$C_{ql}$ :m/sec	$C_{qt}$ :m/sec	Angle : deg	$C_{ql}$ :m/sec	$C_{qt}$ :m/sec
0.0	2559	2130	50.0	8337	2284
10.0	2910	2427	60.0	9352	2175
20.0	4221	2440	70.0	10106	2175
30.0	5695	2400	80.0	10570	2142
40.0	7098	2345	90.0	10726	2130

The shortest wavelength was found to be 2.15 mm. for the frequency of 1 MHz used. It was taken care to use seven nodes per shortest wavelength for discretization. It was found that the solutions are stable for the resolution using the Newmark's integration scheme. The size of the domain modelled is 30mm x 80 mm in all cases. The details of various simulations are given in Table 4.3.

TABLE 4.3

FE simulation details for various defects in composites

Problem	No. of elem.	No. of nodes	$\Delta t$ $\mu$ sec	flaw dimension mm
1. Drilled Hole				
a. With Hole	6162	6332	0.04	3.2
b. Defect Free	6072	6230	0.04	-----
2. Delamination				
a. With Delamina	7500	7691	0.04	12.0
b. Defect free	7500	7676	0.04	-----

It was found that for the faster QL wave, the displacements along

the fibers are prominent and the wave profile of the same is stretched along the fiber direction. For the slower wave QT the displacement perpendicular to the fibers are found to be prominent [38]. This is the case where the transducer is modelled as a line source with a sinusoidal excitation for one full cycle. In the present analysis the transducer modelling is as described in eqn. 3.14 and the band width of the wave is just equal to the major dimension of the defect considered.

#### 4.2.1 Scattering by a hole in a layered composite material

The wave interaction by a drilled hole in a cross-ply laminate made of Graphite/Epoxy has been studied. In the first ply the L-T (Longitudinal and Transverse) properties and in the second ply T-T properties of the material are used. In the first ply the X-axis is along the fiber direction. The hole position is modelled at the interface of the layers.

In the first layer the material is highly anisotropic and the QL and QT wave velocities are different in different directions. [Table 4.2]. The second layer is isotropic in the plane considered and the longitudinal and transverse wave velocities are calculated to be 2560 m/sec and 2130.0 m/sec respectively.

Figs 4.43 and 4.44 show the X and Y displacement fields when the transducer pulse polarised along the propagation direction interacts with the hole. The different shapes of the wave profiles can be observed in the two layers even at the 6.0  $\mu$ sec shot when the wave has crossed the hole. A careful observation reveals a sudden change in the displacements at the interface. The wave propagation is at an angle to the fiber direction in the first ply L-T. In the 8.4  $\mu$ sec shot, the scattered wave has reached the front wall in the L-T laminate where as there is an interference of scattered waves with the back wall echos in T-T ply.

The scattered X and Y displacements were shown in Figs 4.45 and 4.46. The scattered displacements are highly direction oriented in the first ply and are radially distributed in the second layer. Multiple

reflections can be observed from the hole surface to the front and back walls of the domain.

Fig 4.47 shows the polar plot of the scattered amplitudes. In order to eliminate the scattering from the back and front walls, the integrated values of scattered displacements up to 8  $\mu$ sec are only considered. When compared with the isotropic case, it contains many lobes. The lobes are very narrow in the back-scatter. The scattered amplitude is seen to be maximum in the back-scatter i.e. along  $180^\circ$  and the next maximum is likely to occur along  $90^\circ$ .

#### 4.2.2 Scattering of SV pulse by a hole in L-T & T-T laminate

Figs 4.48 and 4.49 show the X and Y displacements when the applied pulse is in perpendicular to the propagation direction. The X-displacement is predominant in the longitudinal direction in L-T lamina and it is seen to be radial in the T-T ply. Even at the 5.0  $\mu$ sec shot also one can observe the scattering from the hole. The sudden change in the wave fronts is very clear at the interface. The Y-displacement profile is very interesting. As such the X displacement of the QL wave is seen to be propagating along the Y-axis in the L-T lamina. A clear distinction of QL and QT waves is not there in these snapshots.

The scattered X and Y displacements are shown in Figs 4.50 and 4.51. The scattering is predominant here right from the 6.0  $\mu$ sec shot, i.e. from the first few micro seconds itself, as the X displacement is maximum along the fiber direction. This elongation of wave front in a particular direction explains the phenomenon of beam skewing in ultrasonic testing of anisotropic materials. Here also the scattered waves are radially distributed from the hole surface in the second ply T-T.

A polar plot of scattered displacements is plotted in Fig. 4.52. It also has contained many lobes like structures. The scattered energy is seen to be maximum along  $50^\circ$  direction. Next maximum is likely to occur along the  $90^\circ$  direction.

A- scan display at a point near to the hole and at  $45^0$  to the line of propagation (in the first ply) is shown in fig. 4.53. When compared to the results of Jalleel [38], wherein the force pulse was at a point, the effect of distributed input force pulse is noticed from these plots.

#### 4.2.3. Scattering by delamination in a layered Composite Material

The wave interaction by delamination in a cross-ply laminate made of Graphite/Epoxy has been studied. The geometry of the ply is shown in the fig. 4.54. For the first ply T-L properties of the material and for the second ply T-T properties are used.

The X and Y displacement fields at different times are shown in Fig. 4.55 and Fig. 4.56 respectively. The evolution of QL wave into first medium is visible from the first two snapshots. The reflection of QL wave from the side walls is visible from the third and fourth shot. As the transverse direction of both fibers is coinciding with the propagation direction, the effect of interface is not seen in these plots. It can be noticed from the third shot that there is a strong scattering of QT wave from the delamination crack. Also observed is the effect of pulse input pulse band width.

The scattered X and Y displacement fields are shown in Fig. 4.57 and Fig. 4.58. The scattered Y displacement is slightly radially distributed in the T-T ply, whereas the X displacement is predominant perpendicular and along the fiber direction in both the plies. There is not much change in the distribution of scattered X and Y displacements.

Differential scatter curve for this interaction is as shown in the fig 4.59. It is also having lobes like structure. The scattered energy is seen to be negligible or zero along the  $90^0$  direction. As observed in the scattered displacements the scattered energy is dominating in both  $0^0$  and  $180^0$  directions, which can be sensed by the transmitter itself in the pulse-echo method.

A- scan display with and without interface crack at an inside

point is shown in fig. 4.60. For the sake of comparison the X- and Y-displacement values with and without the interface crack are shown. The direct and the reflected QL wave is marked in the figure. The presence of QT wave is not felt in this A- scan.

#### 4.2.4. Scattering of SV wave from an interlaminar crack in T-L & L-T Laminates

The scattering of a pulse, which is polarised in a direction perpendicular to the propagation direction, when it interacts with an interlaminar crack in a T-L and T-T cross ply laminate are as shown in figs 4.61 and 4.62. Here also the scattered amplitudes are seen to be maximum along the interface.

Fig 4.63 shows the angular distribution of scattered displacement amplitudes. The scattered power appears to be predominant in  $135^{\circ}$  direction. When compared with the earlier case, a considerable amount of energy is reflected in this case along  $90^{\circ}$  direction. Only a little amount of energy is scattered in  $0^{\circ}$  and  $180^{\circ}$ .

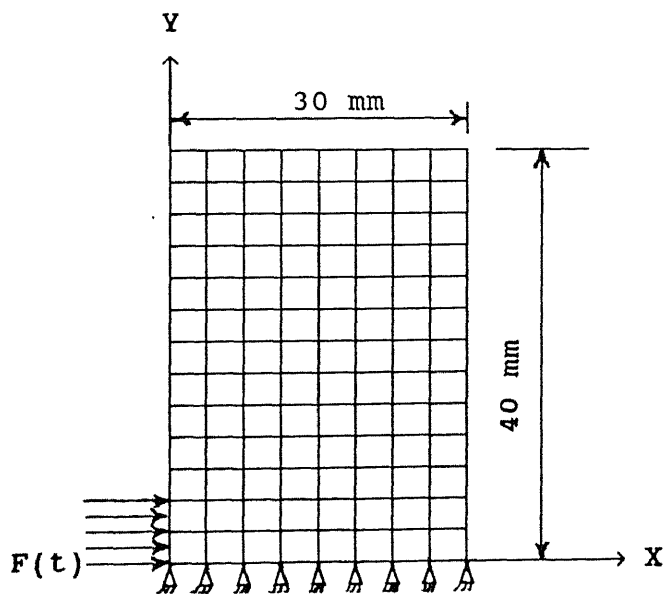
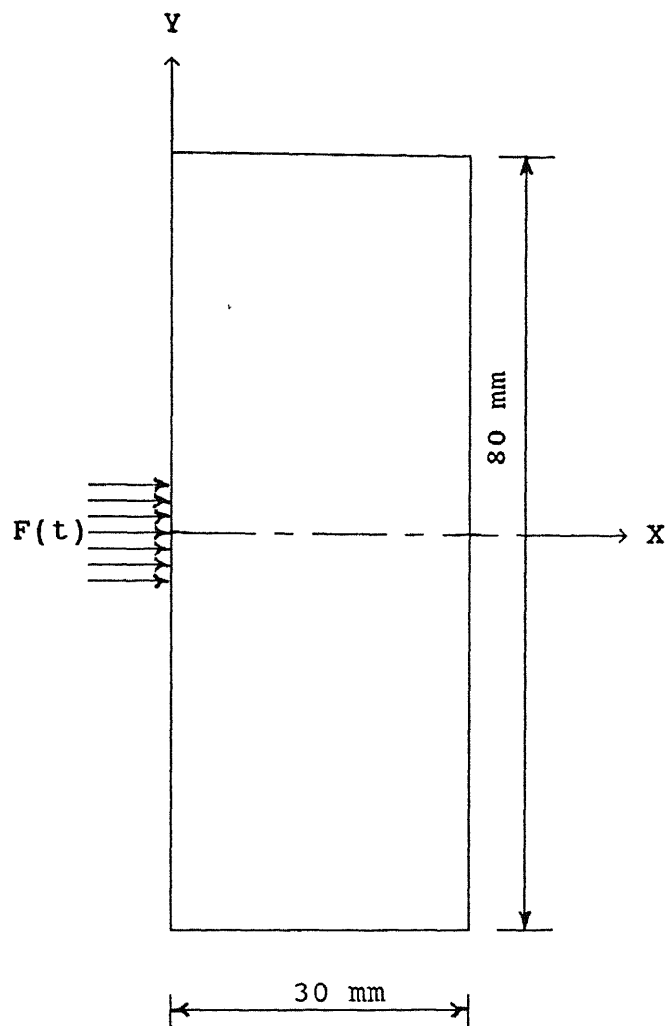


FIG. 4.1 GEOMETRY OF DEFECT-FREE ISOTROPIC SOLID



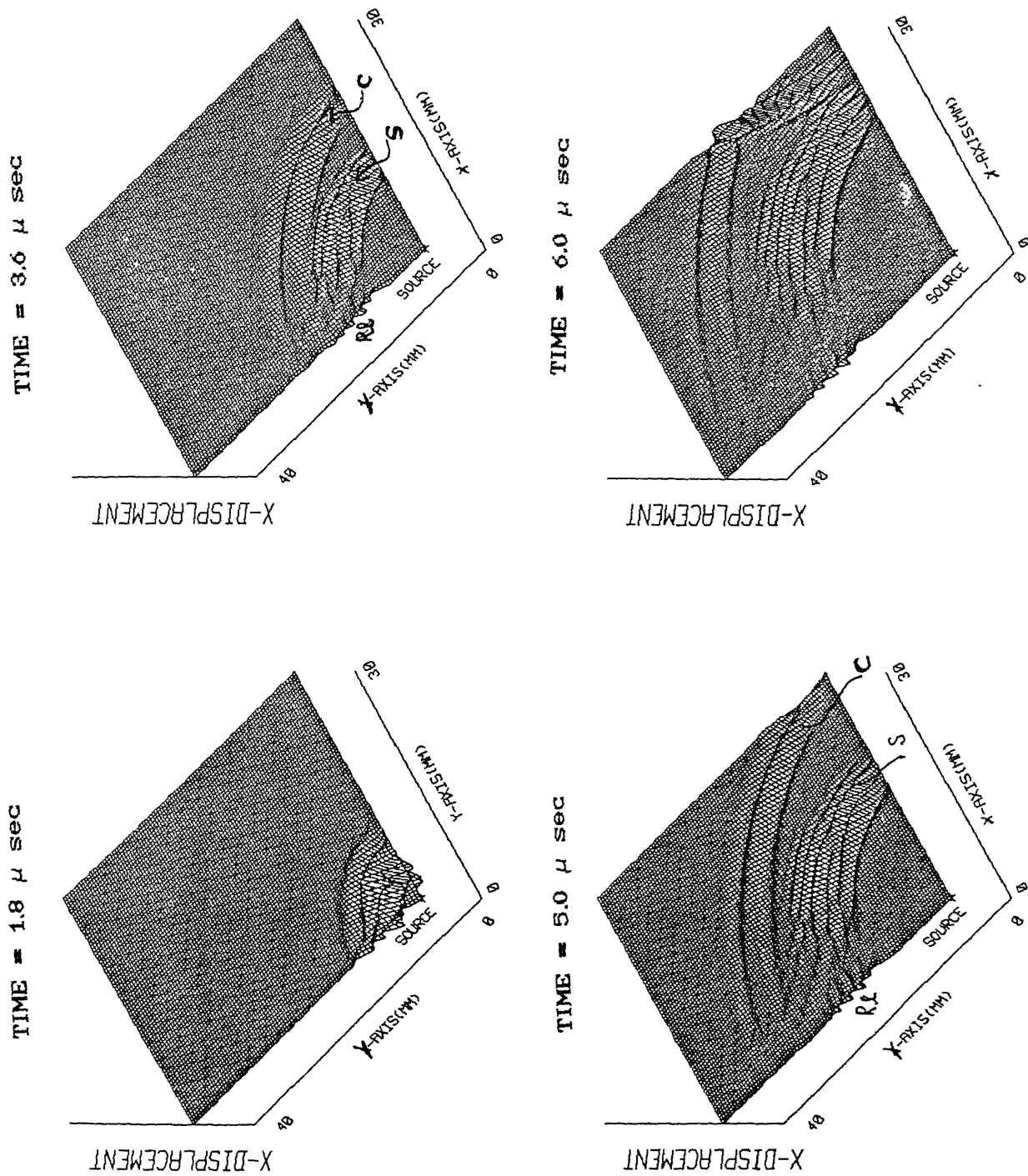


Fig. 4.2 X - Displacement Field for Defect-free Isotropic Solid.

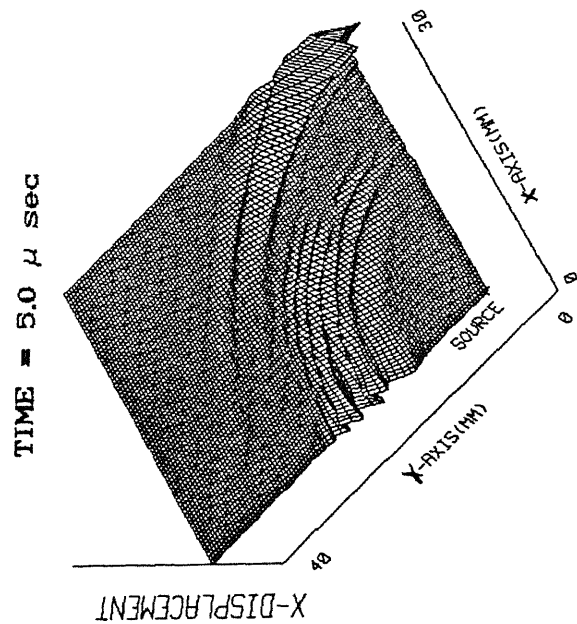
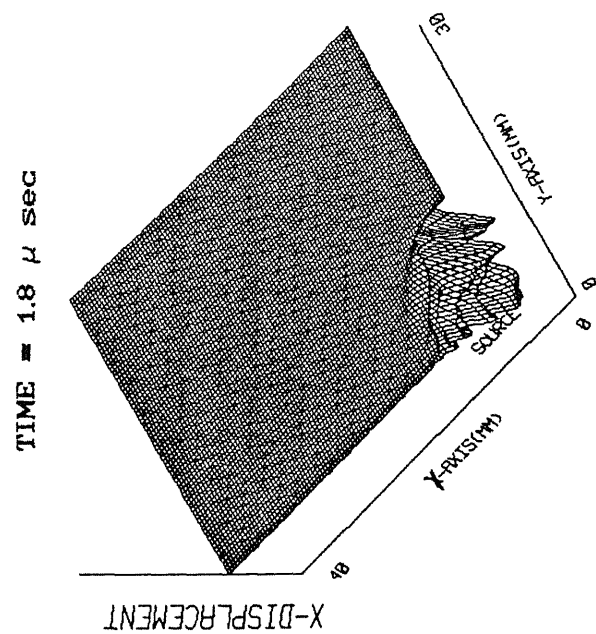
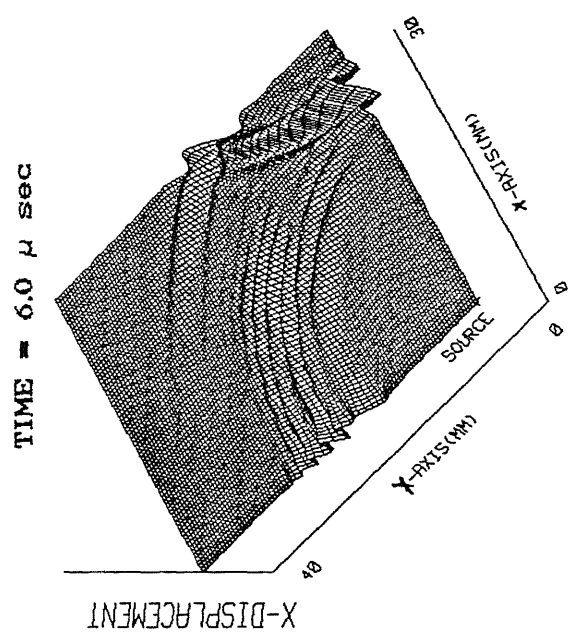
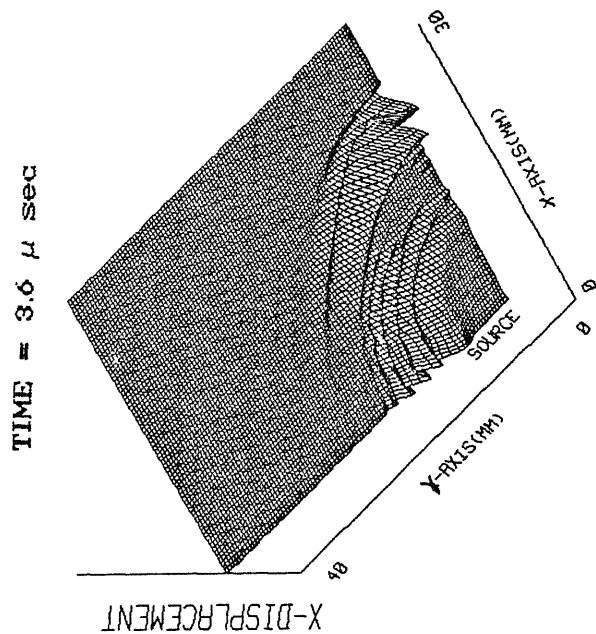


Fig. 4.3 Y - Displacement Field for Defect-free Isotropic Solid.

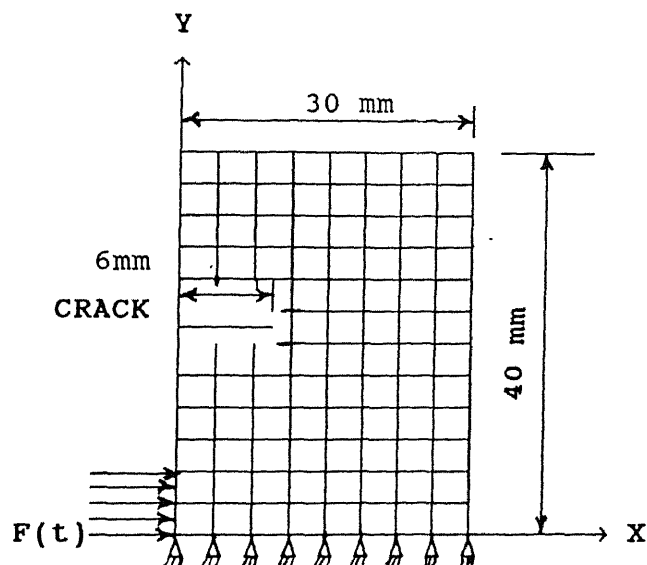
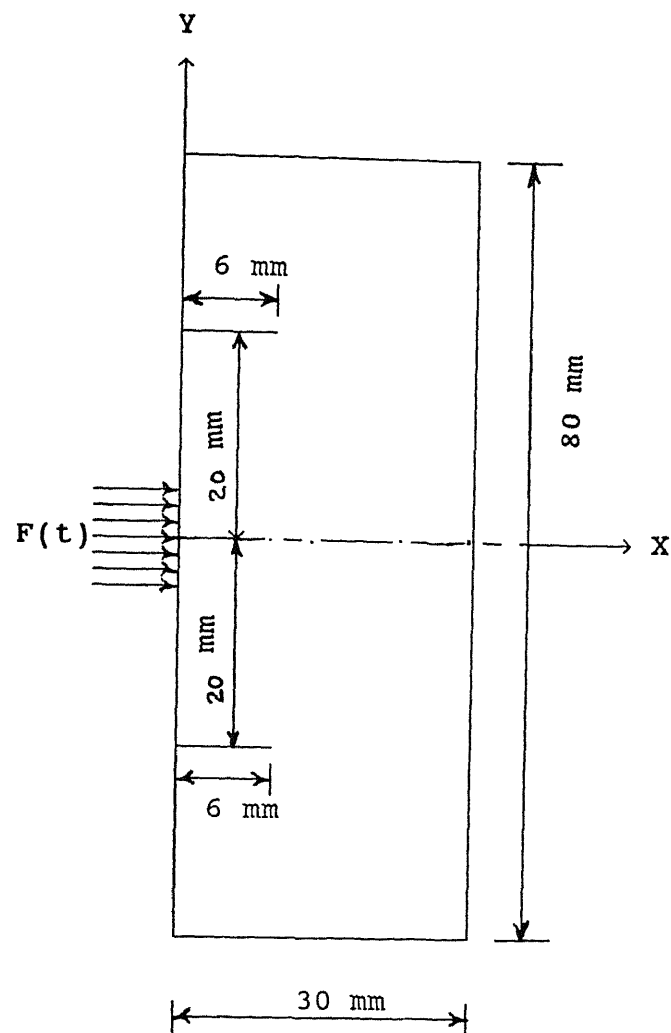


FIG. 4.4. GEOMETRY OF ISOTROPIC SOLID WITH A SURFACE CRACK

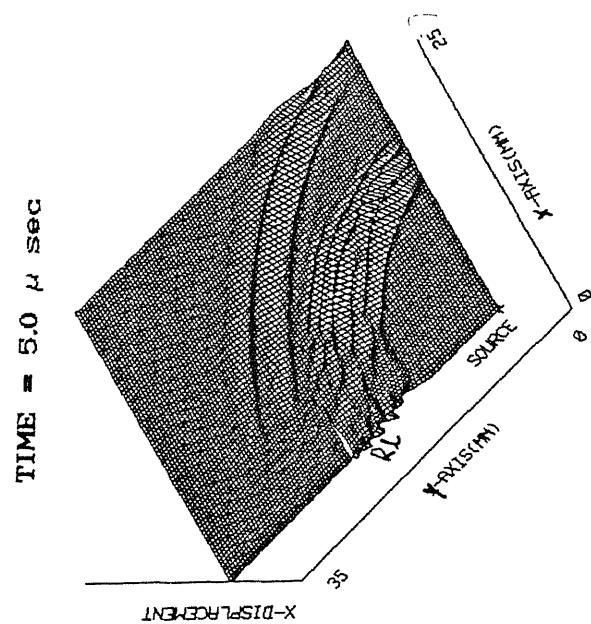
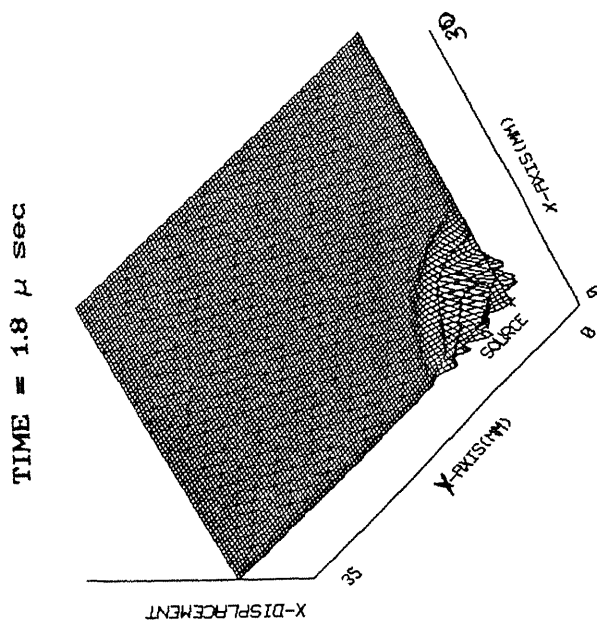
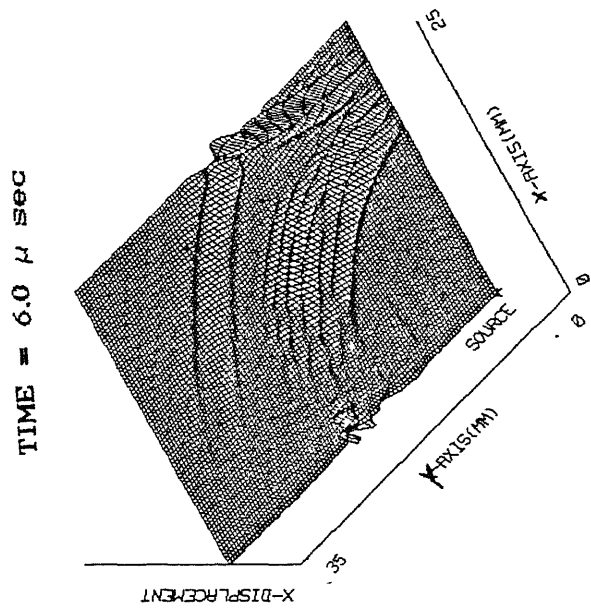
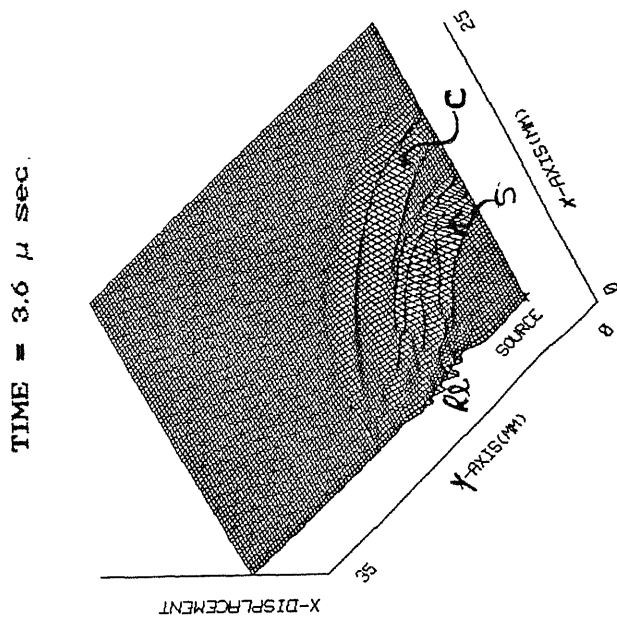


Fig. 4.5 X-Displacement: Rayleigh Wave Interaction with a Surface Crack.

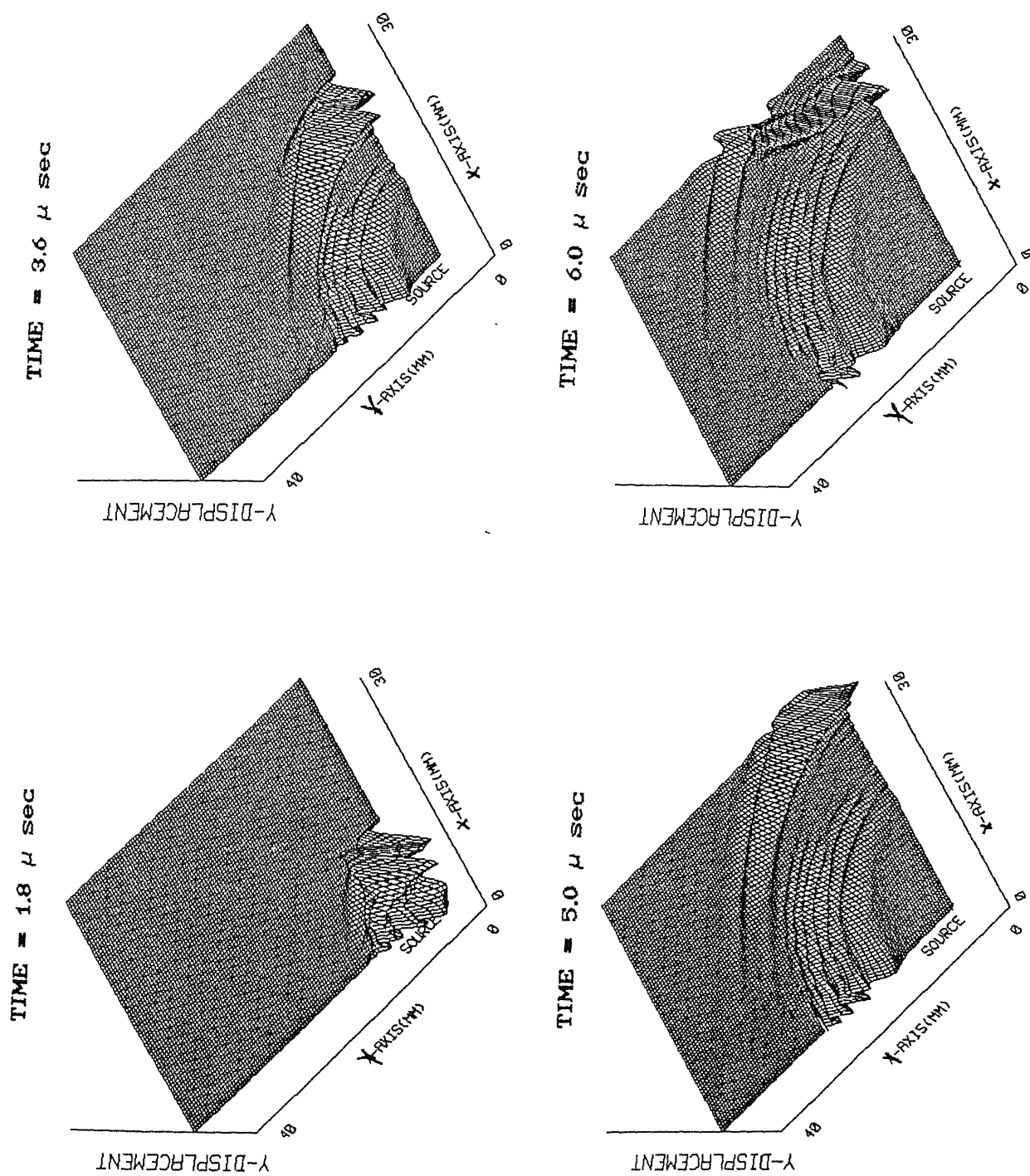


Fig. 4.6 Y-Displacement: Rayleigh Wave Interaction with a Surface Crack.

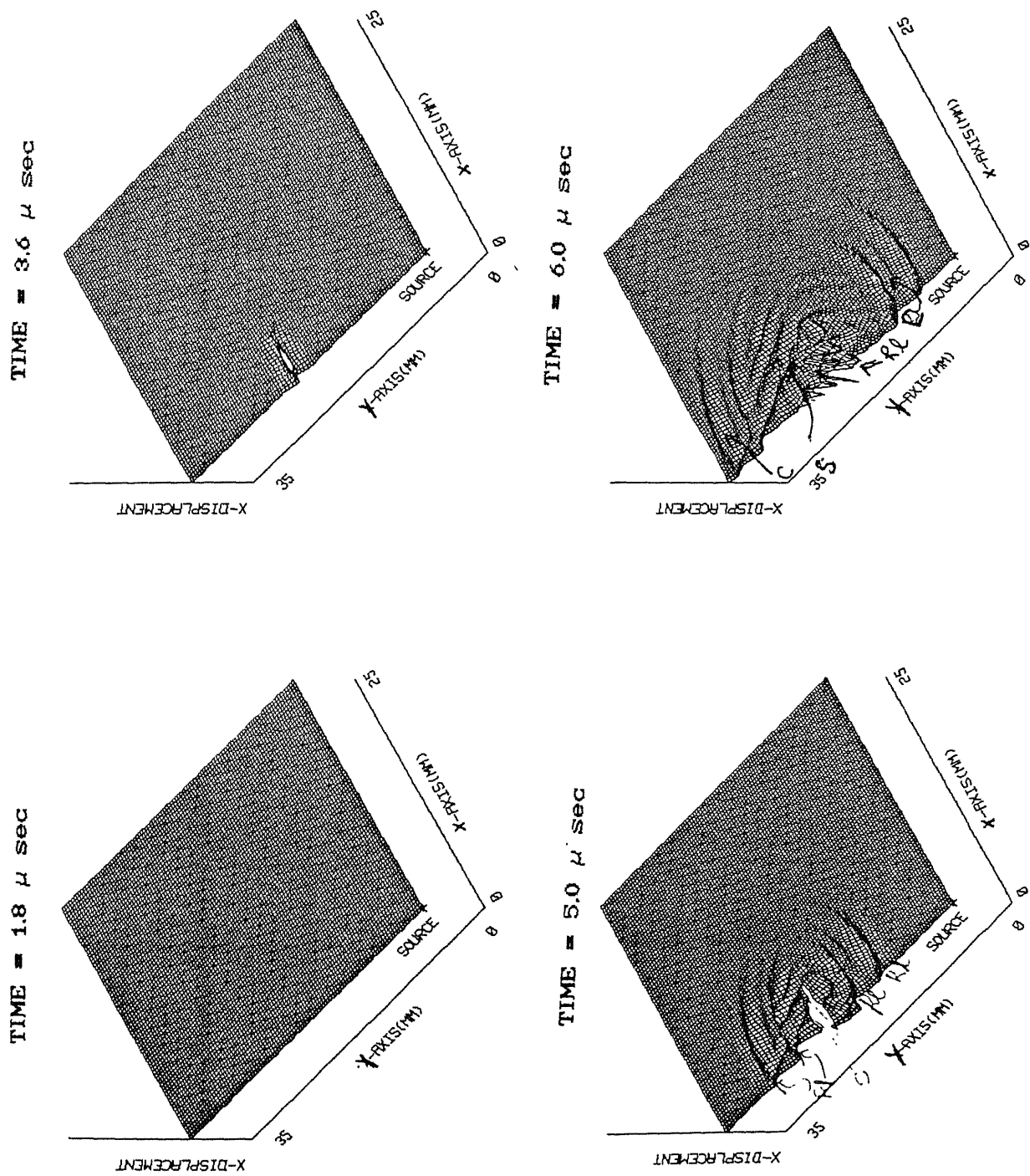


Fig. 4.7 Scattered X-Displacement Field: Rayleigh Wave Interaction with A Surface Crack.

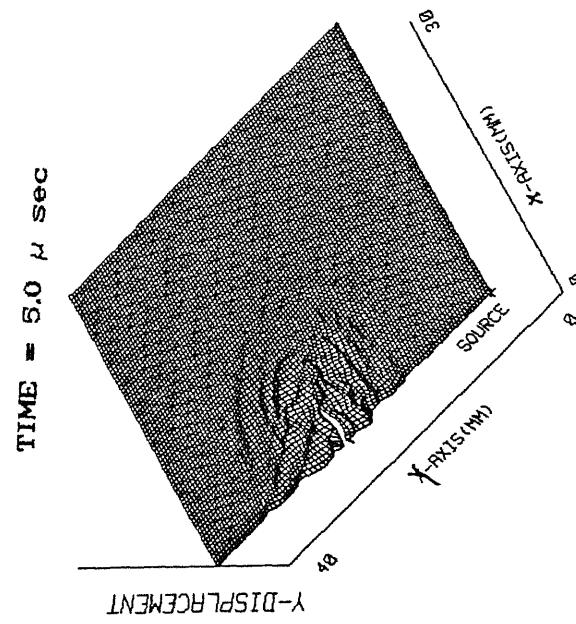
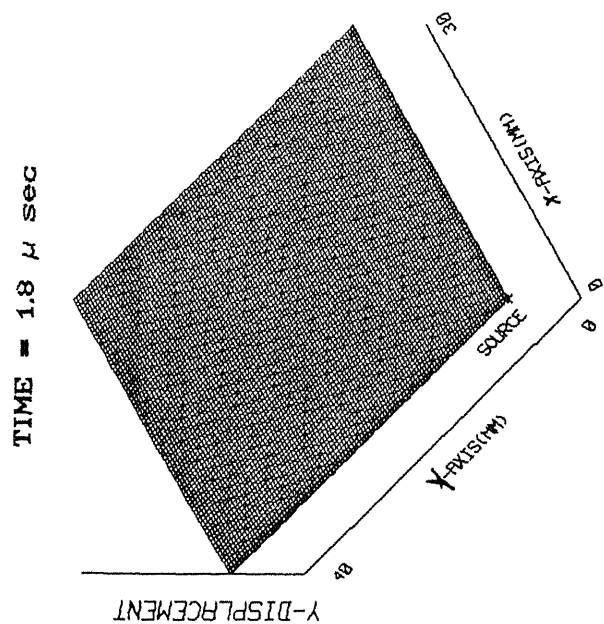
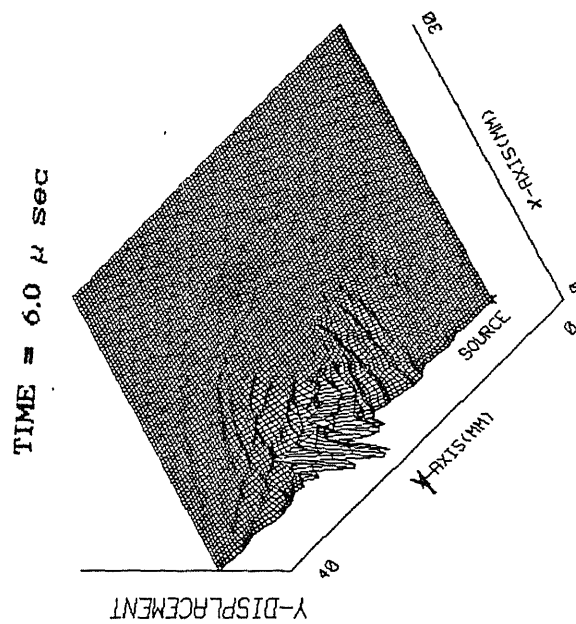
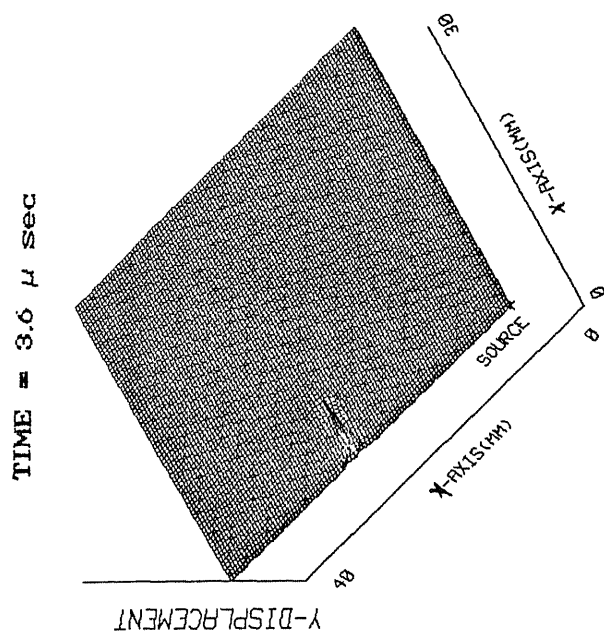


Fig. 4.8 Scattered Y-Displacement Field: Rayleigh Wave Interaction with A Surface Crack.

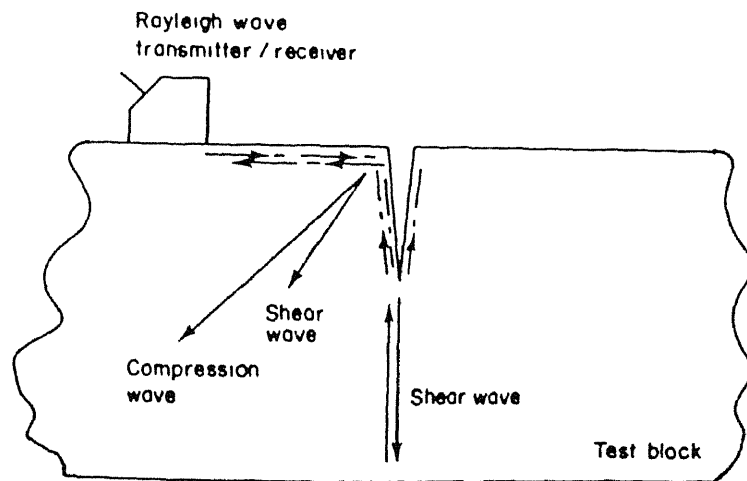


Fig. 4.9 Wave Field Components which result from the interaction of pulsed Rayleigh Waves with A Surface Crack.



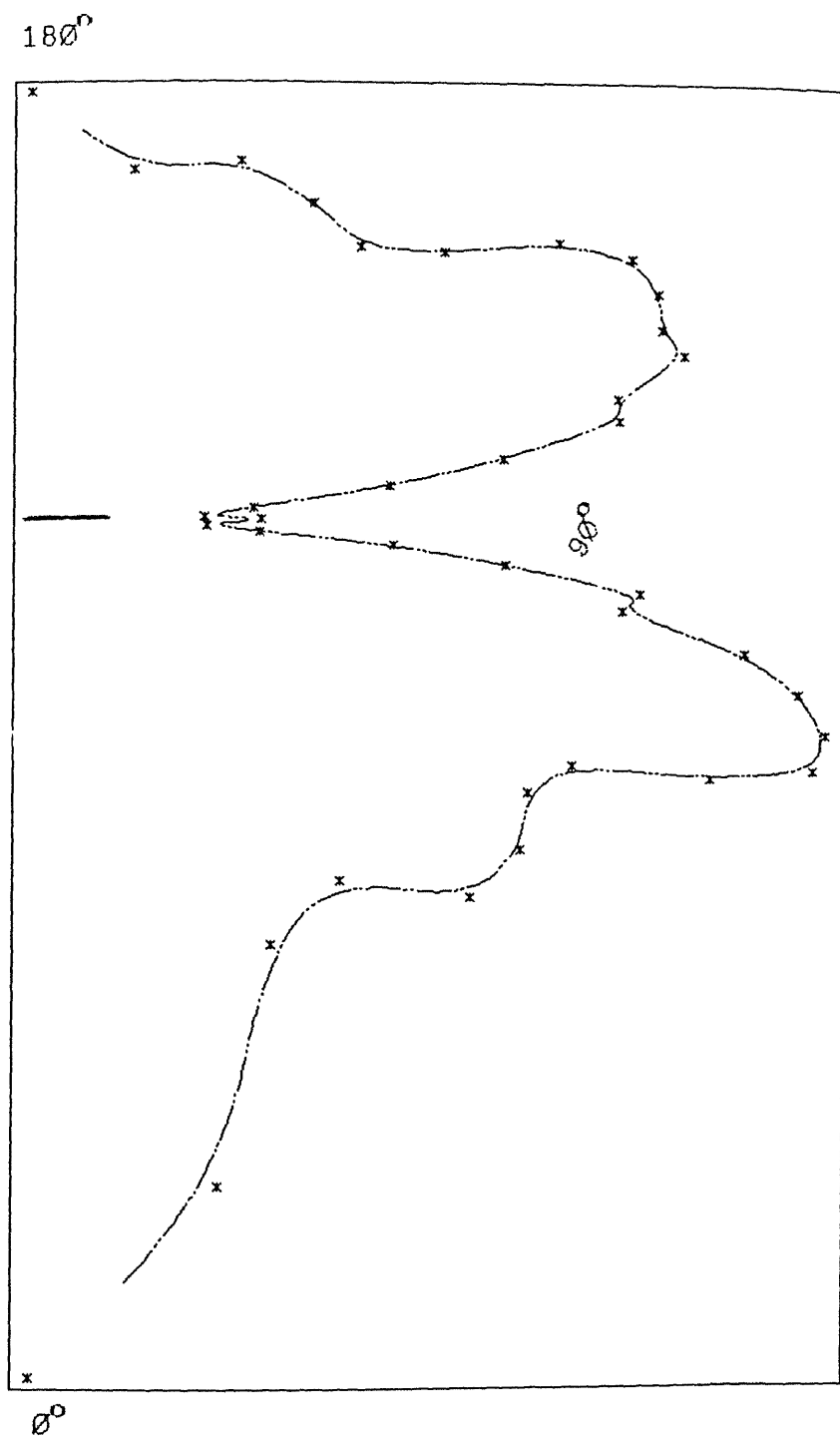


Fig. 4.10 Polar Plot of the Scattered Amplitudes by A Rayleigh Wave Interaction with A Surface Crack.

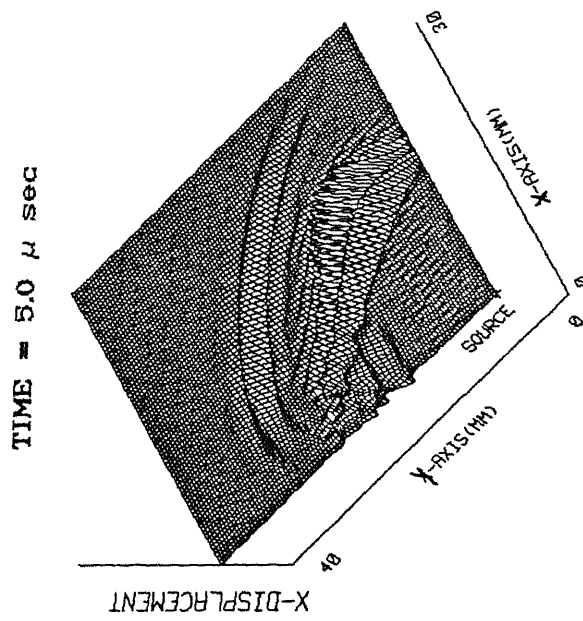
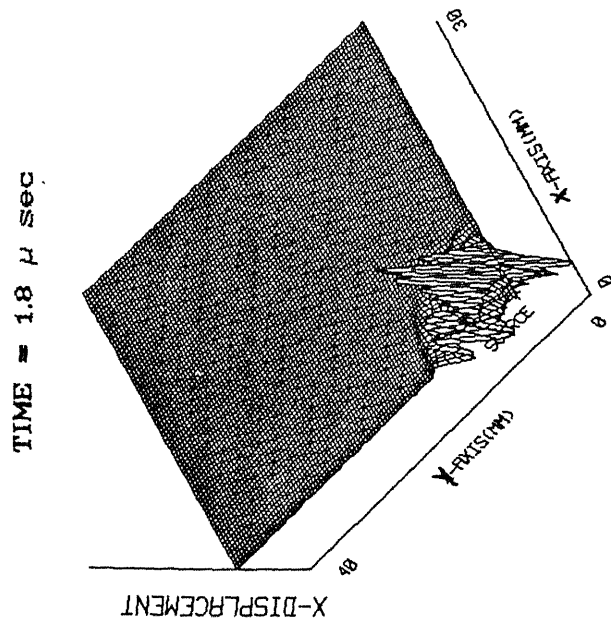
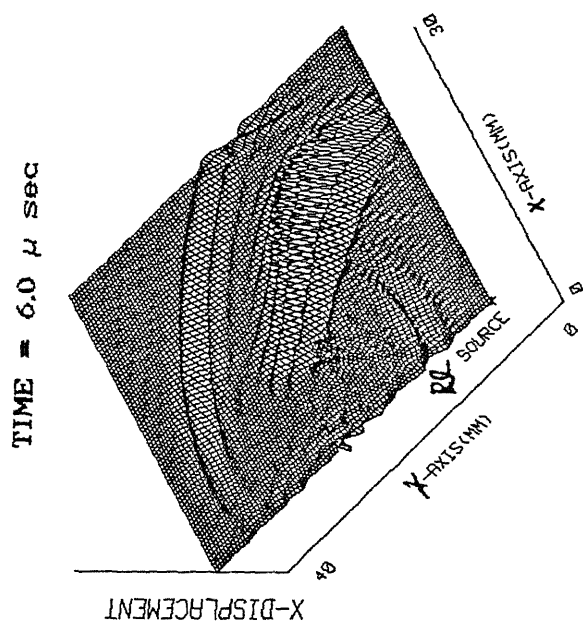
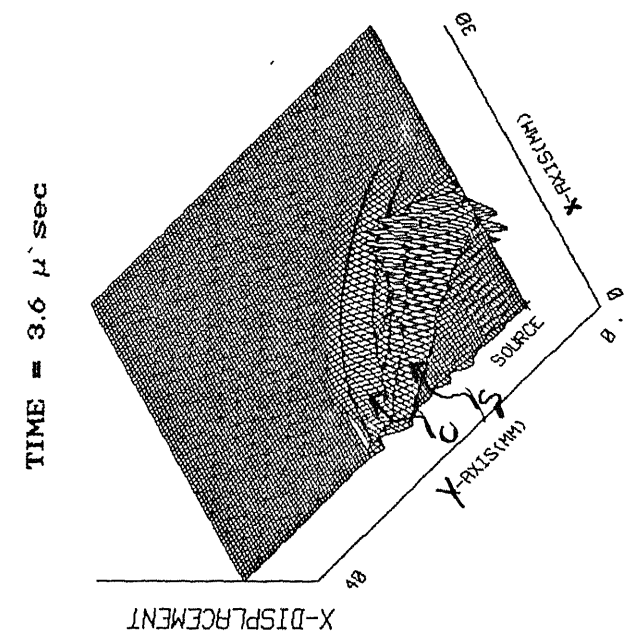
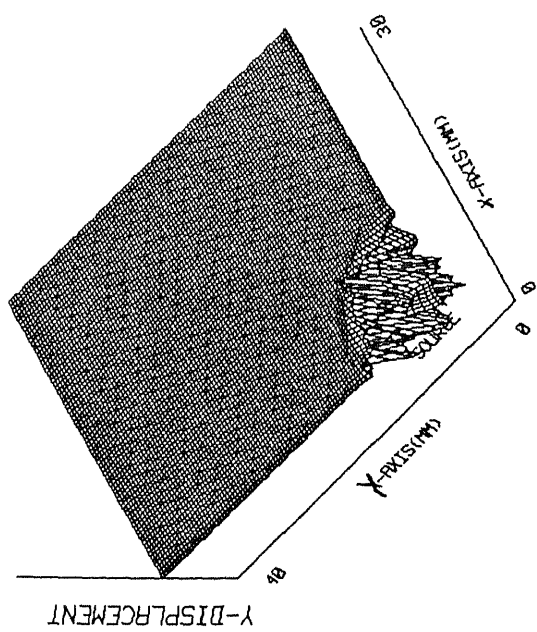
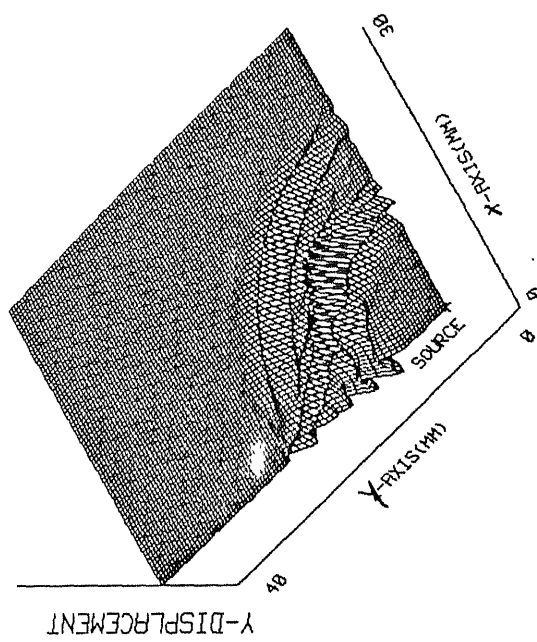


Fig. 4.11 X-Displacement Field: Compression Wave Interaction with A Surface Crack.

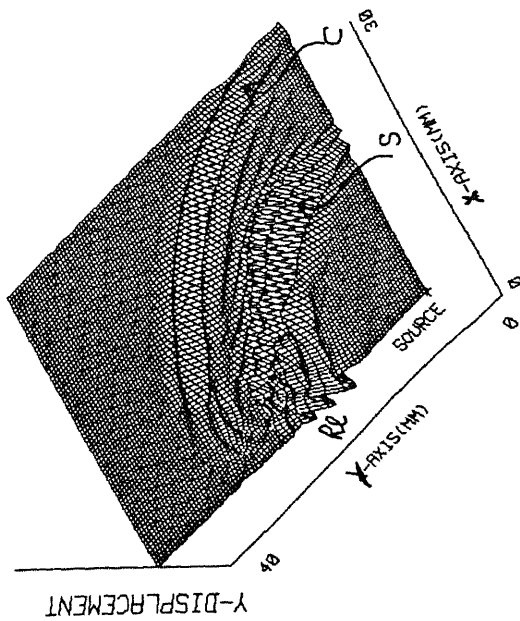
TIME = 1.8  $\mu$  sec



TIME = 3.6  $\mu$  sec



TIME = 5.0  $\mu$  sec



TIME = 6.0  $\mu$  sec

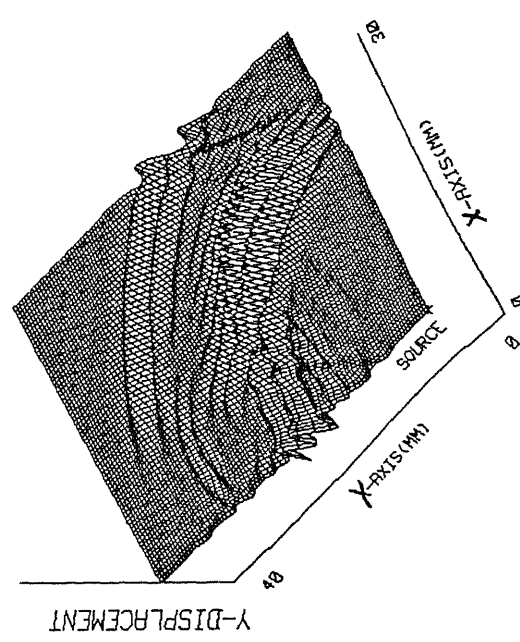


Fig. 4.12 Y-Displacement Field: Compression Wave Interaction with A Surface Crack.

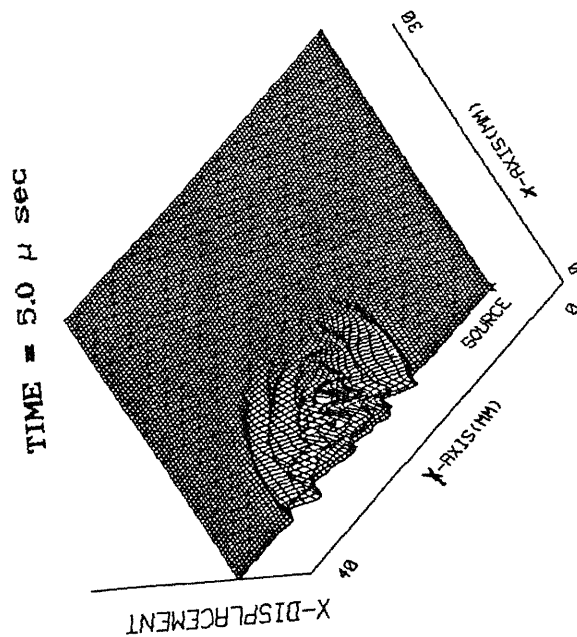
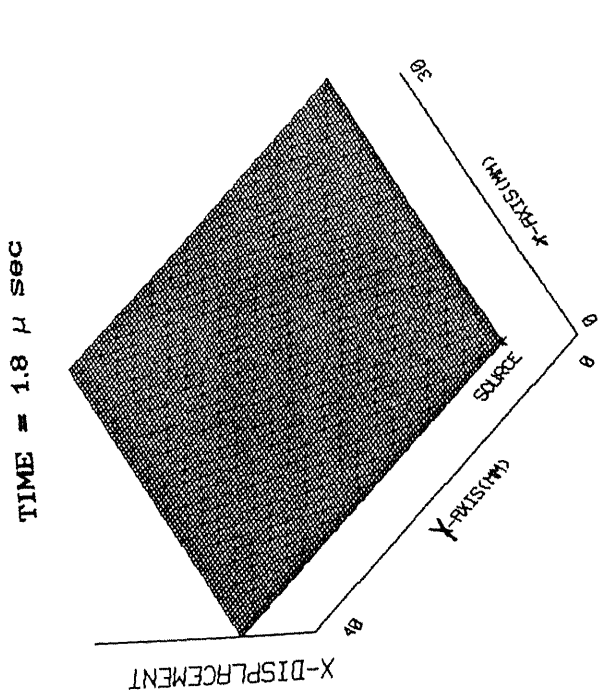
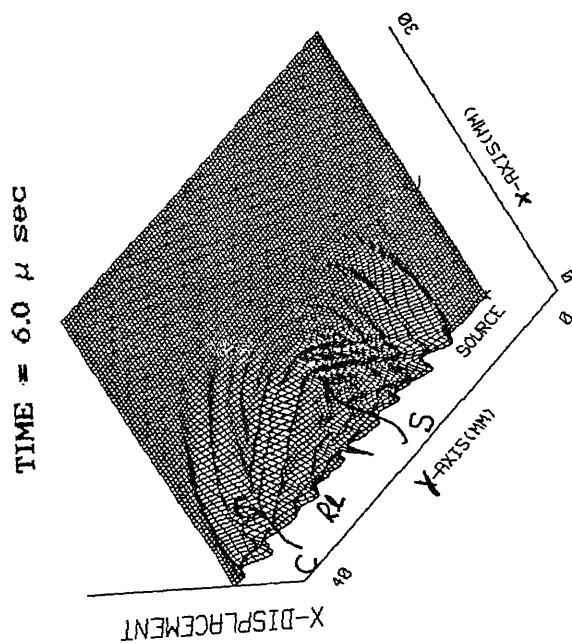
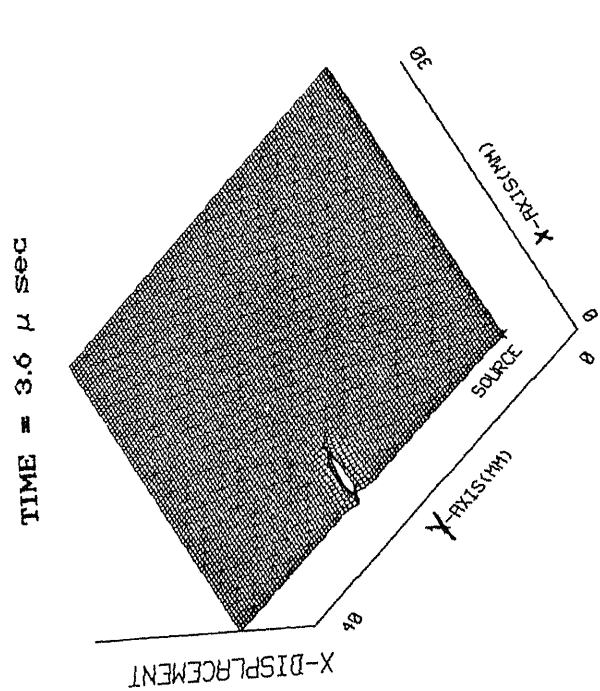


Fig. 4.13 Scattered X-Displacement Field: Compression Wave Interaction with A Surface Crack.

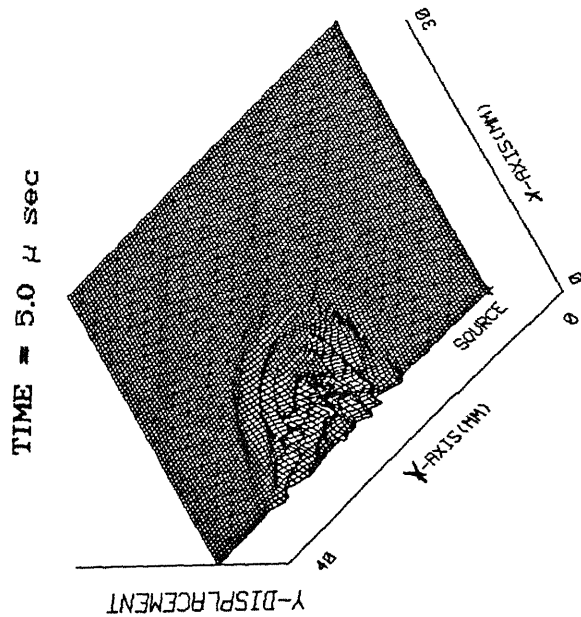
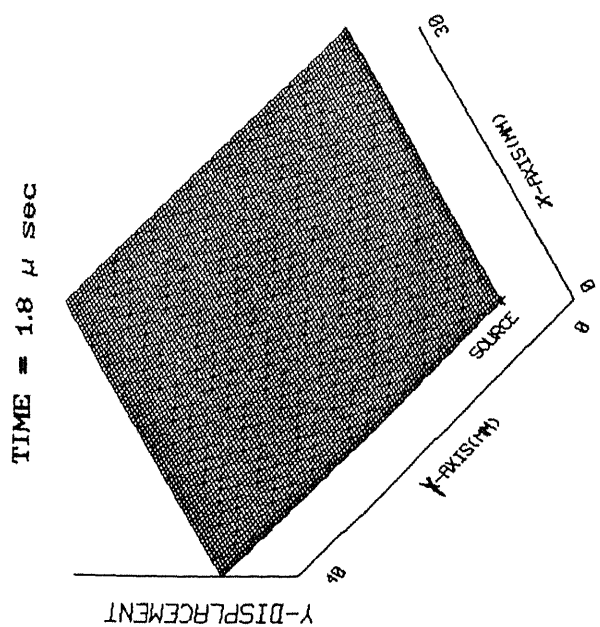
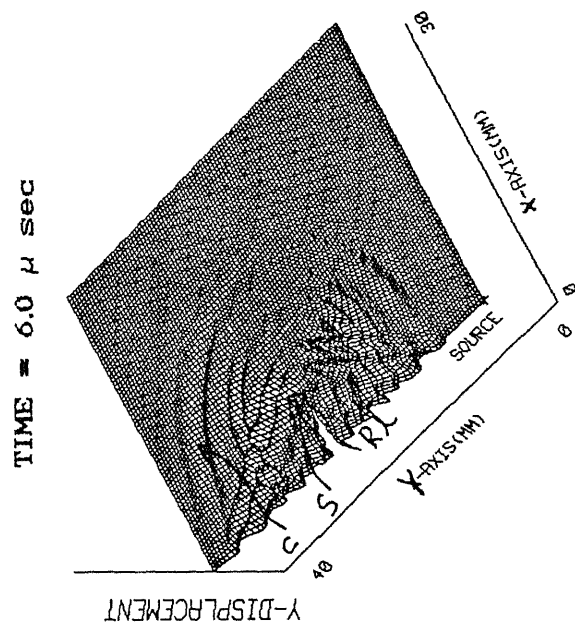
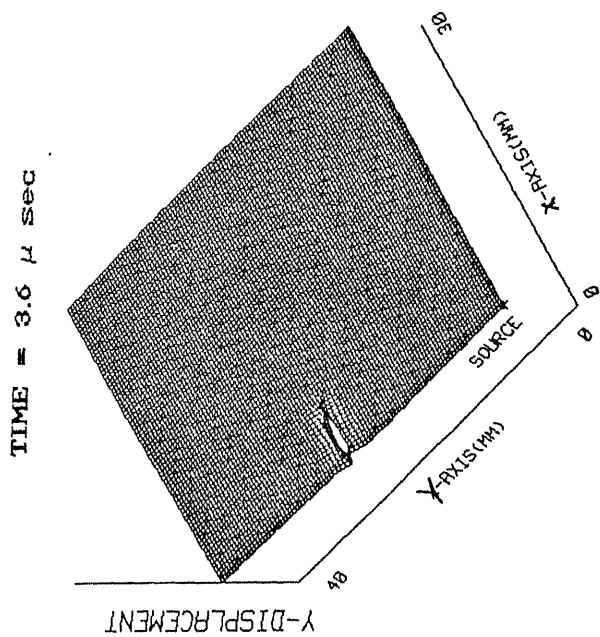


Fig. 4.14 Scattered Y-Displacement Field: Compression Wave Interaction with A Surface Crack.

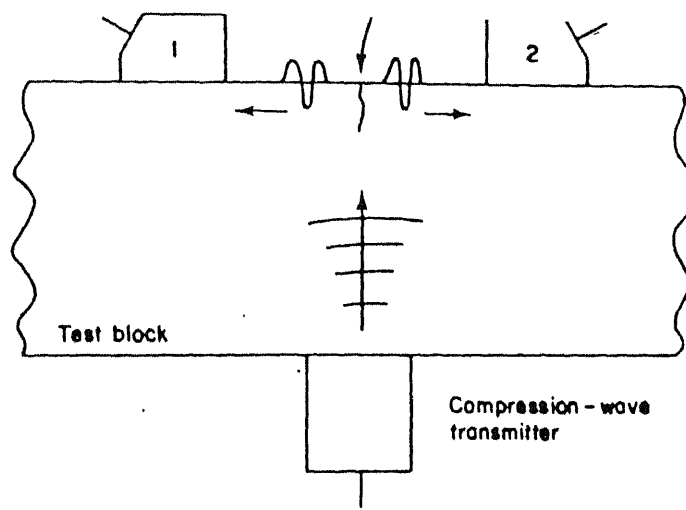


Fig. 4.16 The Basic Compression to Rayleigh Wave Mode Conversion Configuration.[26]

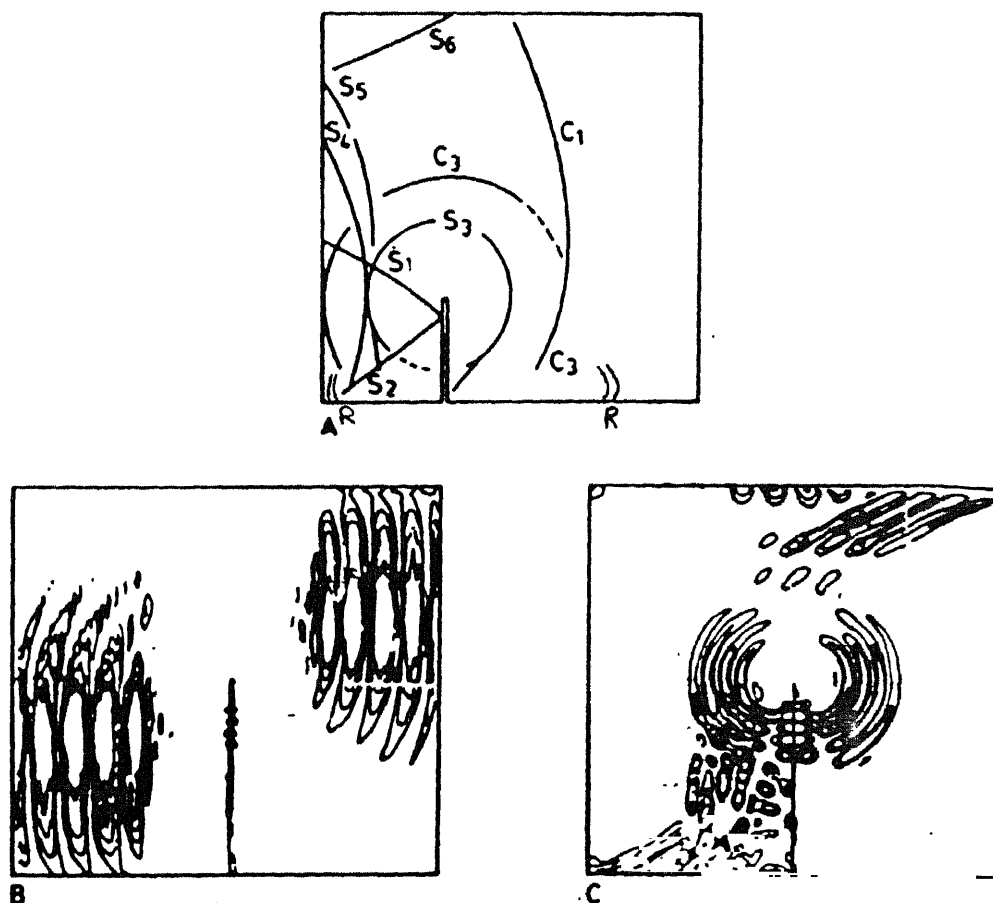


Fig. 4.15 (a) Interpretation of Photoelastic Visualisation of the Field After A Plane Compression Wave has Scattered from a Slit. (b) Contours of Compression Wave to correspond with (a). (c) Contours of Shear Wave to correspond with (a).

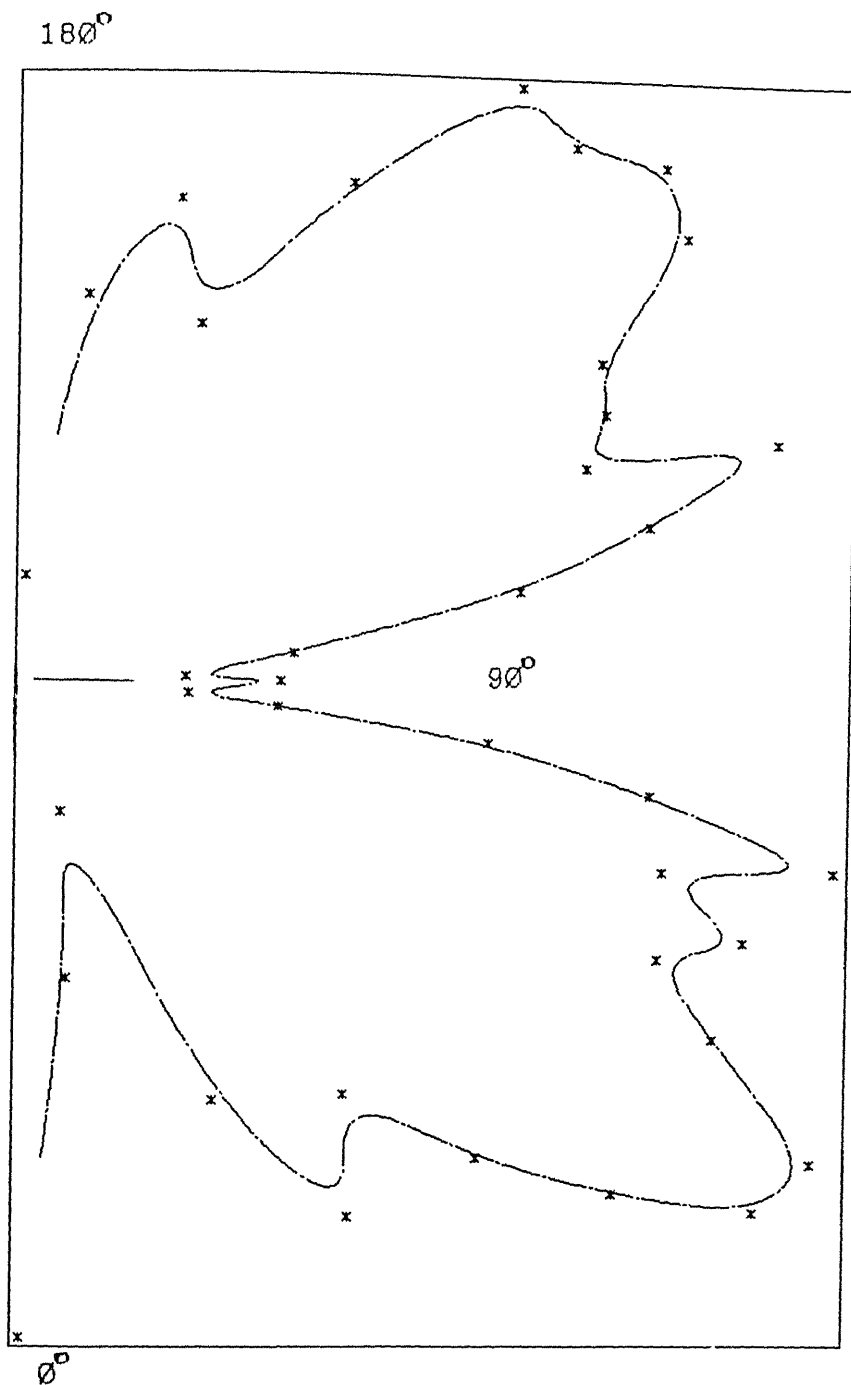


Fig. 4.17 Polar Plot of Scattered Amplitudes by A Compression Wave Interaction with A Surface Crack.

TOTAL NO. OF NODES = 1230

TOTAL NO. OF ELEMENTS = 1152

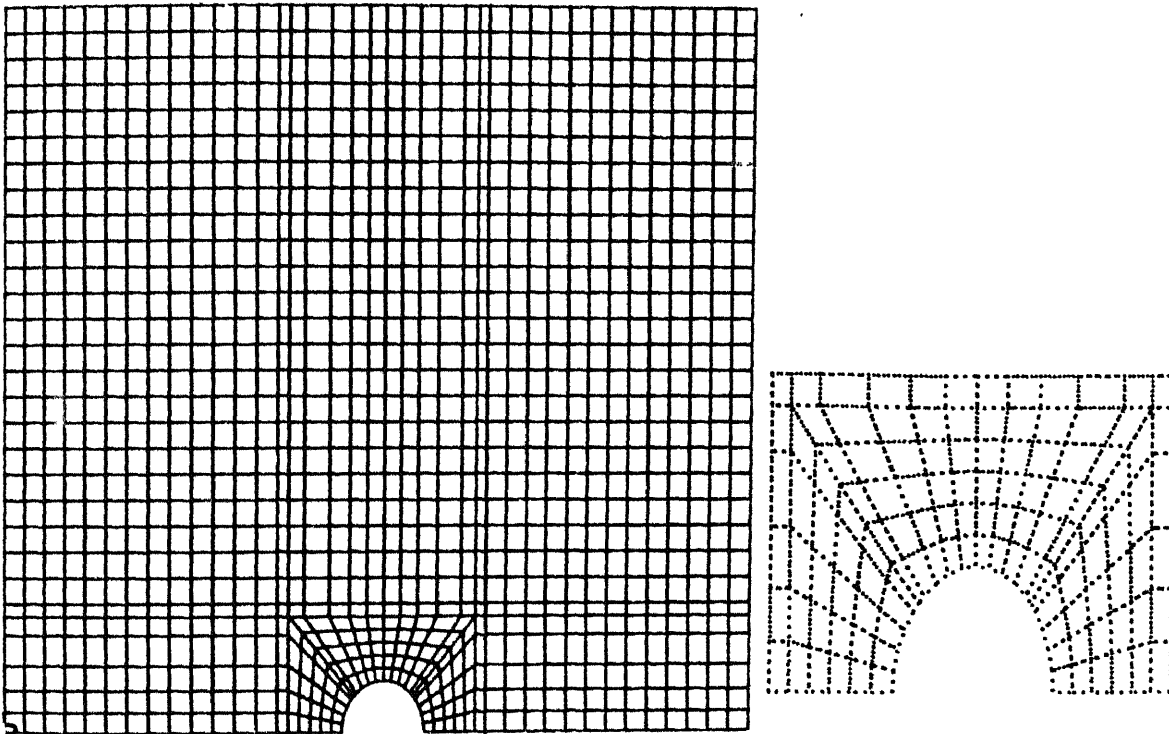
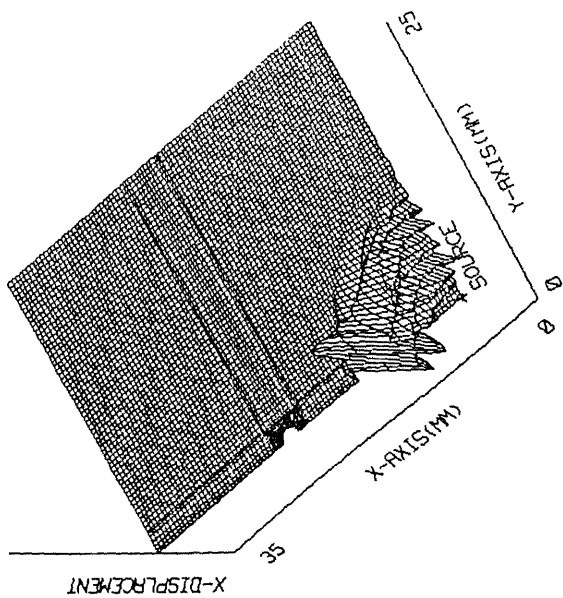


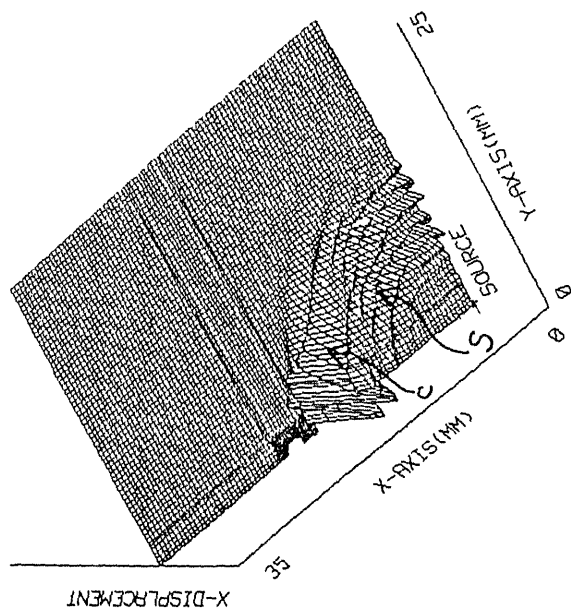
Fig. 4.18 Finite Element Discretization of a Plate with Hole.



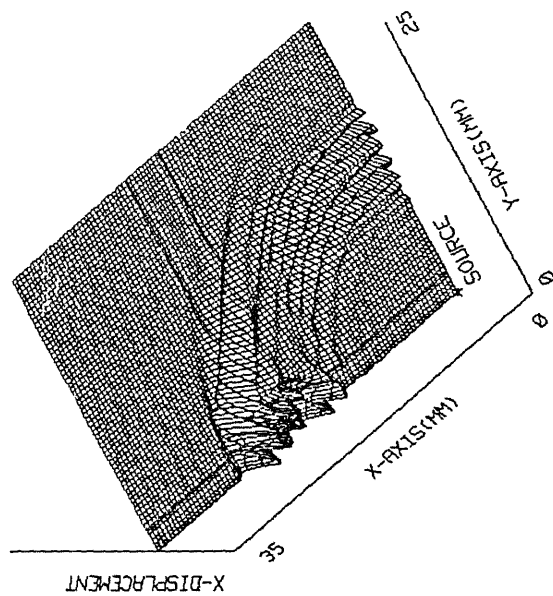
TIME = 1.8  $\mu$  sec



TIME = 2.8  $\mu$  sec



TIME = 3.8  $\mu$  sec



TIME = 5.0  $\mu$  sec

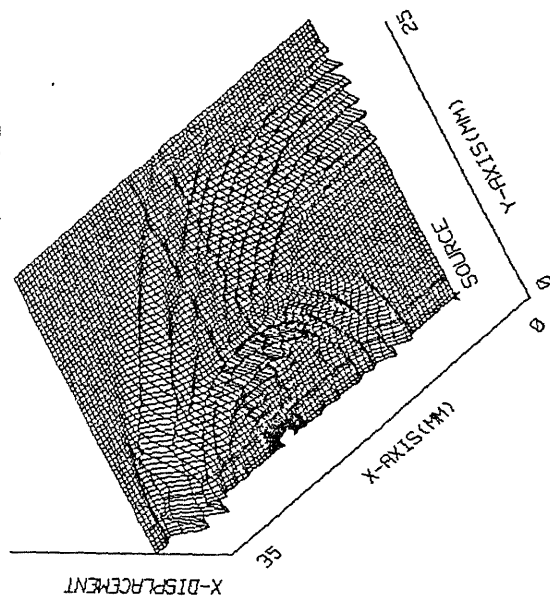
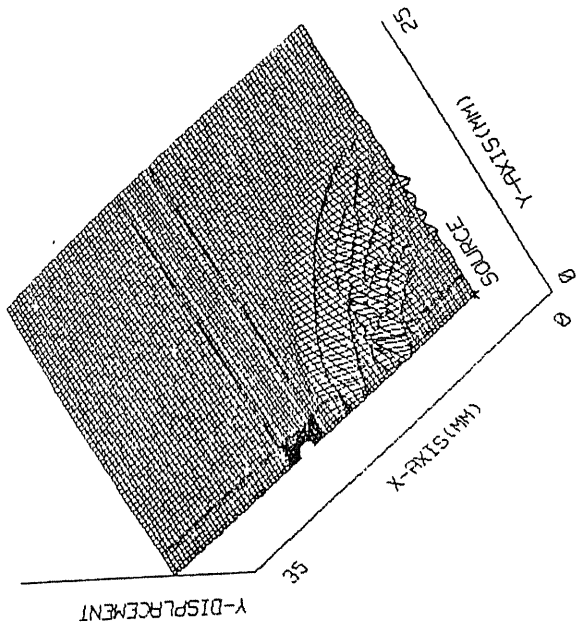
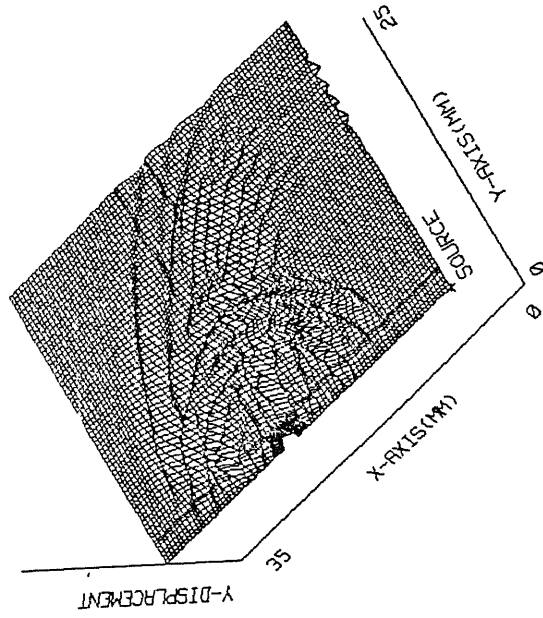


Fig. 4.19 X-Displacement Field: Compression Wave Interaction with Hole in Isotropic solid.

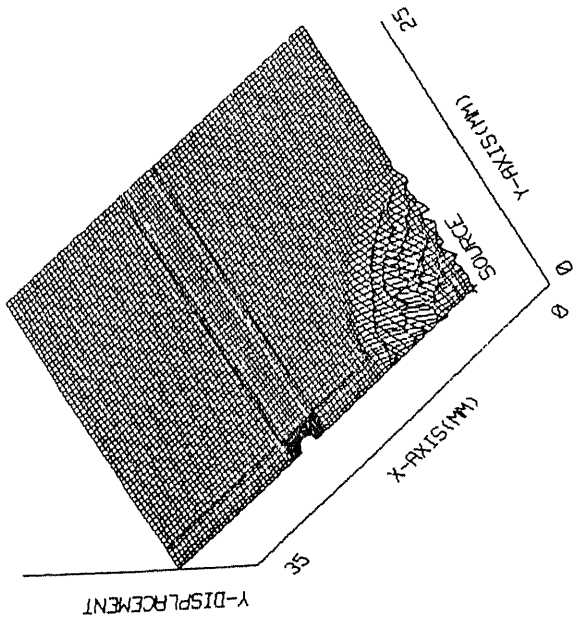
TIME = 2.8  $\mu$  sec



TIME = 5.0  $\mu$  sec



TIME = 1.8  $\mu$  sec



TIME = 3.8  $\mu$  sec

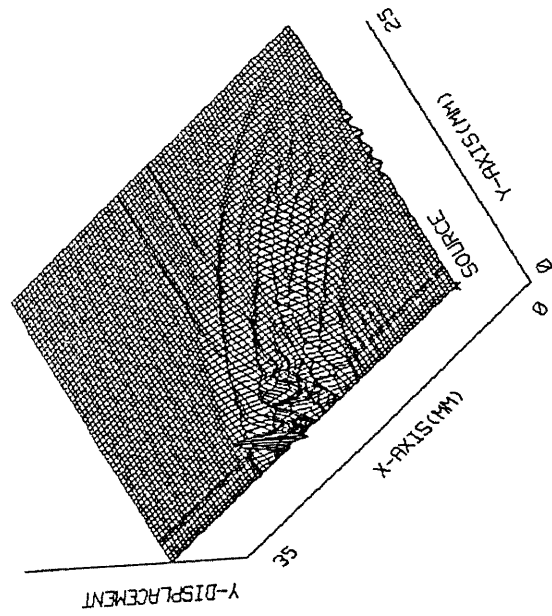


Fig. 4.20 Y-Displacement Field: Compression Wave Interaction with Hole in Isotropic solid.

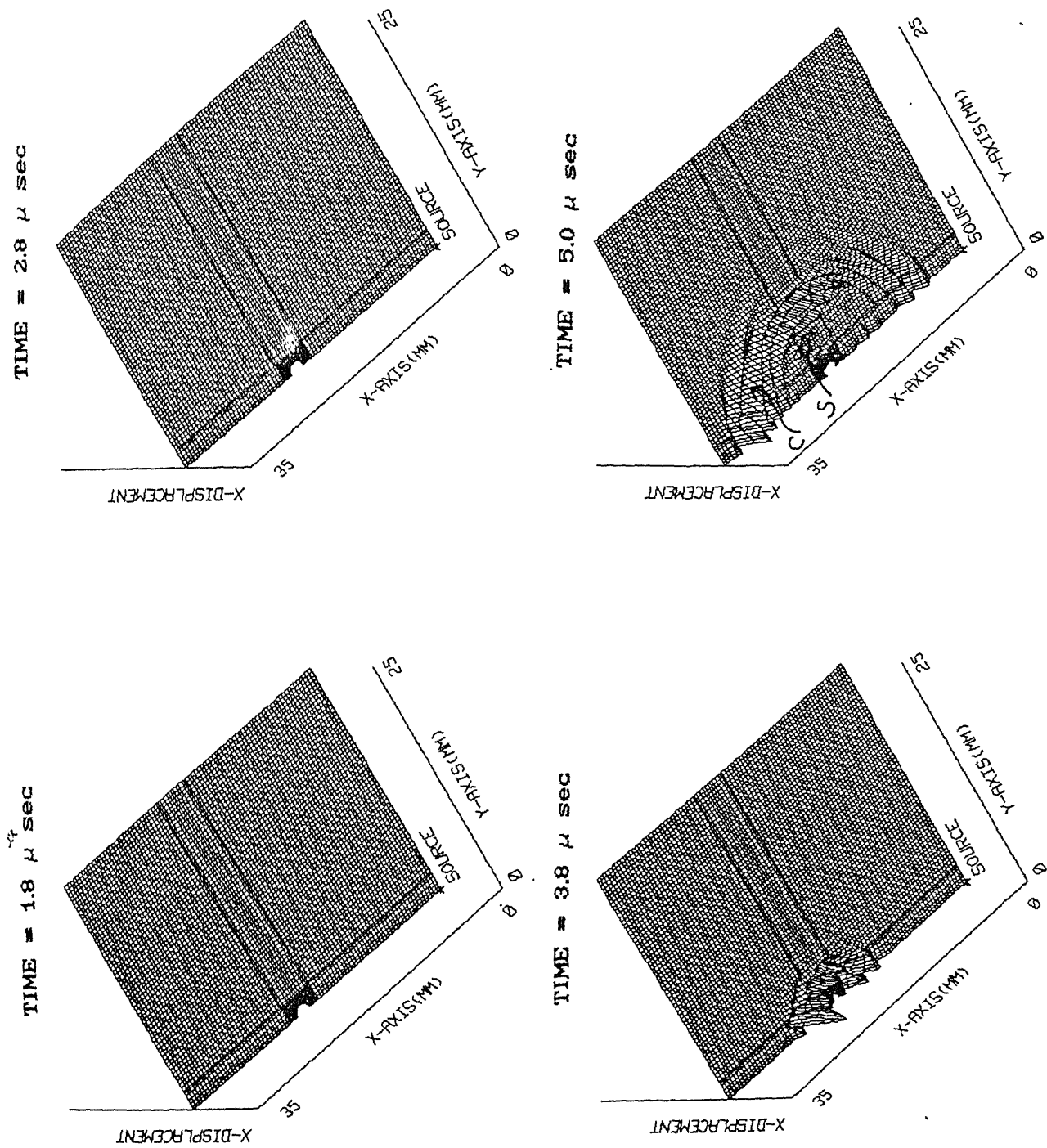


Fig. 4.21 Snapshots of the Scattered X- Disp. Field : Compression Wave Interaction with Hole in Isotropic Solid.

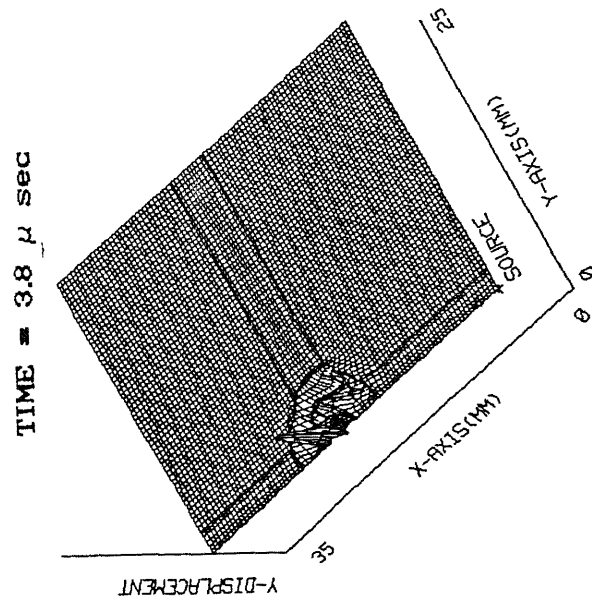
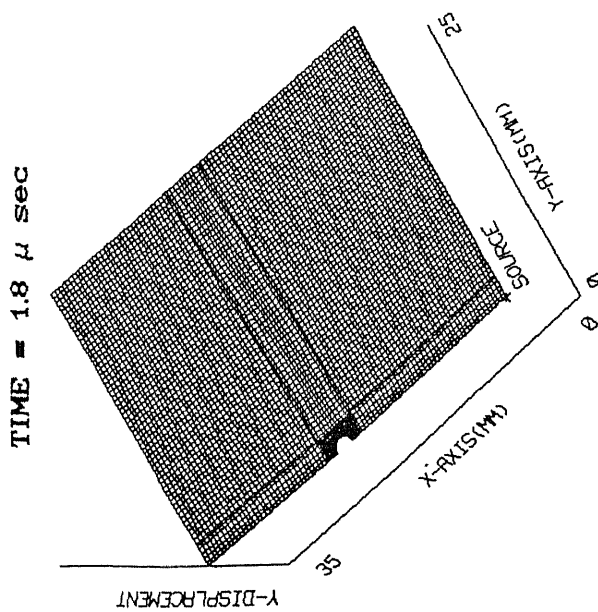
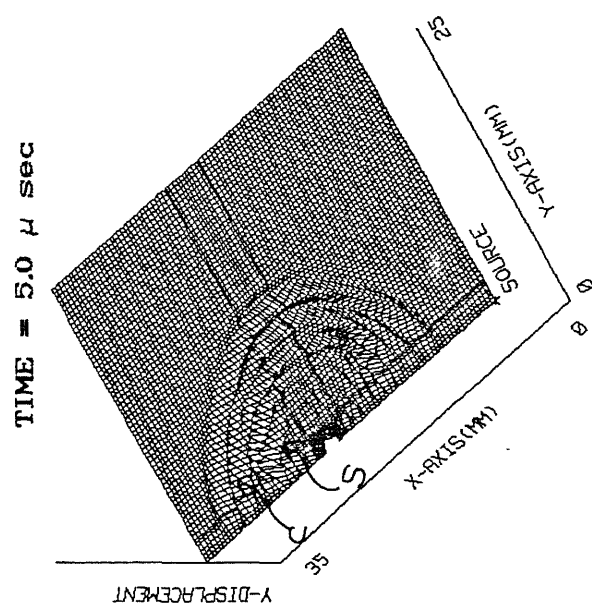
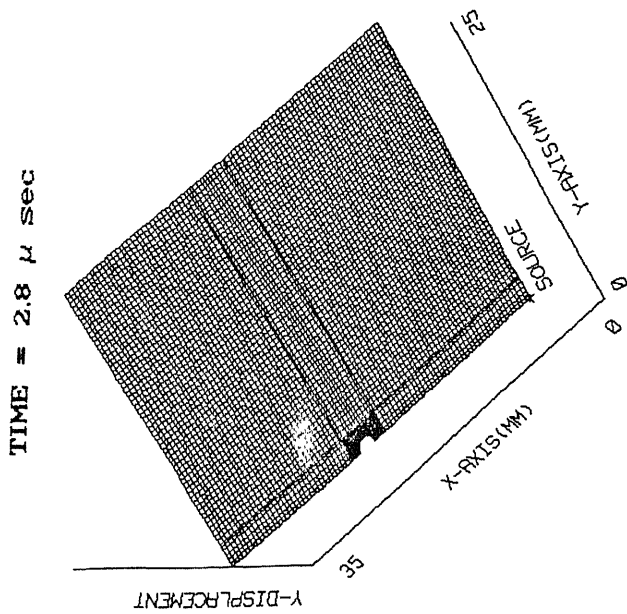


Fig. 4.22 Snapshots of the Scattered Y- Disp. Field : Compression  
Wave Interaction with Hole in Isotropic Solid.

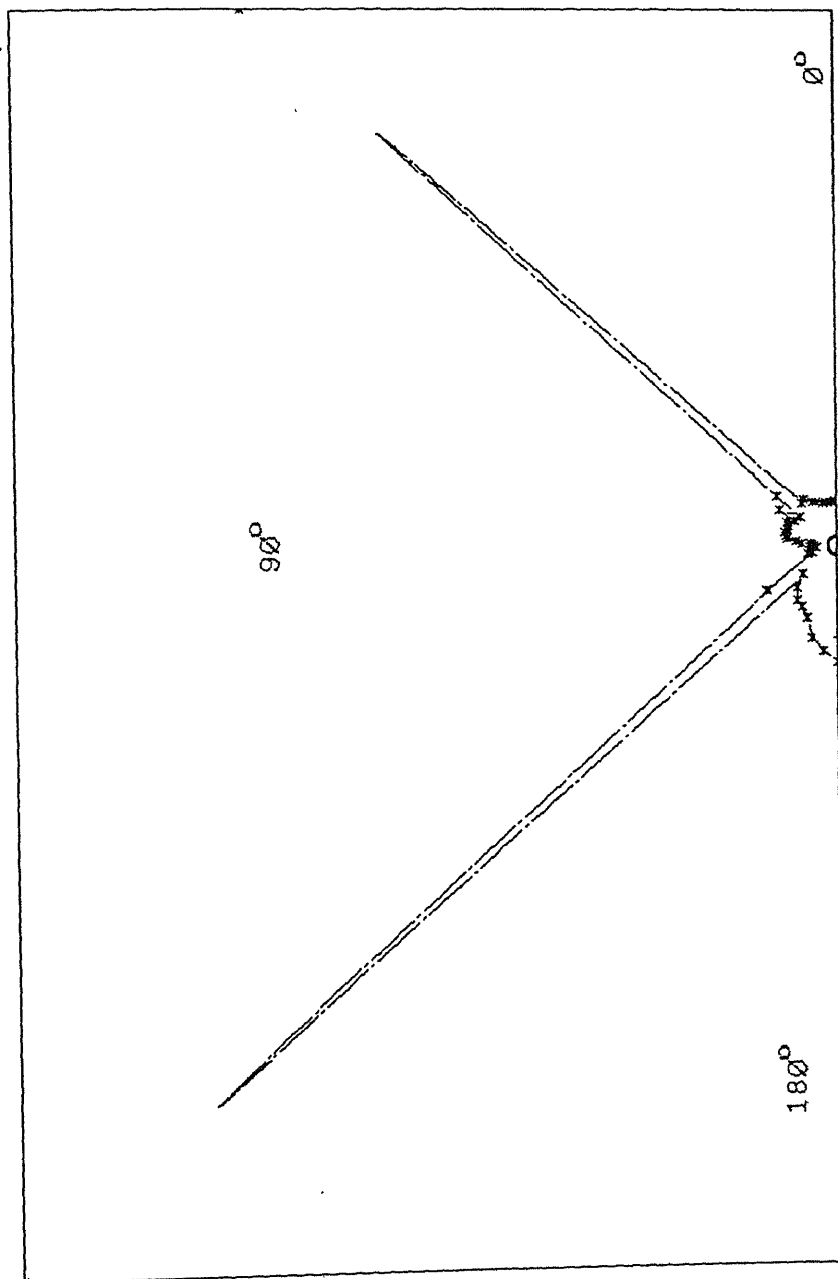


Fig 4.23 Polar Plot of Scattered Amplitudes by A Compression wave Interaction with A Hole.

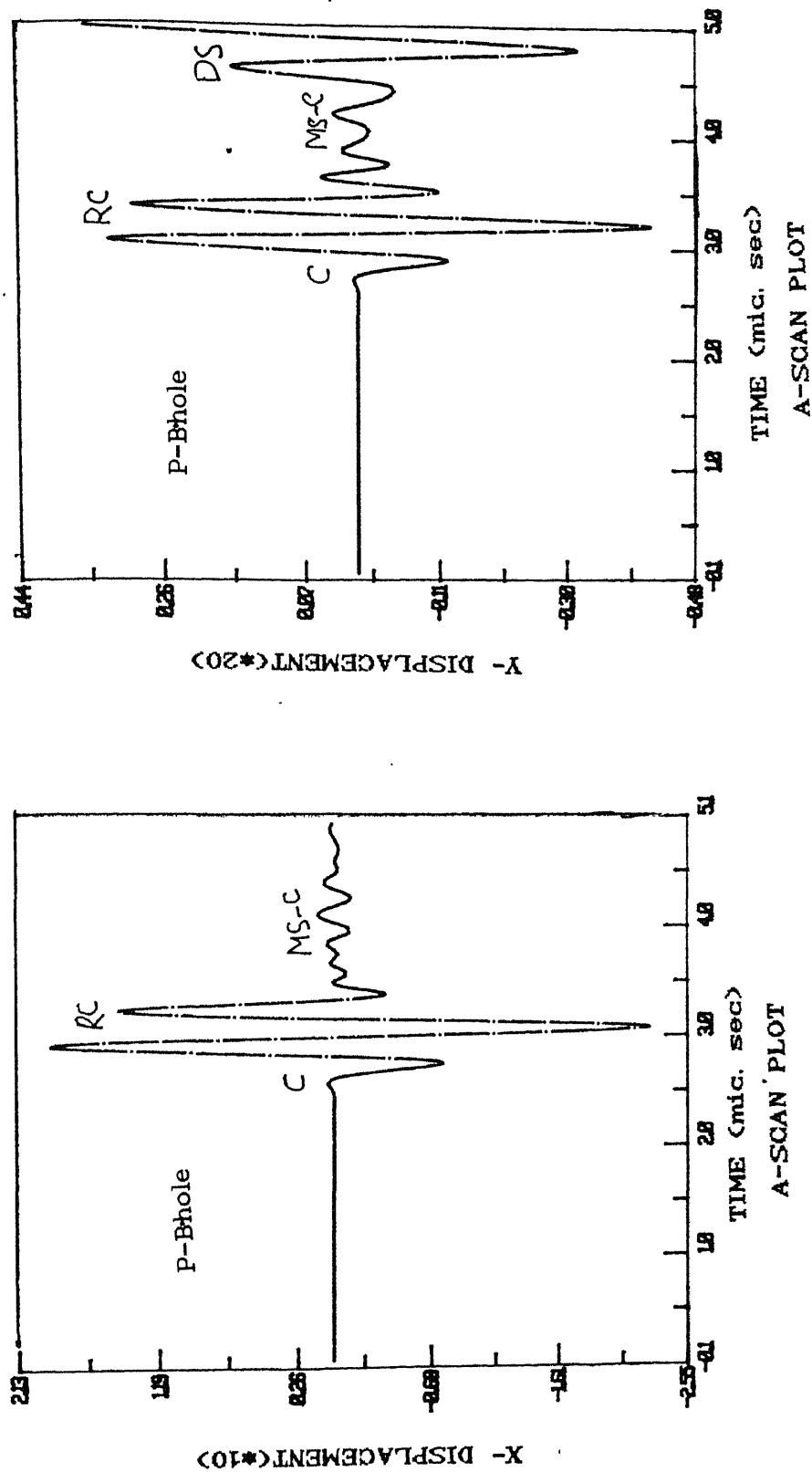
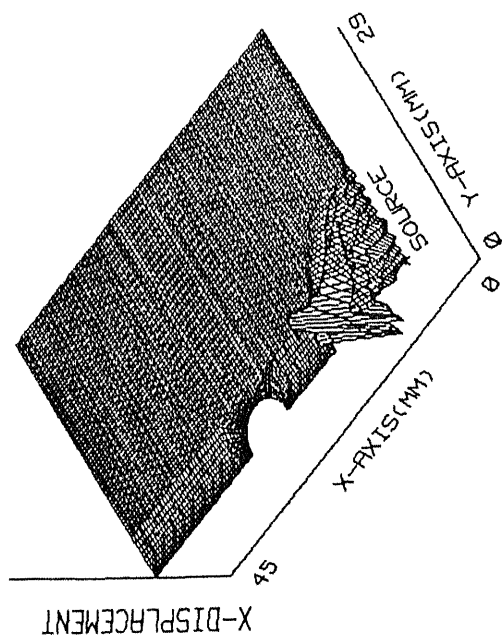
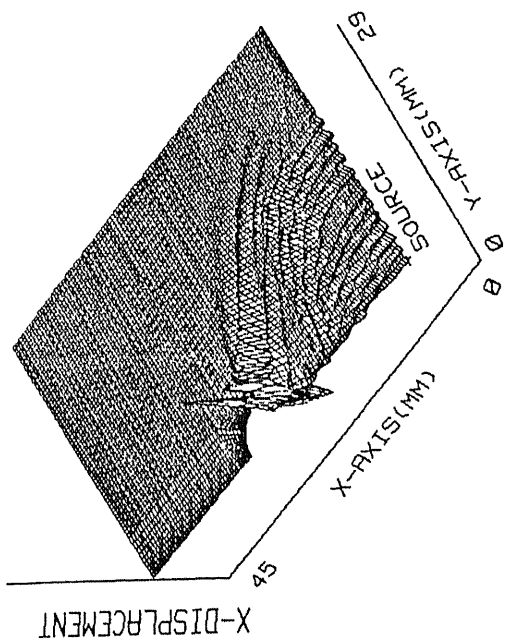


Fig. 4.24 A-SCAN plot at a point before the hole surface  
(Compression wave interaction)

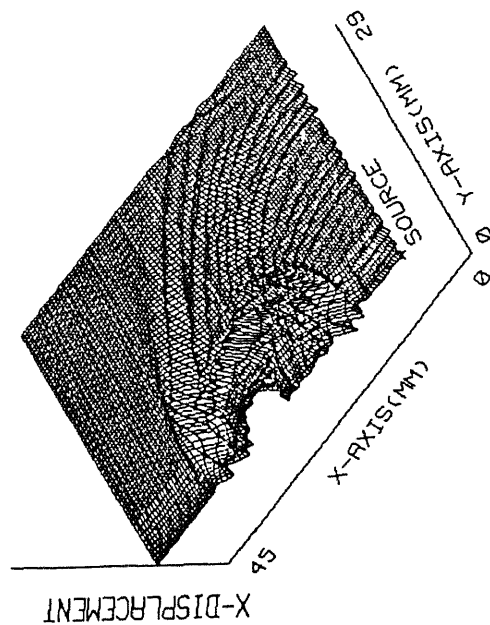
TIME = 2.0 mic.sec



TIME = 3.8 mic.sec



TIME = 5.4 mic.sec



TIME = 6.4 mic.sec

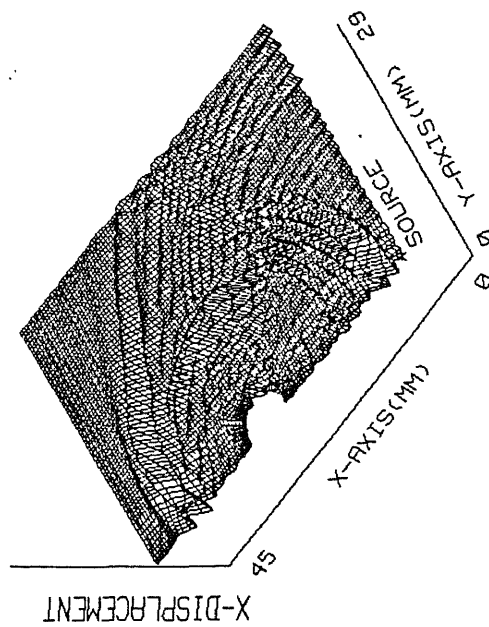
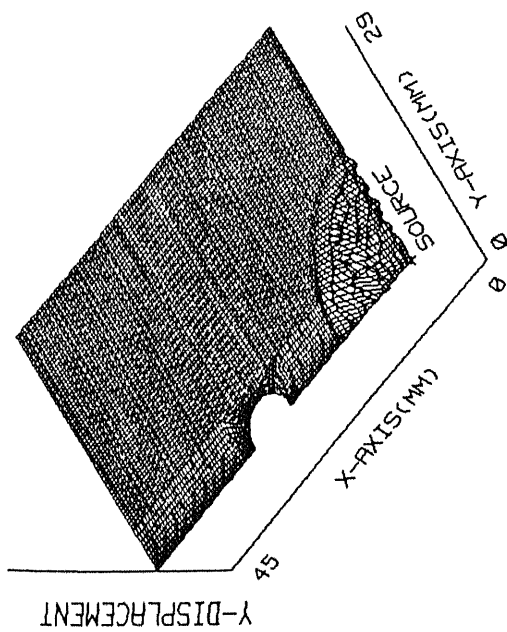
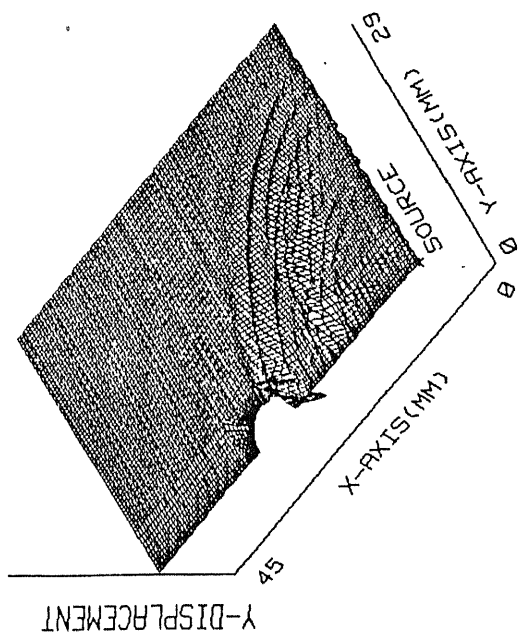


Fig. 4.25 X-Displacement Field: Compression Wave Interaction with Hole in Isotropic solid. (Resonance Condition)

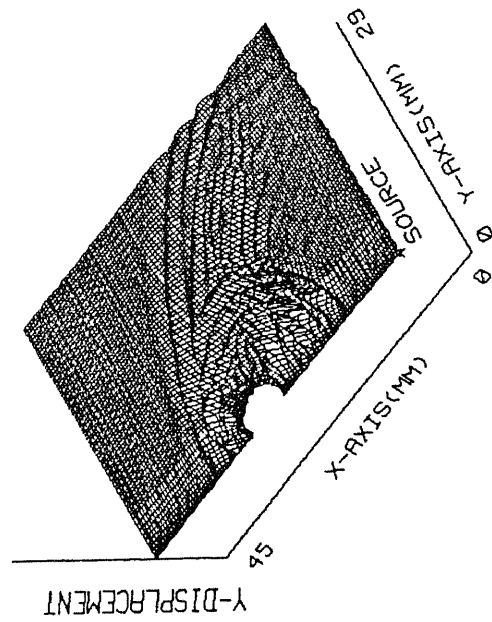
TIME = 2.0 mic.sec



TIME = 3.8 mic.sec



TIME = 5.4 mic.sec



TIME = 6.4 mic.sec

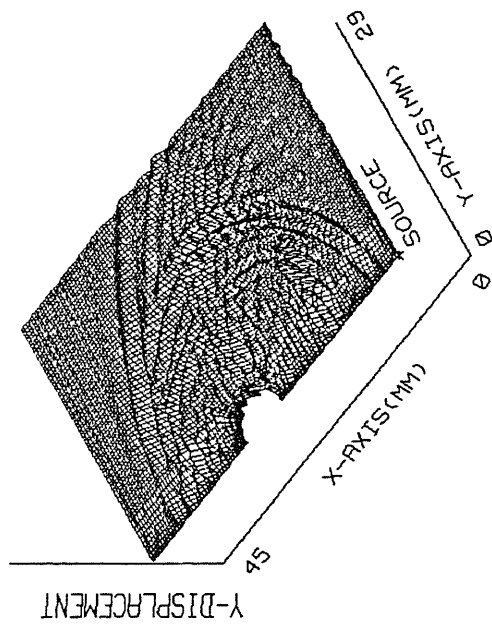
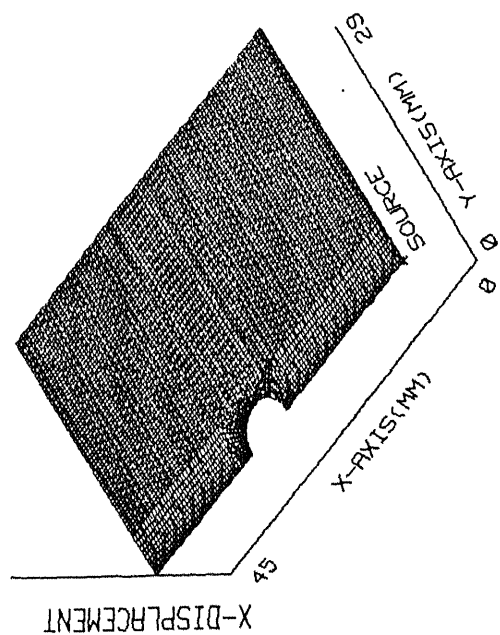


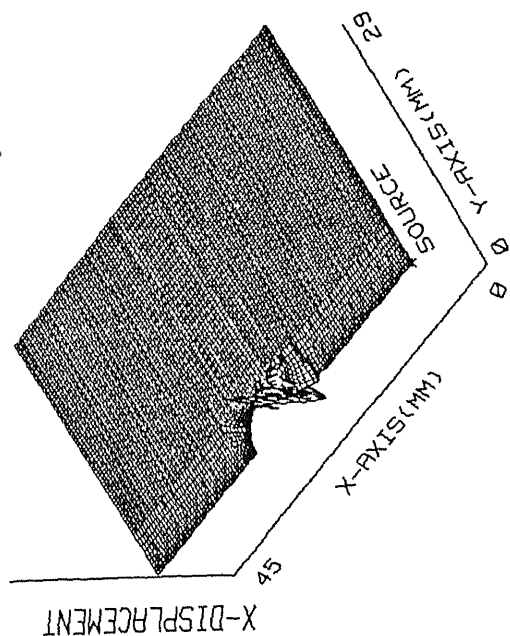
Fig. 4.26 Y-Displacement Field: Compression Wave Interaction with Hole in Isotropic solid.(Resonance Condition)



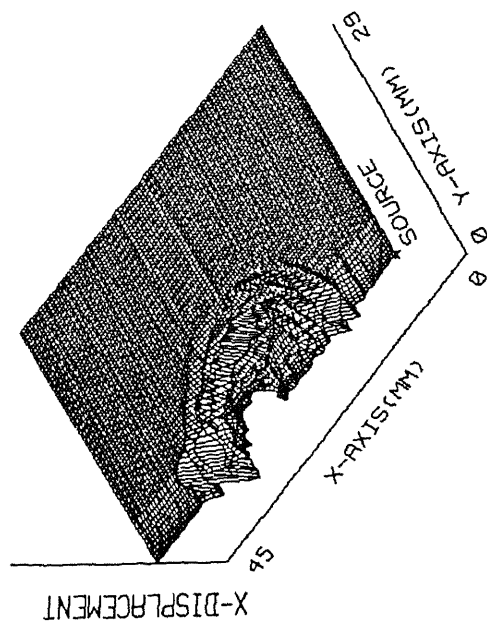
TIME = 2.0 mic.sec



TIME = 3.8 mic.sec



TIME = 5.4 mic.sec



TIME = 6.4 mic.sec

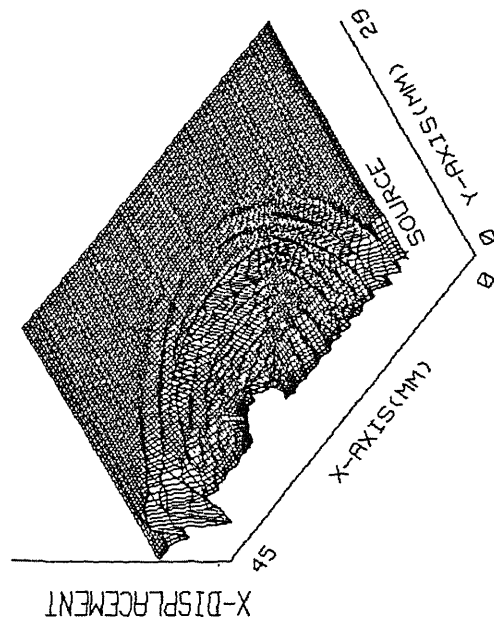
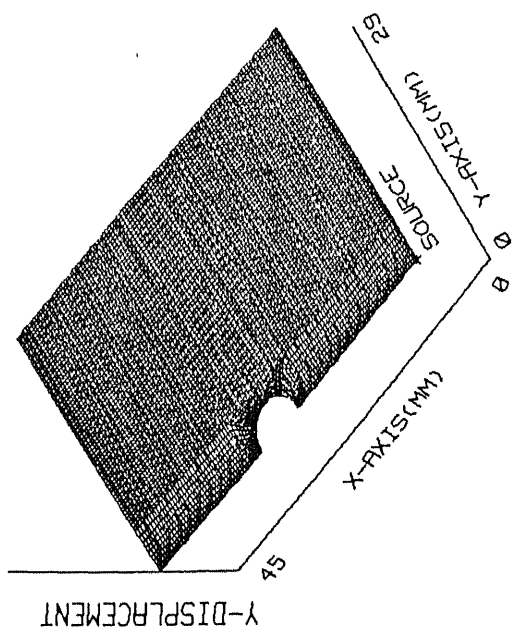
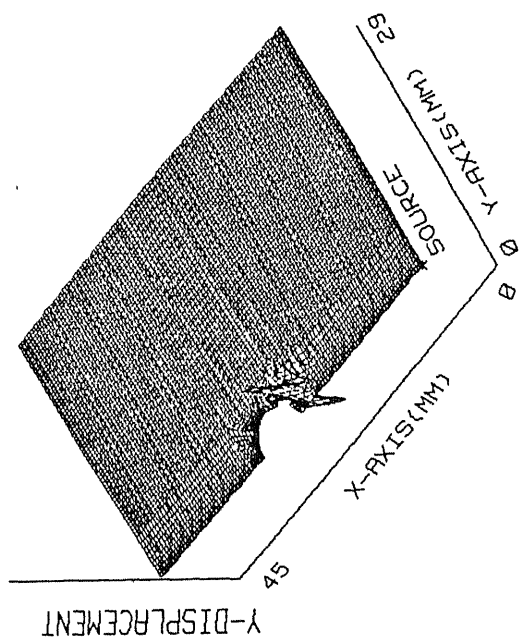


Fig. 4.27 Snapshots of the Scattered X-Disp. Field : Compression  
Wave Interaction with Hole in Isotropic Solid.  
(Resonance Condition)

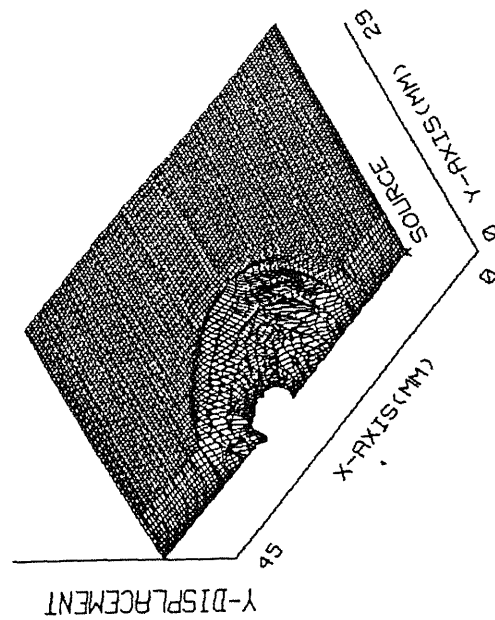
TIME = 2.0 mic.sec



TIME = 3.8 mic.sec



TIME = 5.4 mic.sec



TIME = 6.4 mic.sec

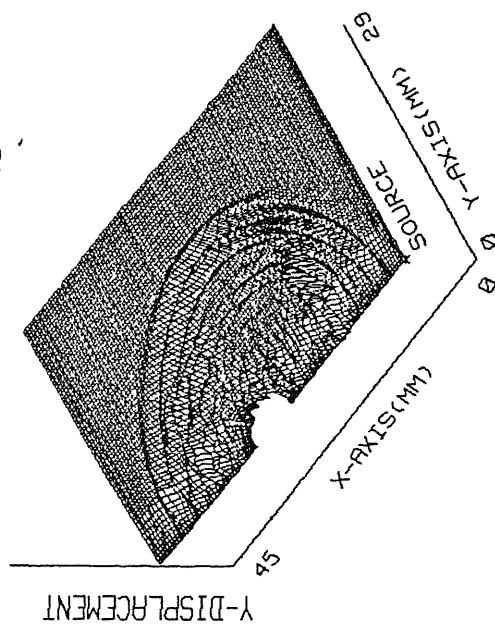


Fig. 4.28 Snapshots of the Scattered Y- Disp. Field : Compression  
Wave Interaction with Hole in Isotropic Solid.  
(Resonance Condition)

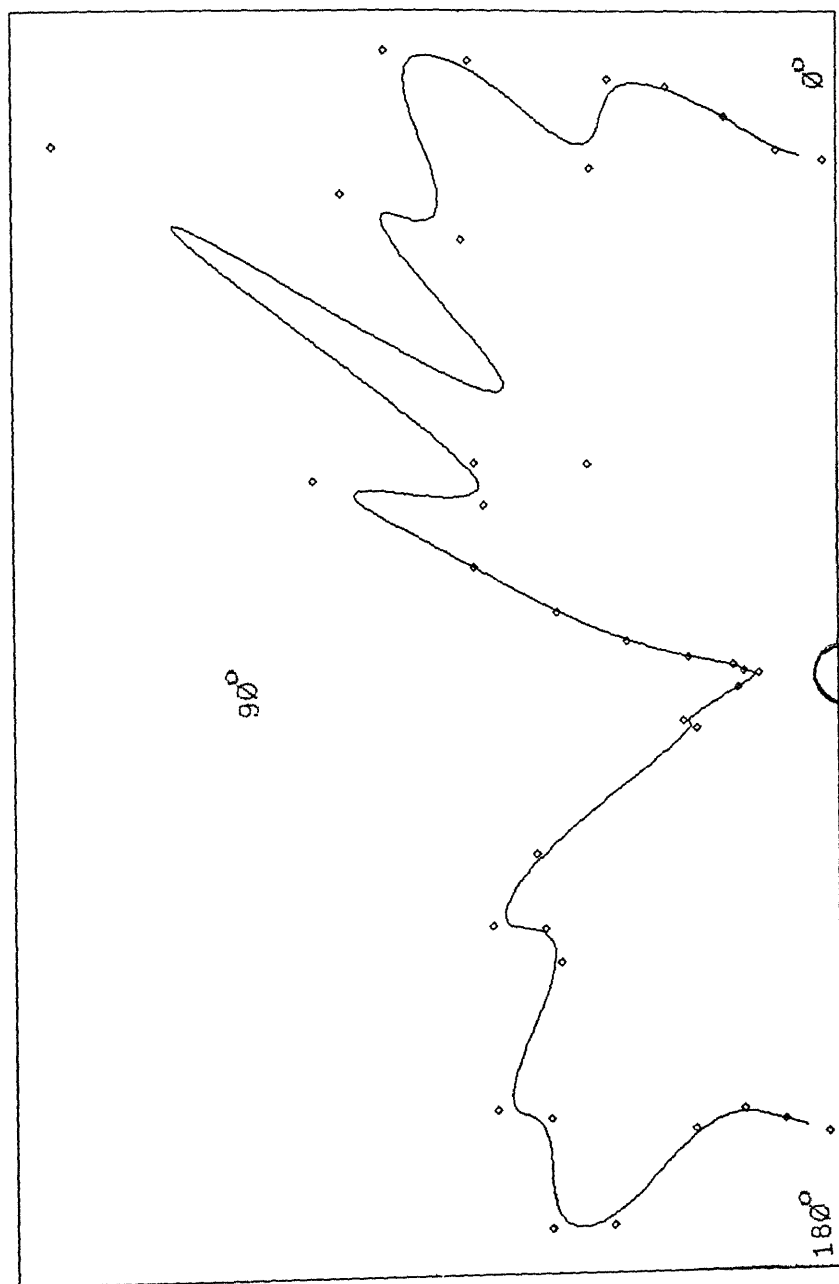


Fig 4.29 Polar Plot of Scattered Amplitudes by A Compression wave Interaction with A Hole. (Resonance Condition)

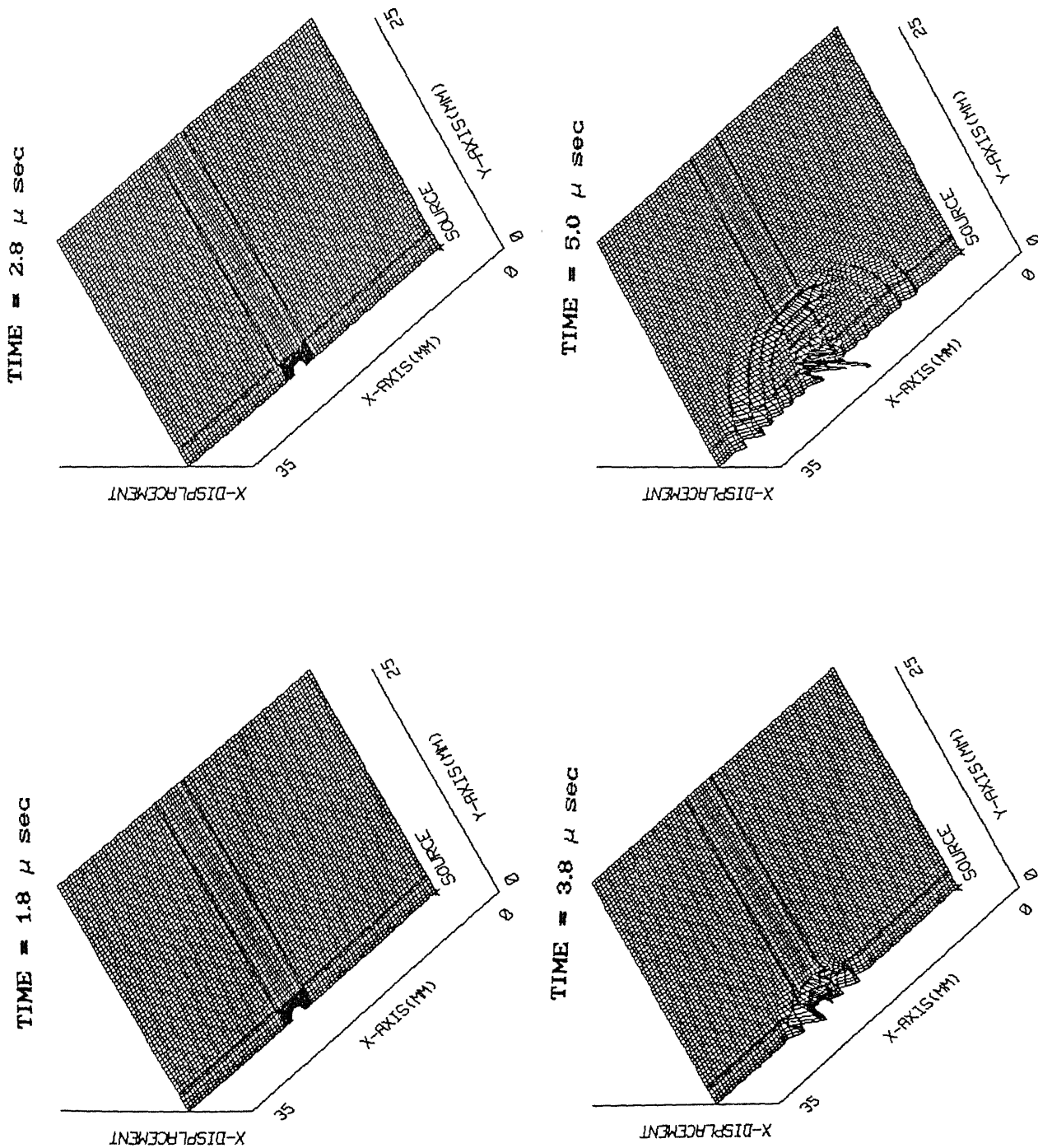


Fig. 4.30 Snapshots of the Scattered X- Disp. Field : Plane Shear Wave Interaction with Hole in Isotropic Solid.

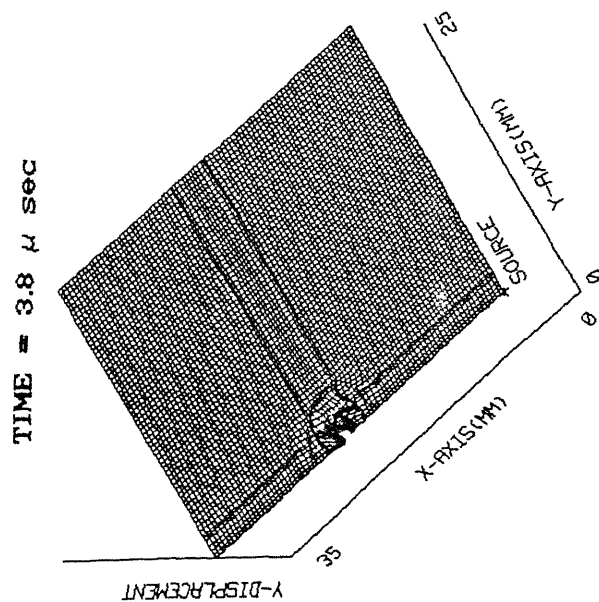
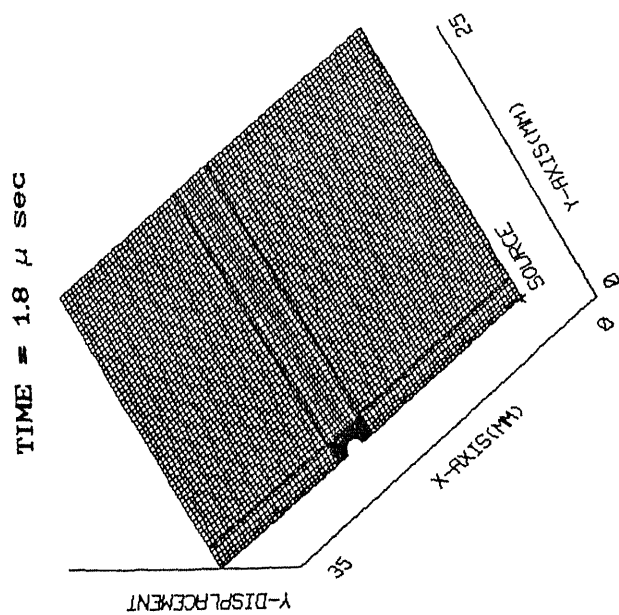
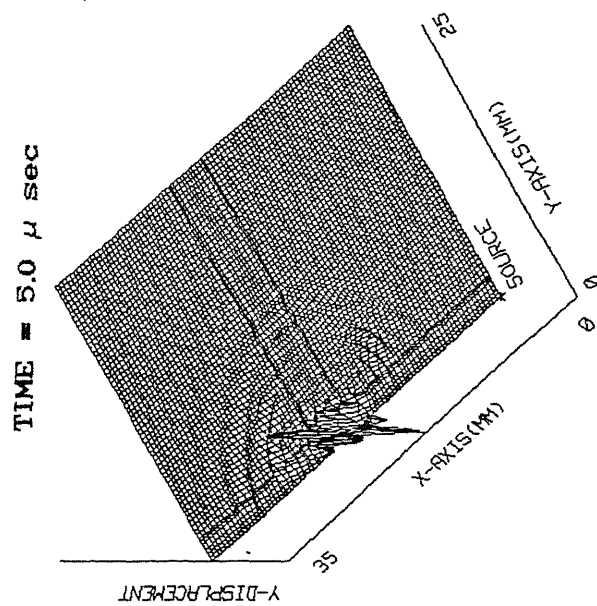
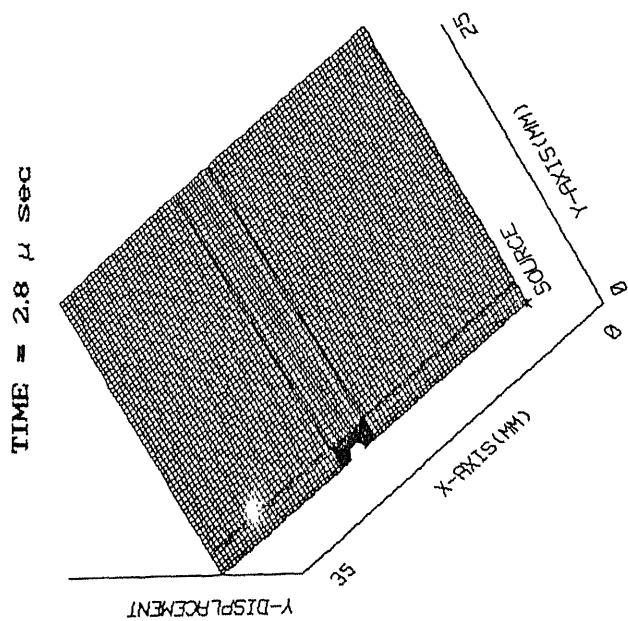


Fig. 4.31 Snapshots of the Scattered Y- Disp. Field : Plane Shear  
Wave Interaction with Hole in Isotropic Solid.

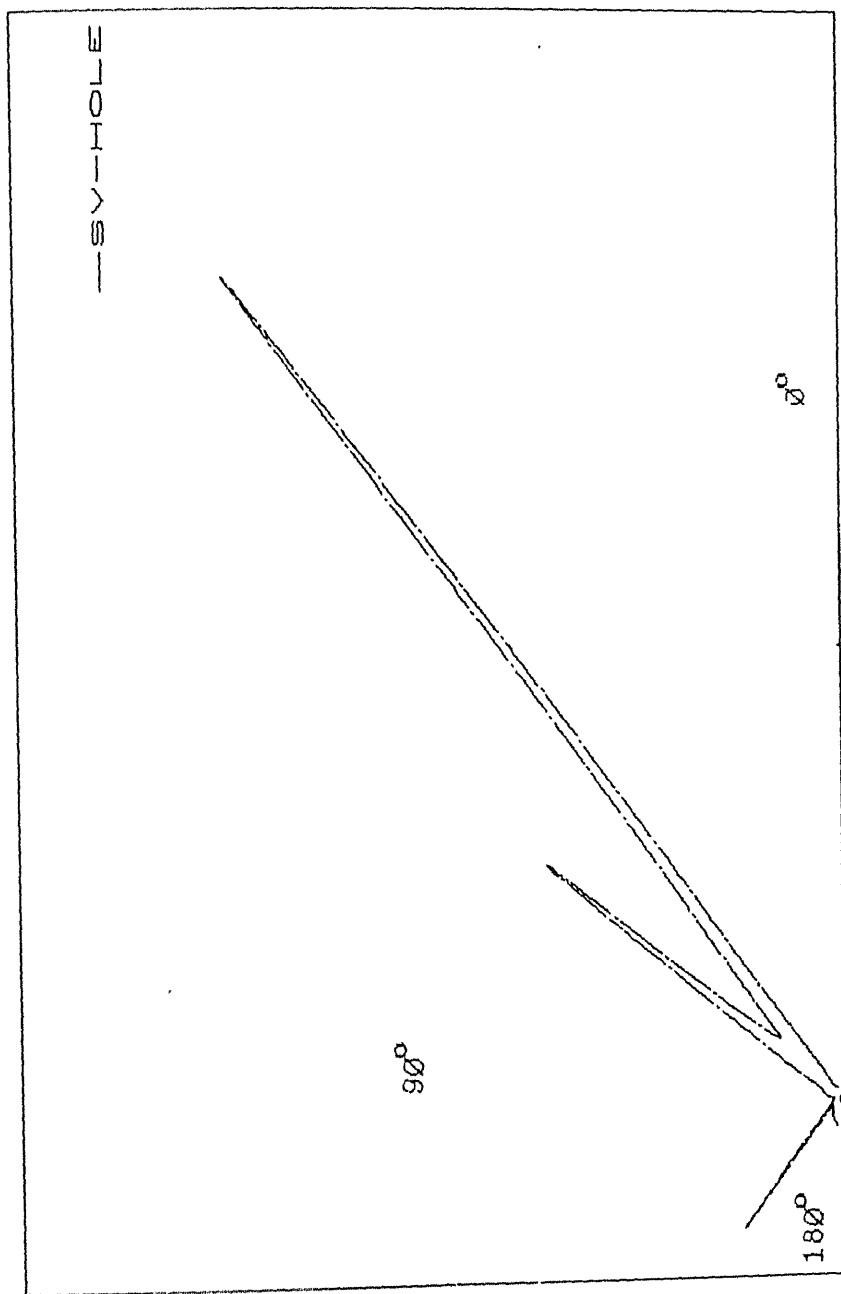


Fig. 4.32 Polar Plot of Scattered Amplitudes by A Shear wave Interaction with A Hole.

TOTAL NO. OF NODES = 1365

TOTAL NO. OF ELEMENTS = 1276

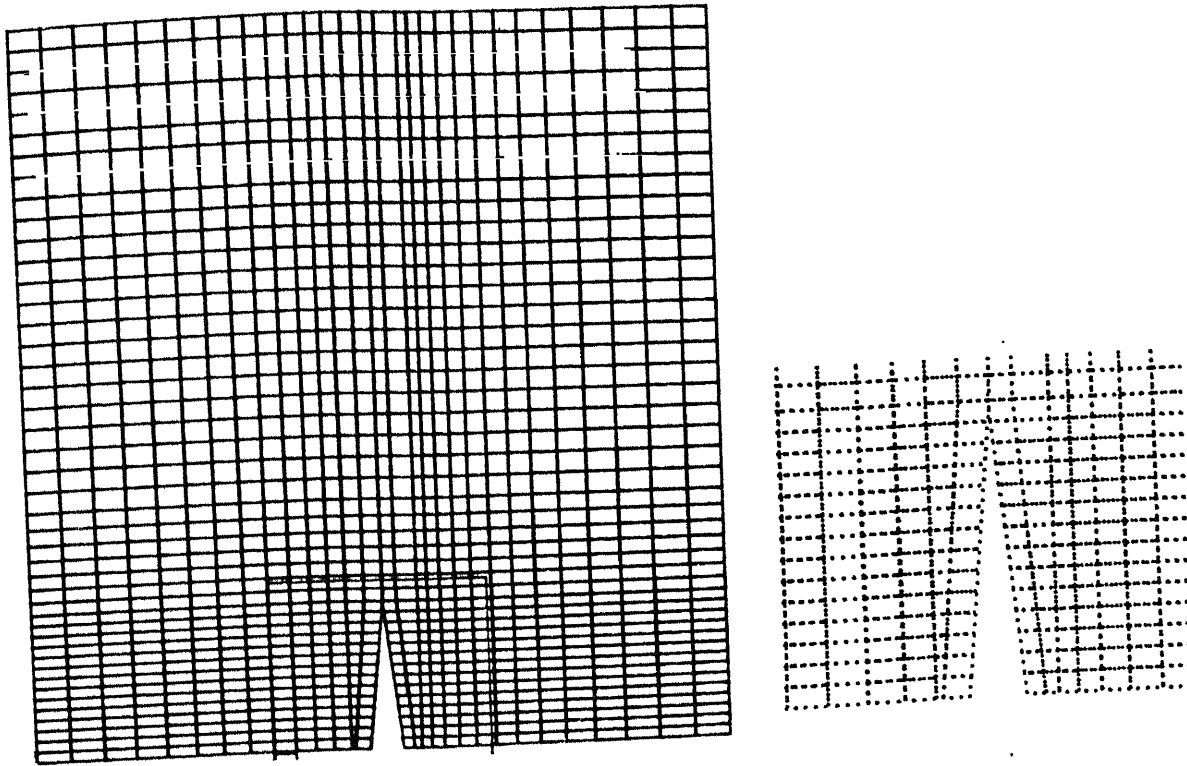
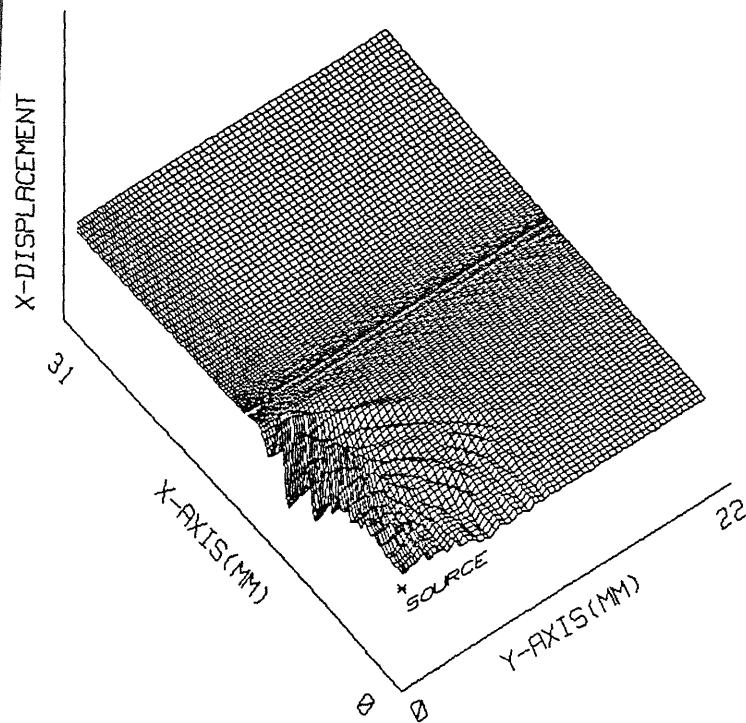
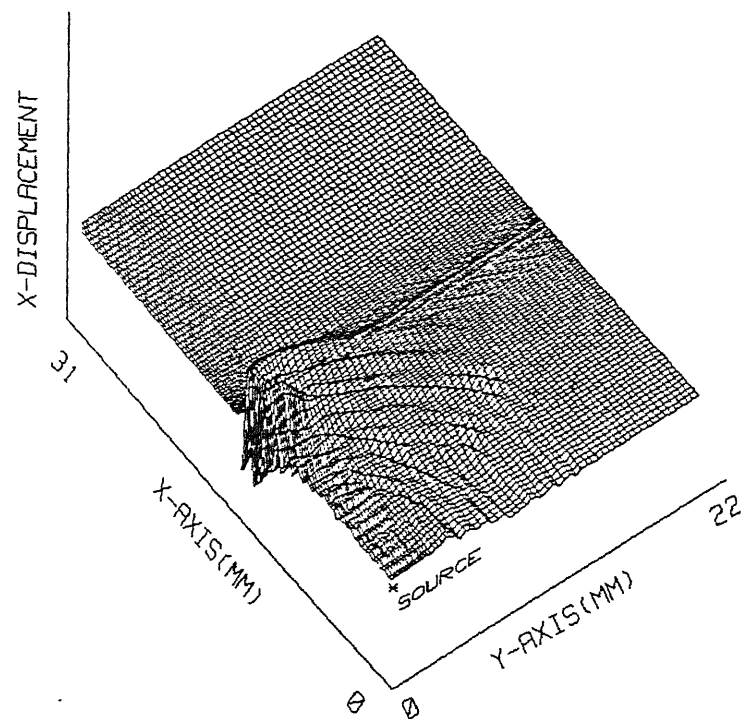


Fig. 4.33 Finite Element Discretization of A Wedge Crack  
(Body Defect).

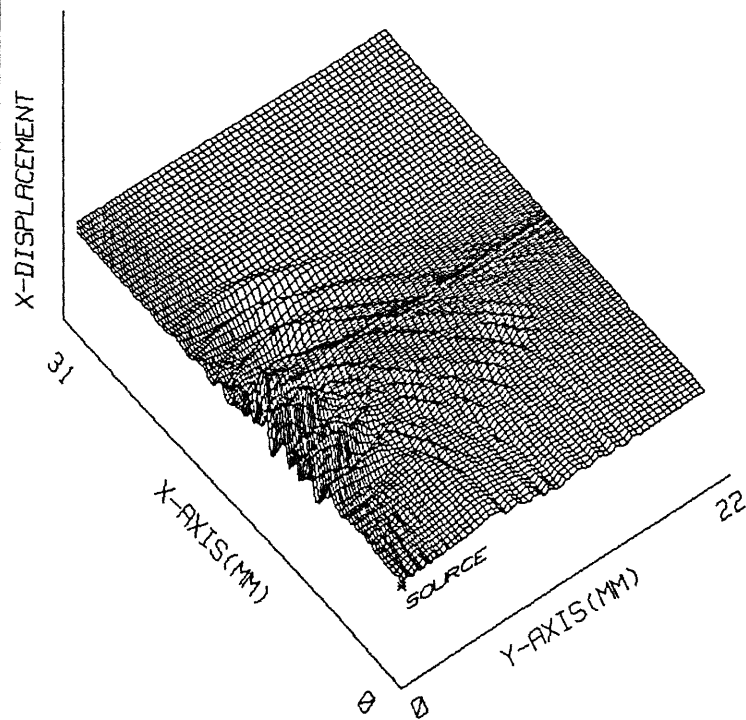
TIME = 2.2  $\mu$  sec



TIME = 3.0  $\mu$  sec



TIME = 3.8  $\mu$  sec



TIME = 4.8  $\mu$  sec

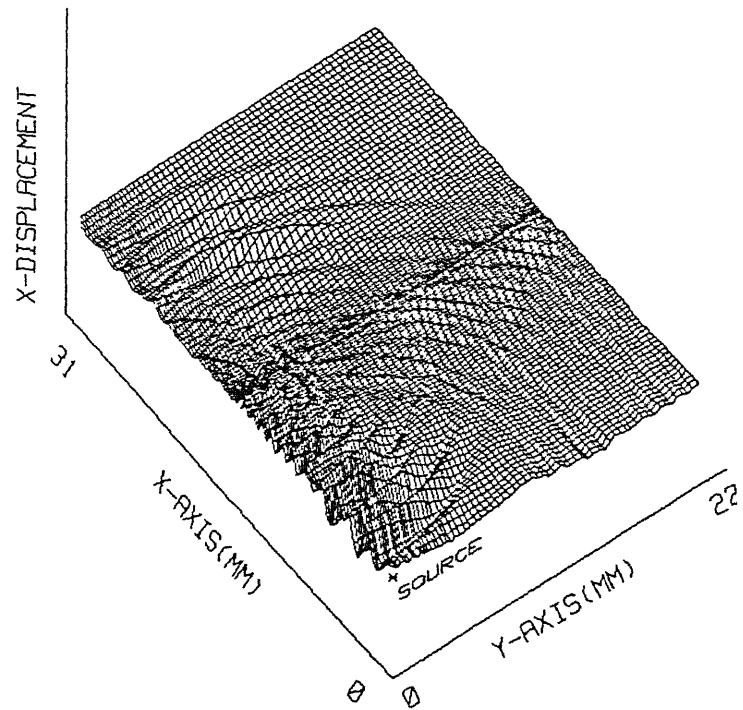
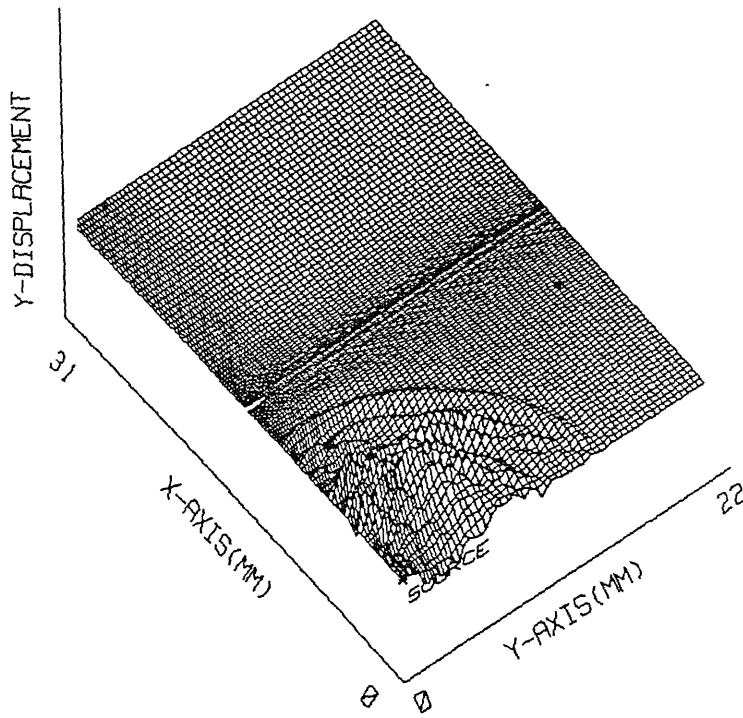


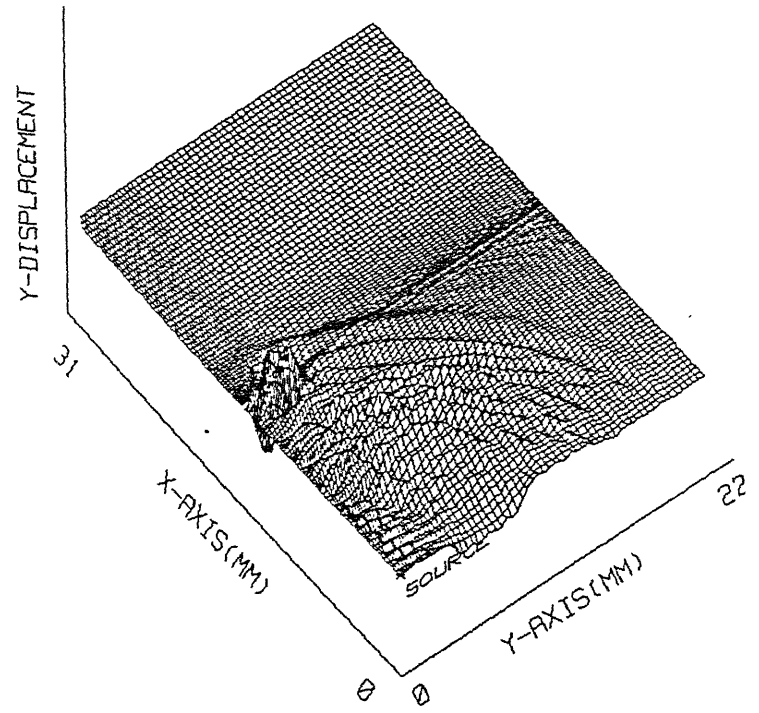
Fig. 4.34 X-Displacement Field: Compression Wave Interaction with Wedge Crack.



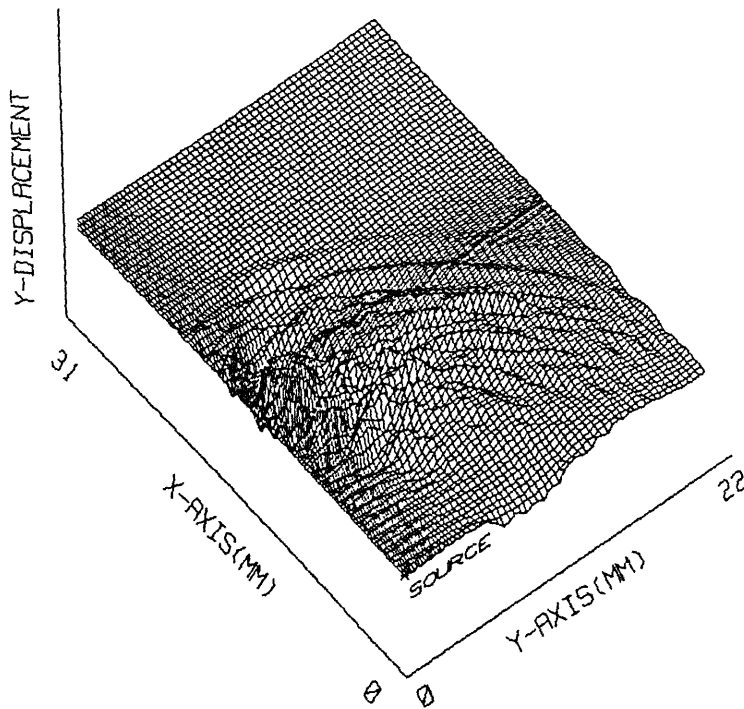
TIME = 2.2  $\mu$  sec



TIME = 3.0  $\mu$  sec



TIME = 3.8  $\mu$  sec



TIME = 4.8  $\mu$  sec

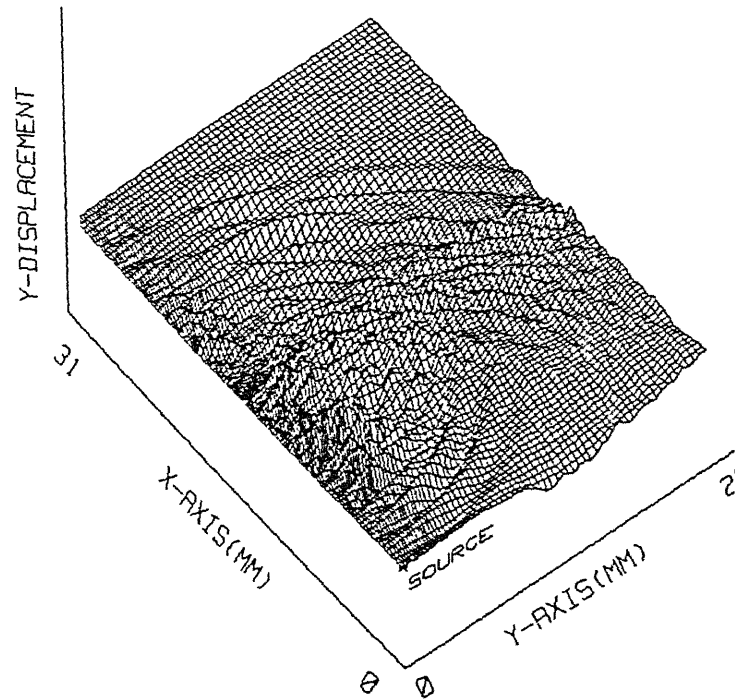


Fig. 4.35 Y-Displacement Field: Compression Wave Interaction with Wedge Crack.

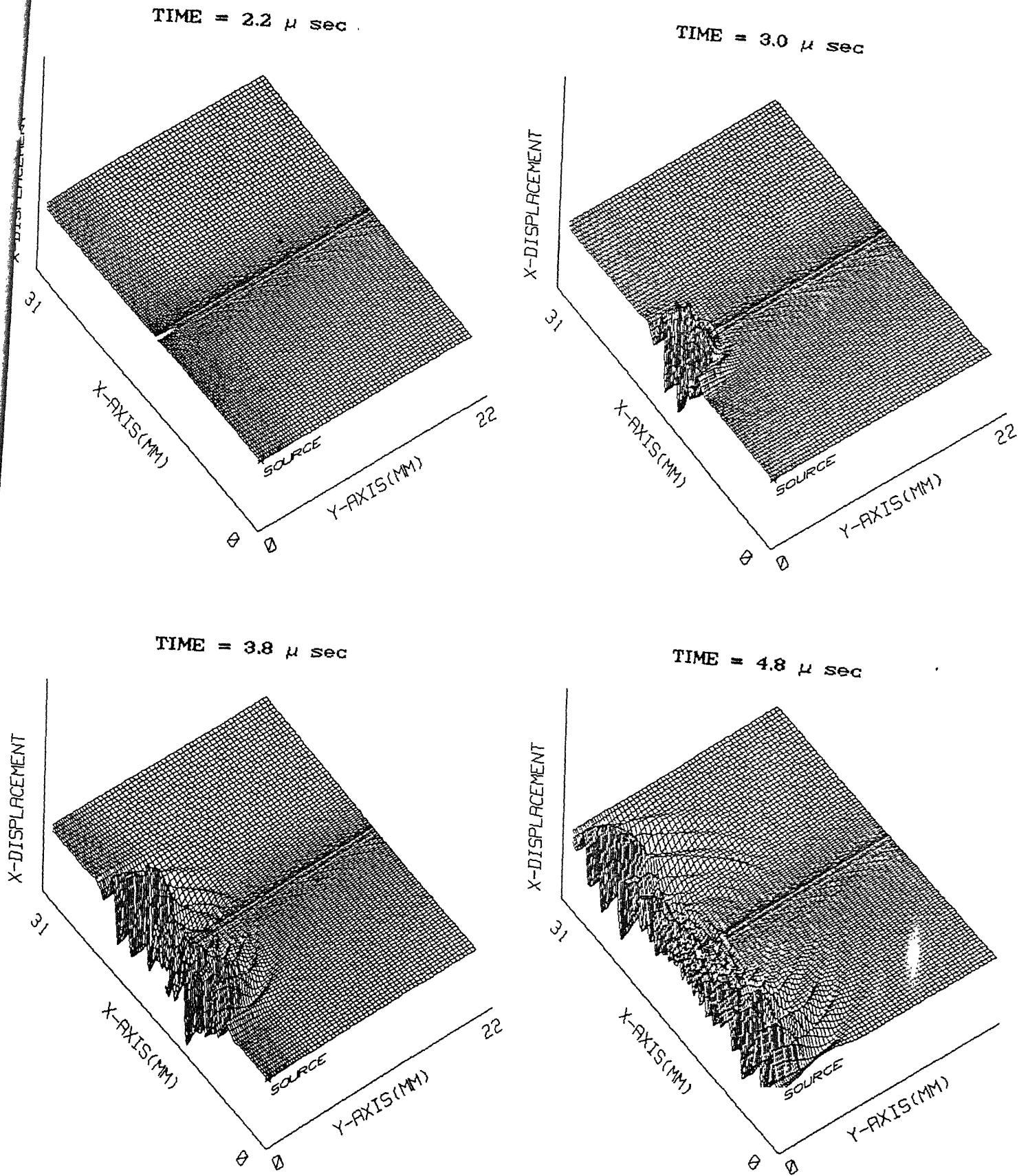


Fig. 4.36 Snapshots of the Scattered X-Displacement Field After a Plane Compression Wave has Interacted with Wedge Crack.

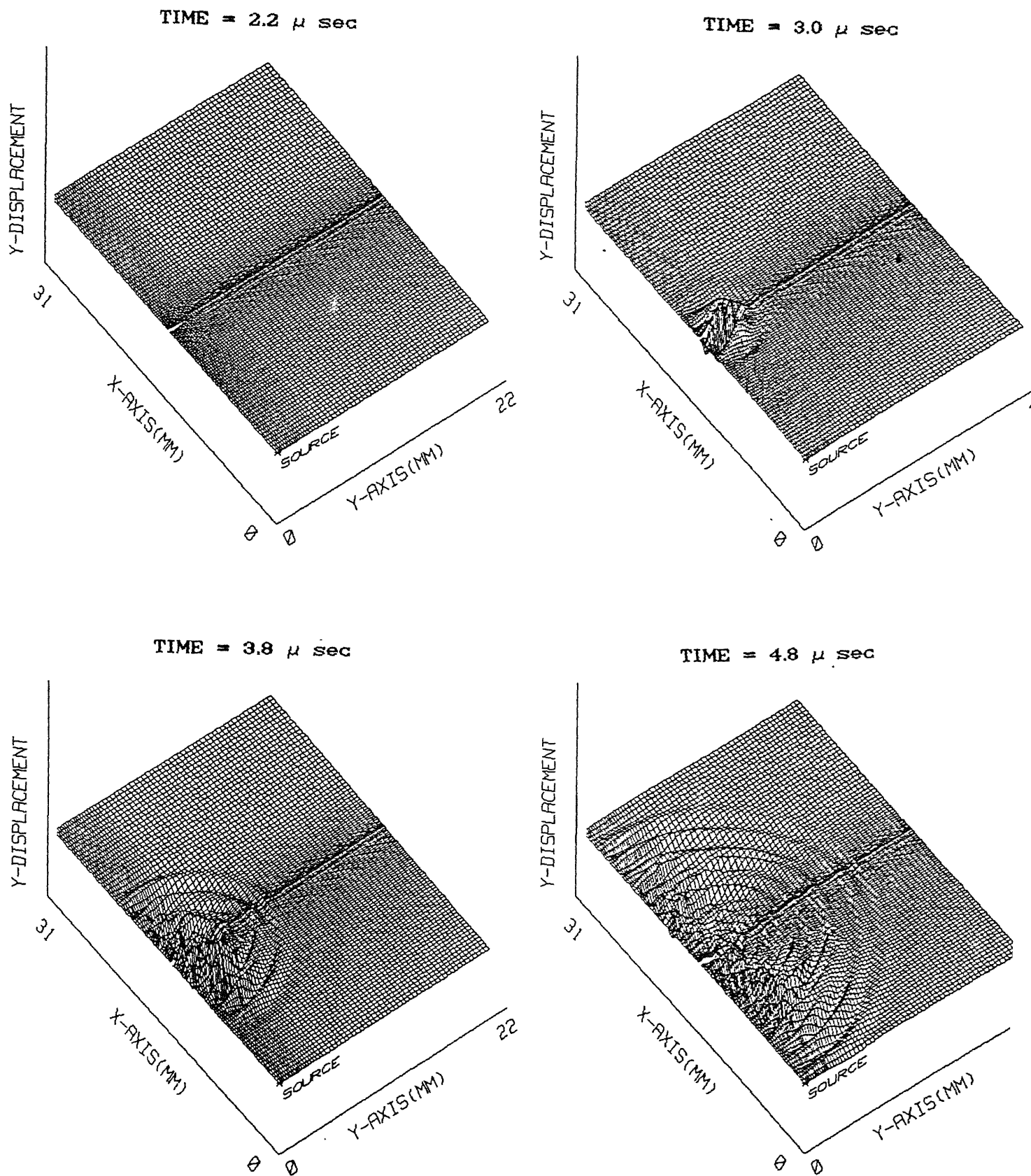


Fig. 4.37 Snapshots of the Scattered Y-Displacement Field After a Plane Compression Wave has Interacted with Wedge Crack.

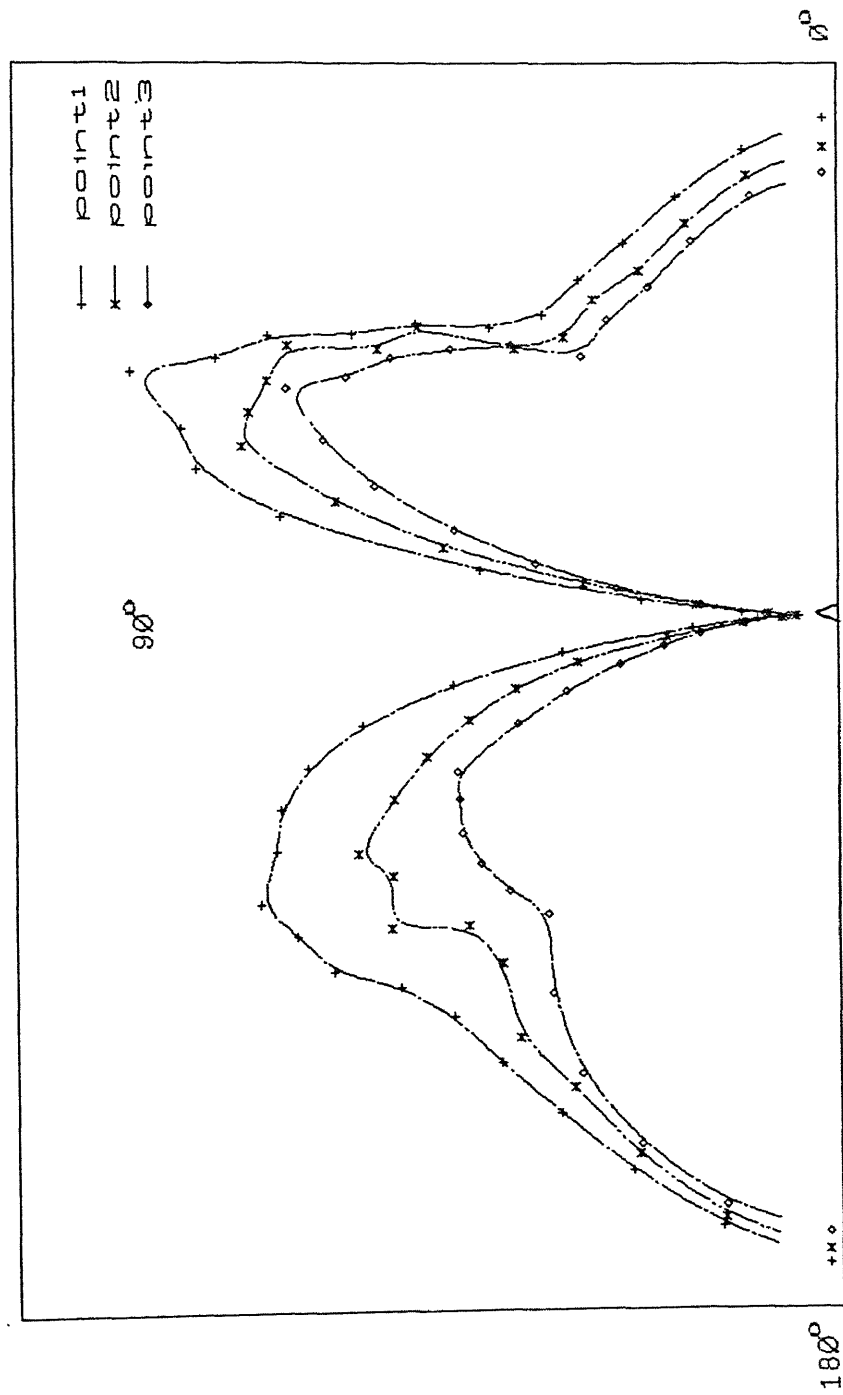


Fig. 4.38 Angular Distribution of Scattered Amplitudes after a Plane Compression Wave interaction with Wedge Crack.

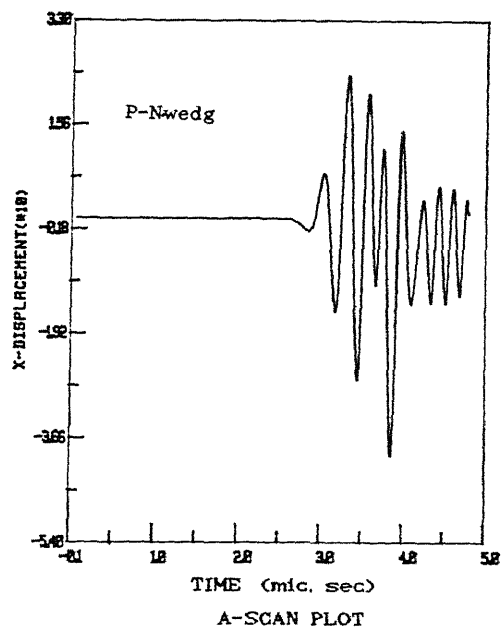
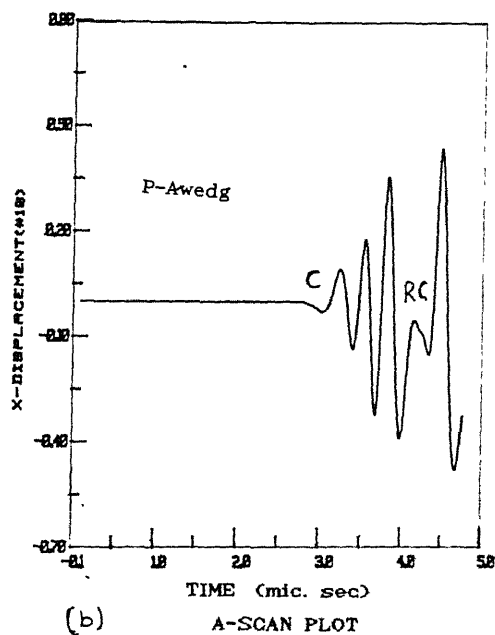
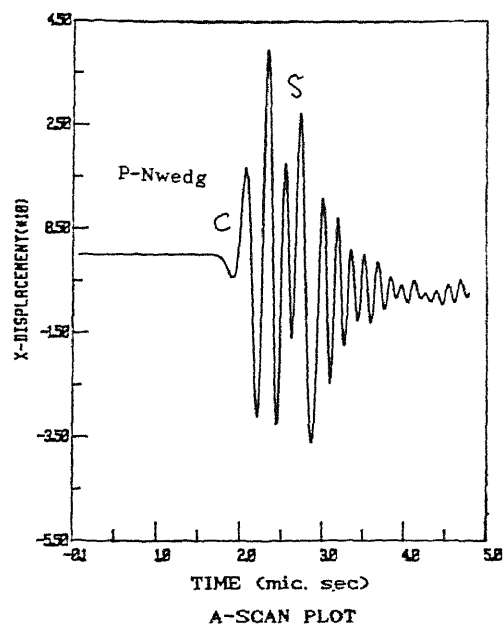
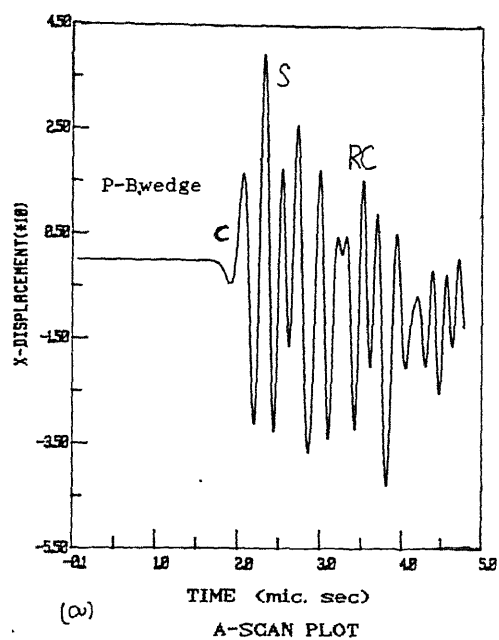
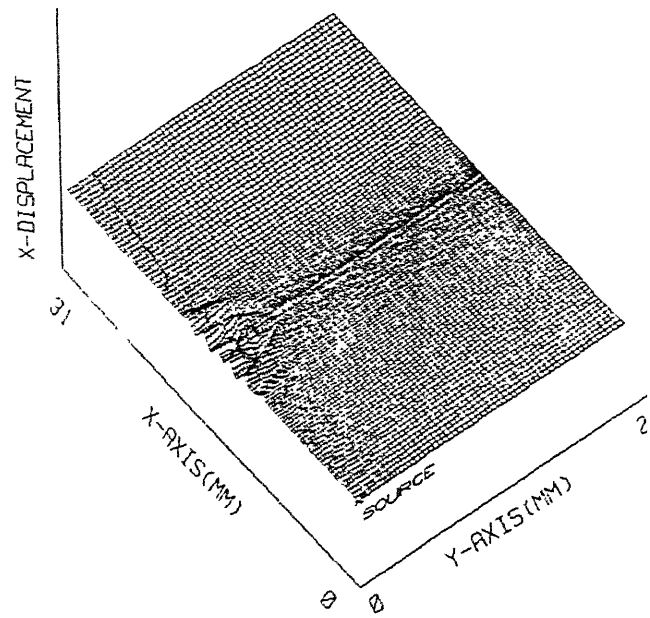
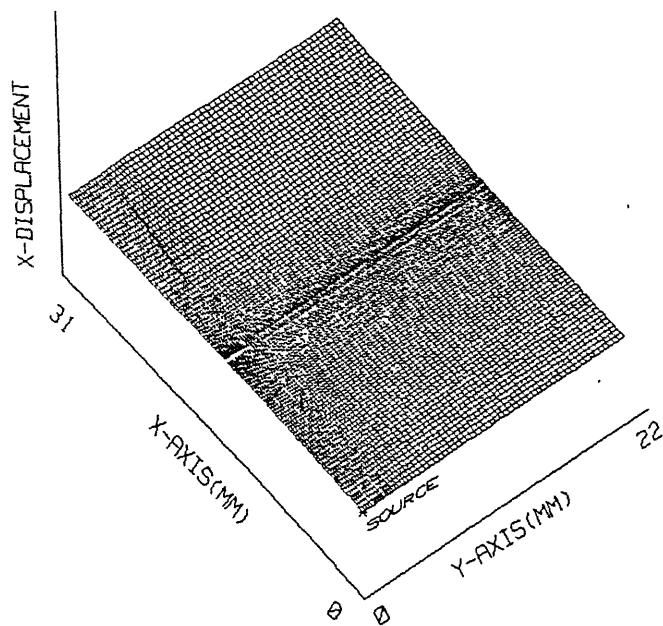
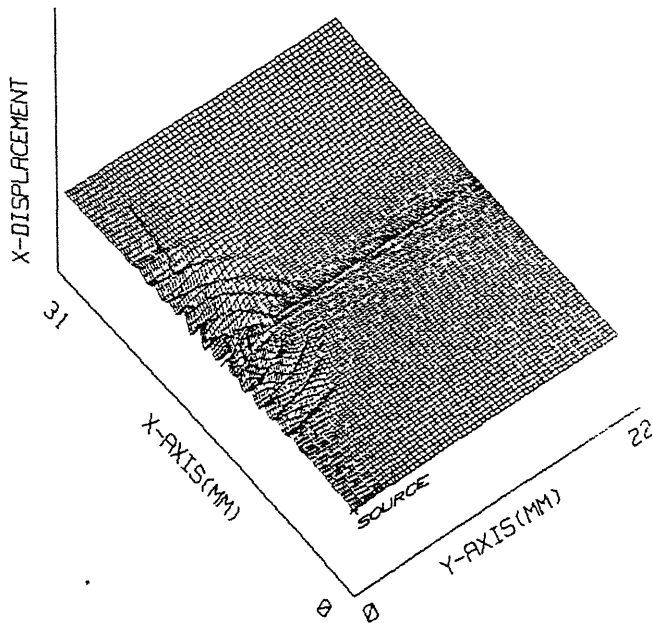


Fig. 4.39(a) A-Scan plot at a point before the Wedg crack.

(b) A-Scan plot at a point after the Wedg crack.



TIME = 4.0  $\mu$  sec



TIME = 5.2  $\mu$  sec

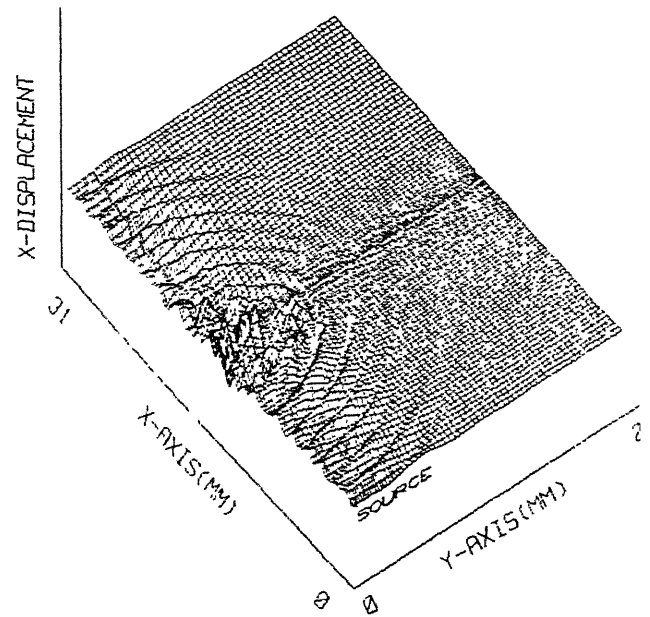
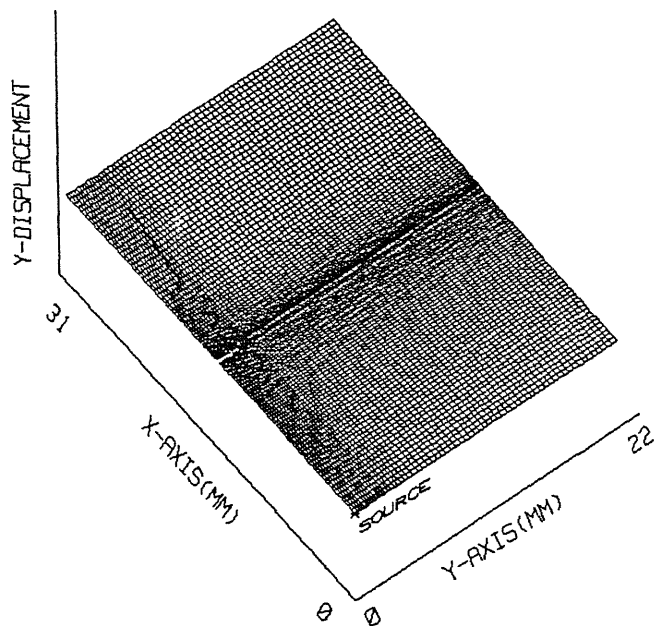
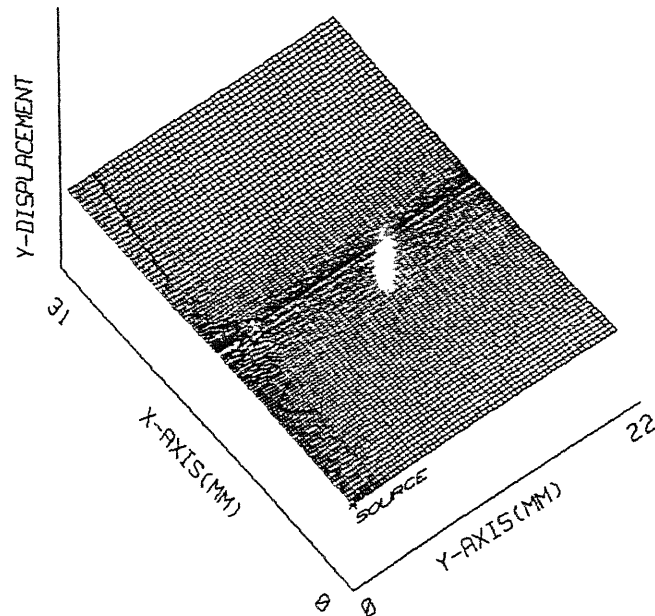


Fig. 4.40 Snapshots of the Scattered X-Displacement Field After a Plane Shear Wave has Interacted with Wedge Crack.

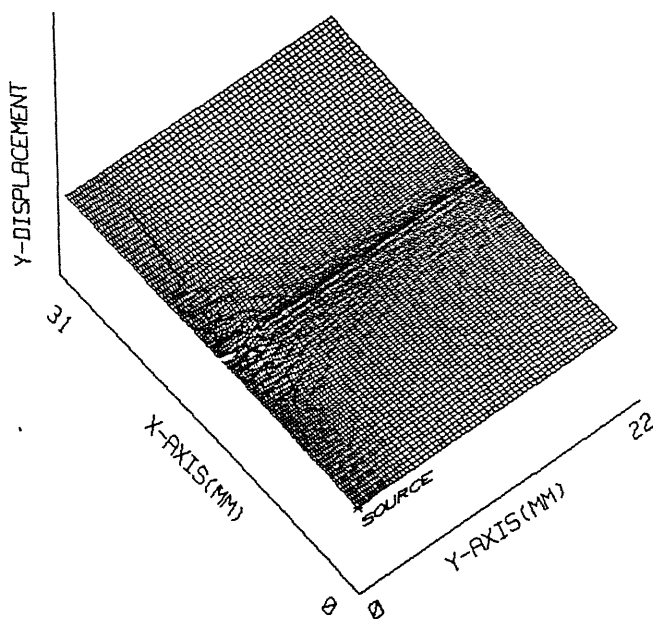
TIME = 2.4  $\mu$  sec



TIME = 3.2  $\mu$  sec



TIME = 4.0  $\mu$  sec



TIME = 5.2  $\mu$  sec

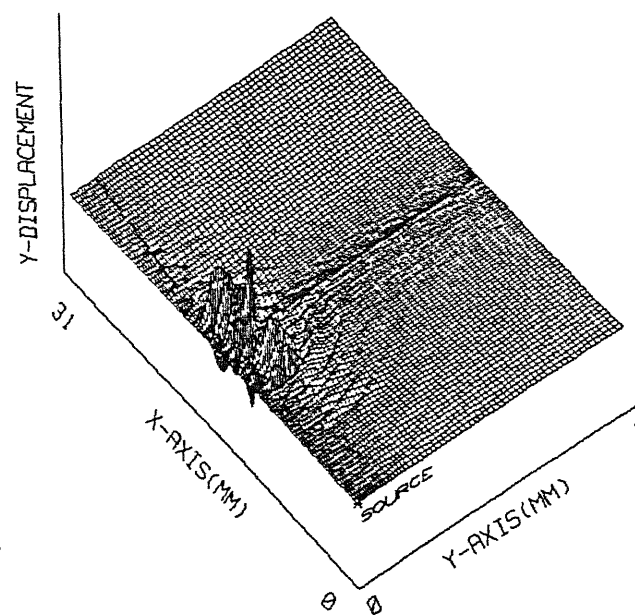


Fig. 4.41 Snapshots of the Scattered Y-Displacement Field After a Plane Shear Wave has Interacted with Wedge Crack.

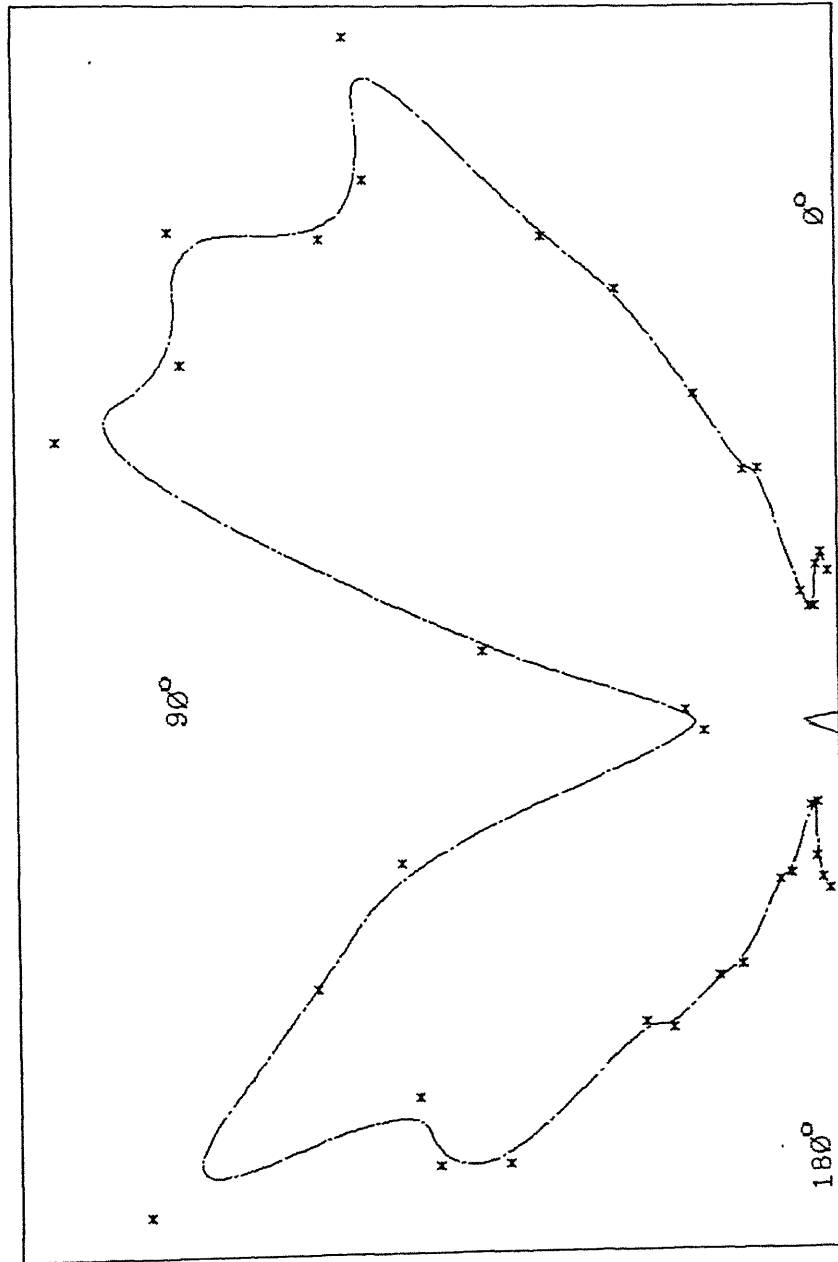


Fig. 4.42 Angular Distribution of Scattered Amplitudes after a Plane Shear Wave interaction with Wedge Crack.



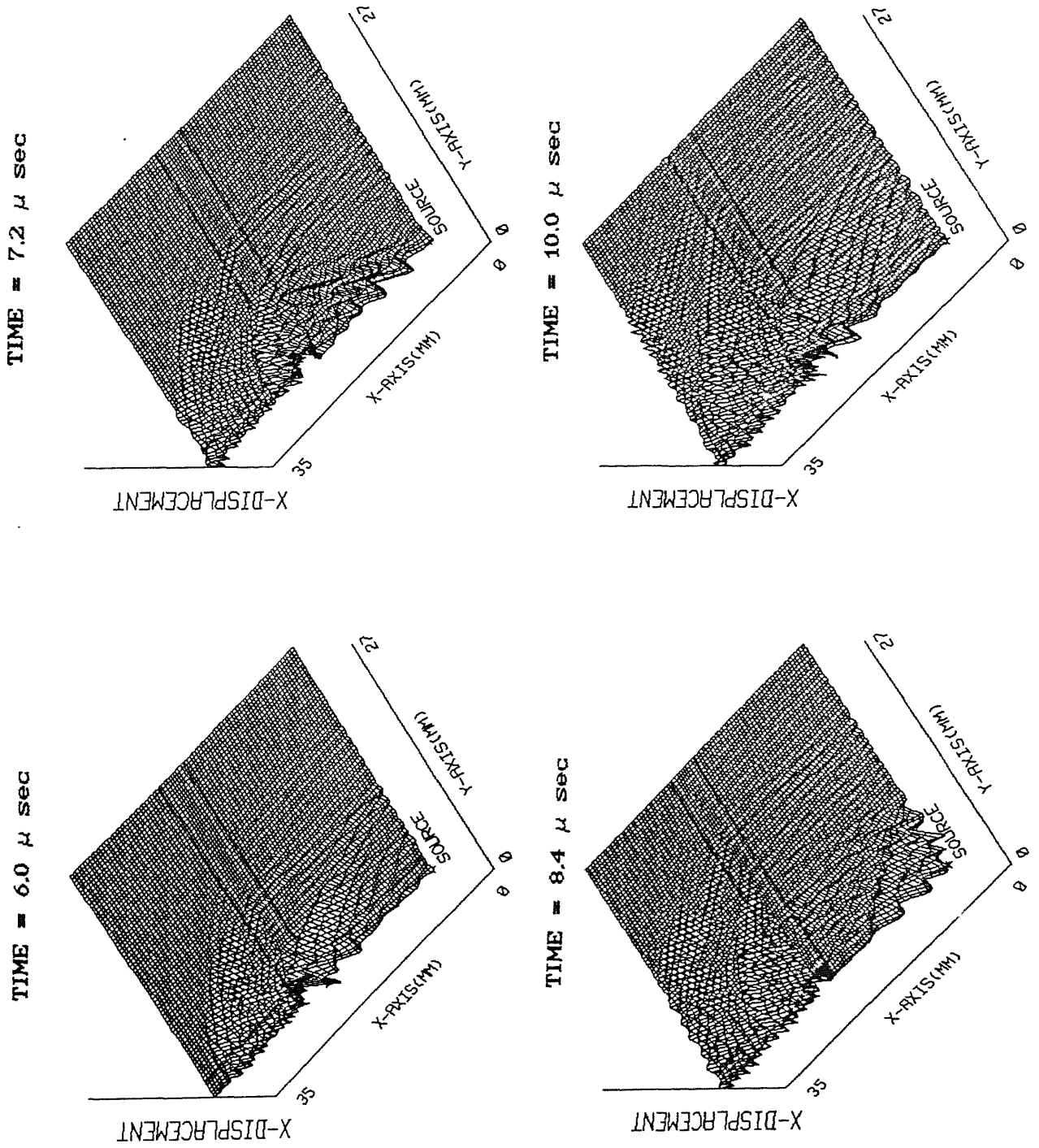


Fig. 4.43 X-displacement field : Plane Compression wave interaction with a hole in Layered Structure.

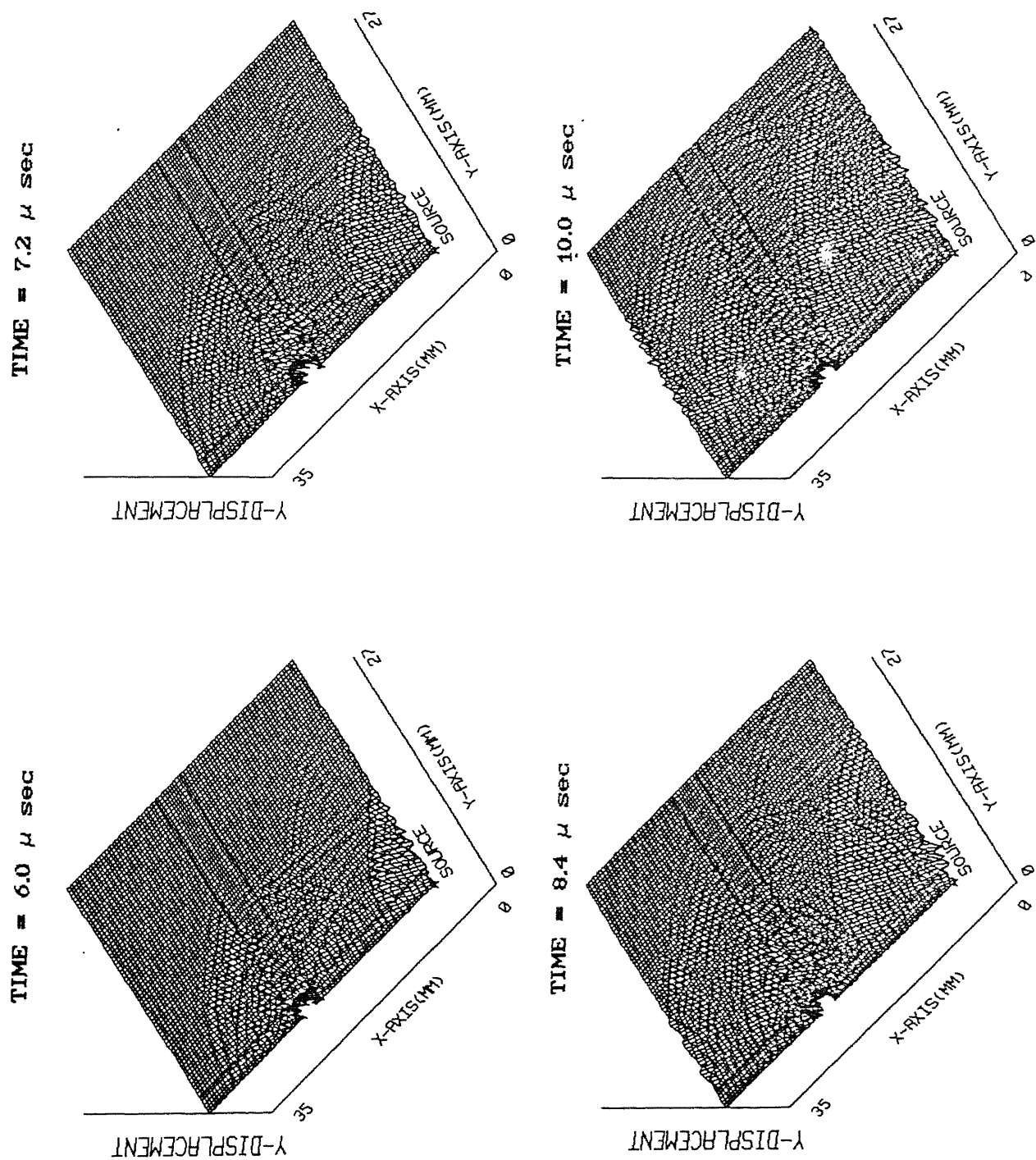


Fig. 4.44 Y-displacement field : Plane Compression wave interaction with a hole in Layered Structure.

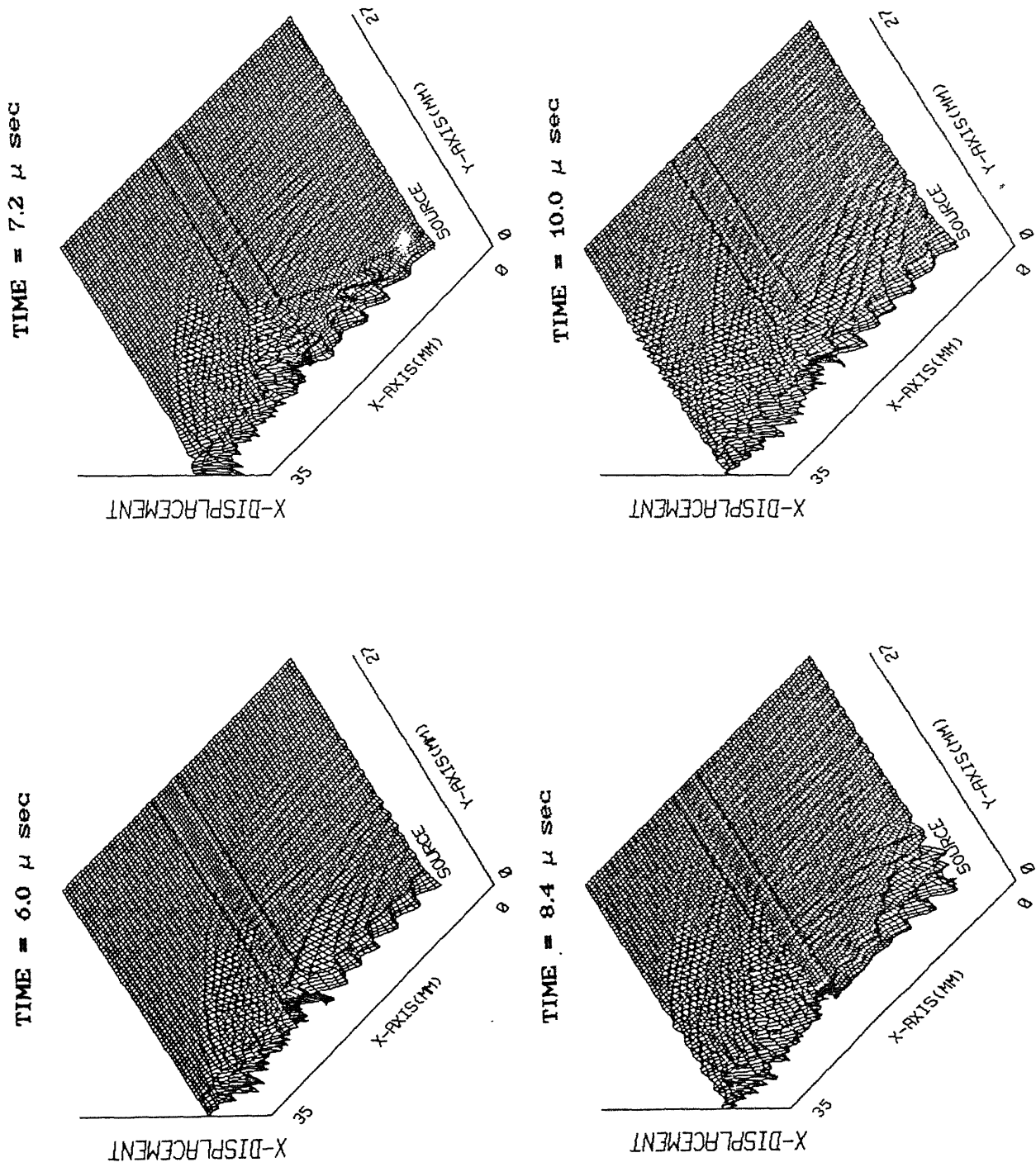


Fig. 4.45 Scattered X- disp. field : plane Compression wave interaction with a hole in Layered Structure.

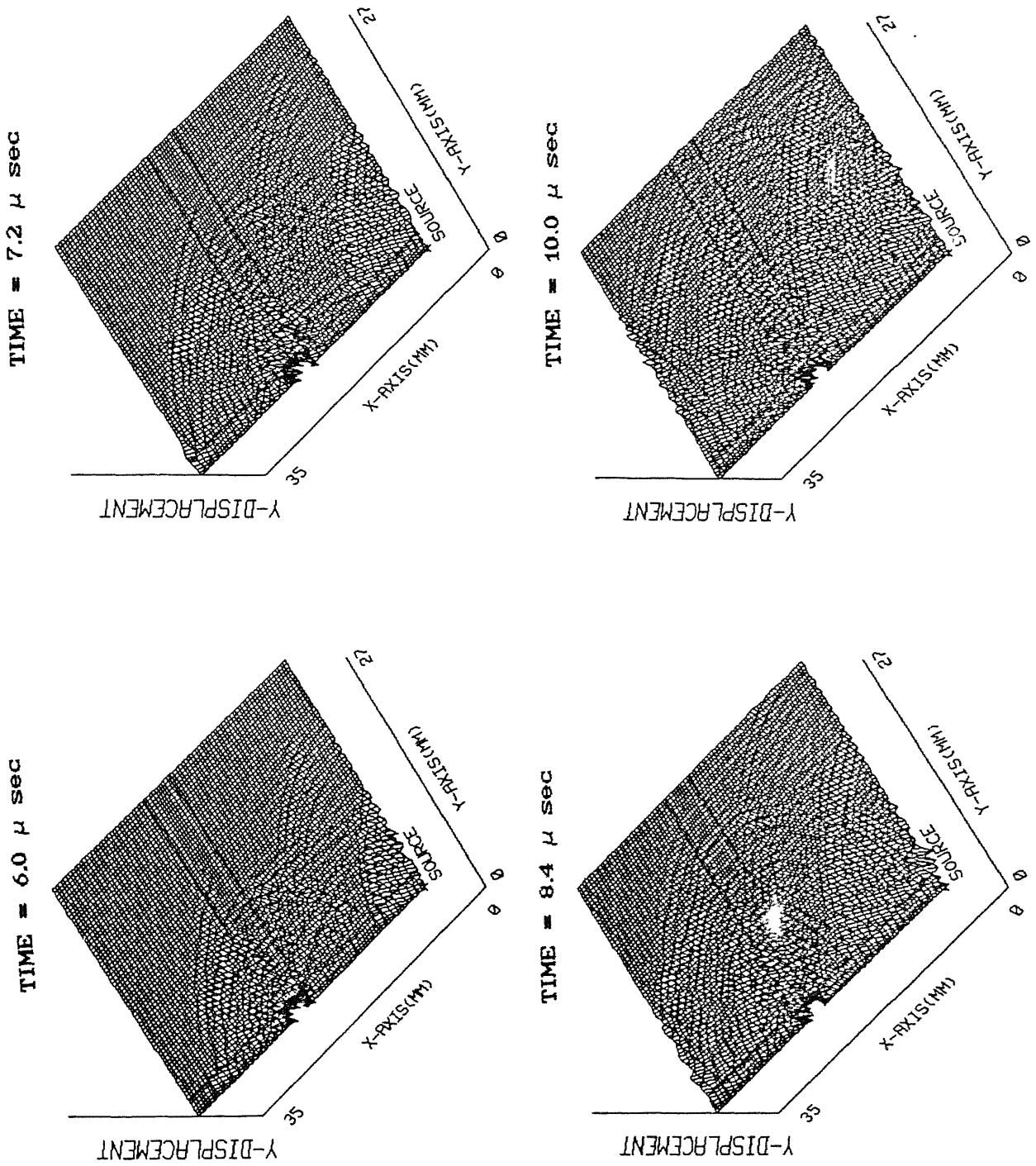


Fig. 4.46 Scattered Y- disp. field : plane Compression wave interaction with a hole in Layered Structure.

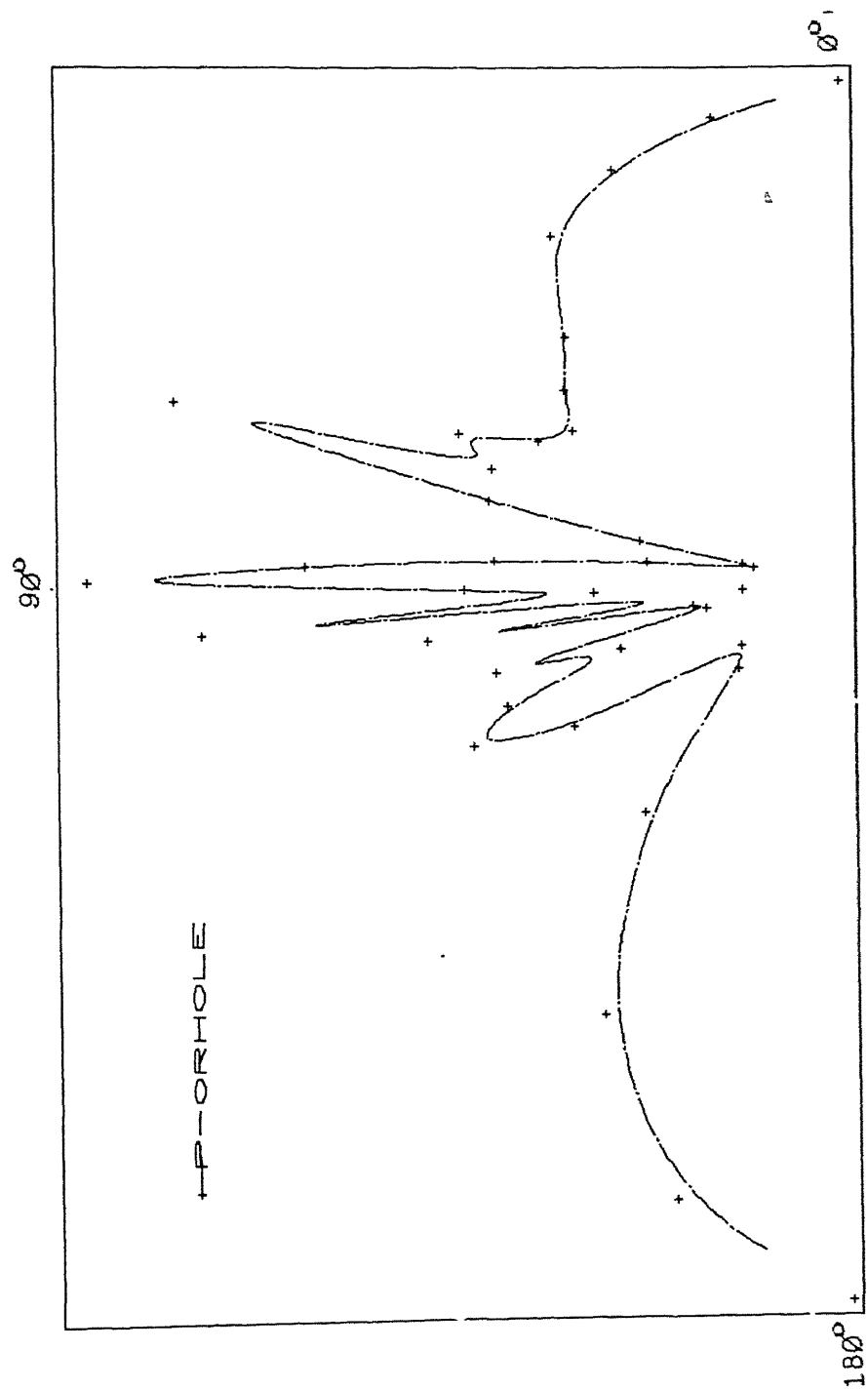


Fig. 4.47 Polar plot of Scattered amplitudes after a Compression wave interacts with a hole in Layered Structure.

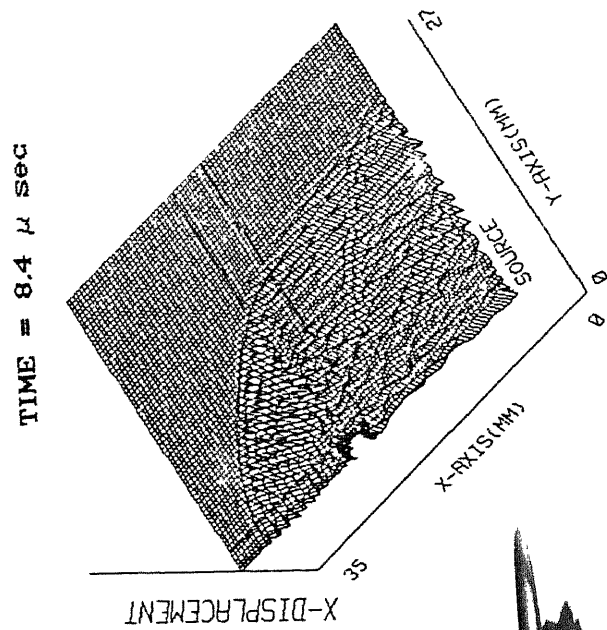
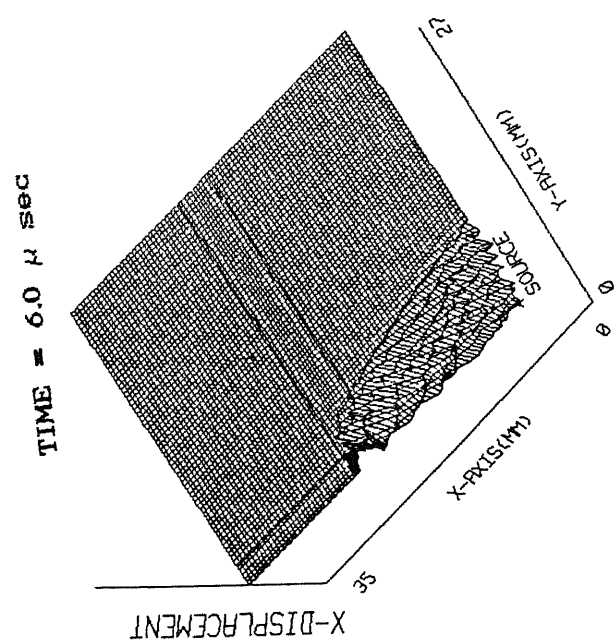
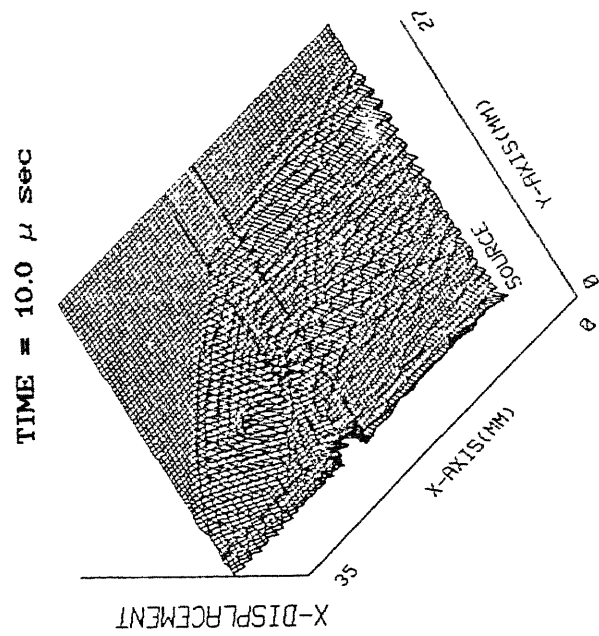
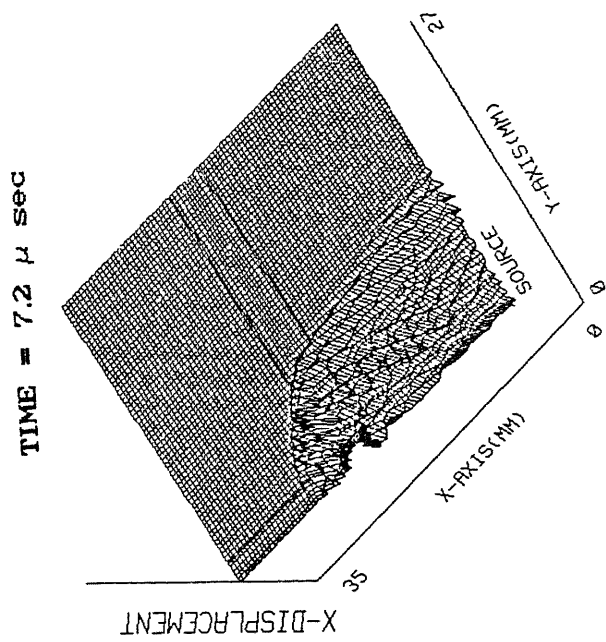


Fig. 4.48 X-displacement field : Plane Shear wave interaction with a hole in Layered Structure.

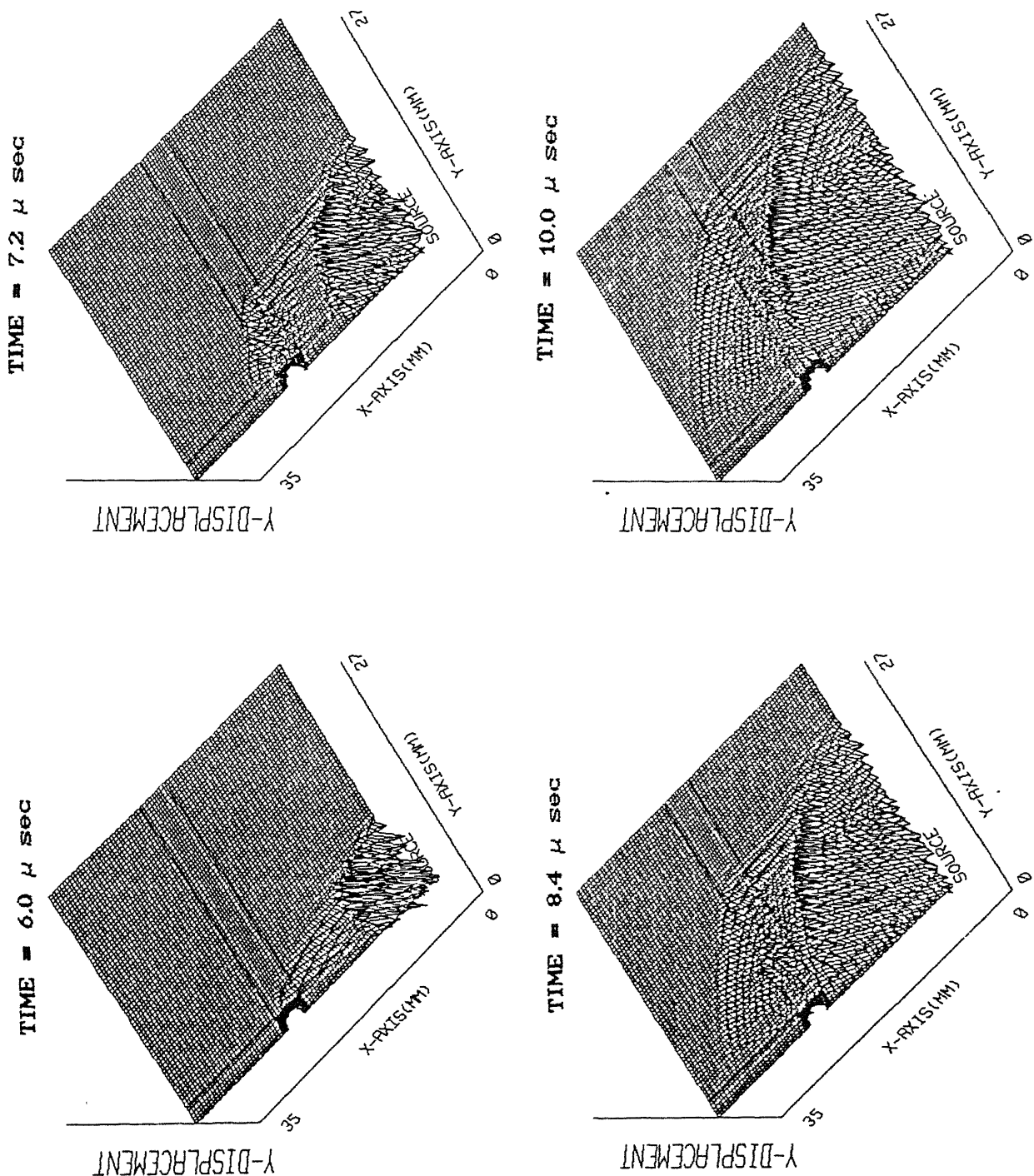


Fig. 4.49 Y-displacement field : Plane Shear wave interaction with a hole in layered Structure.

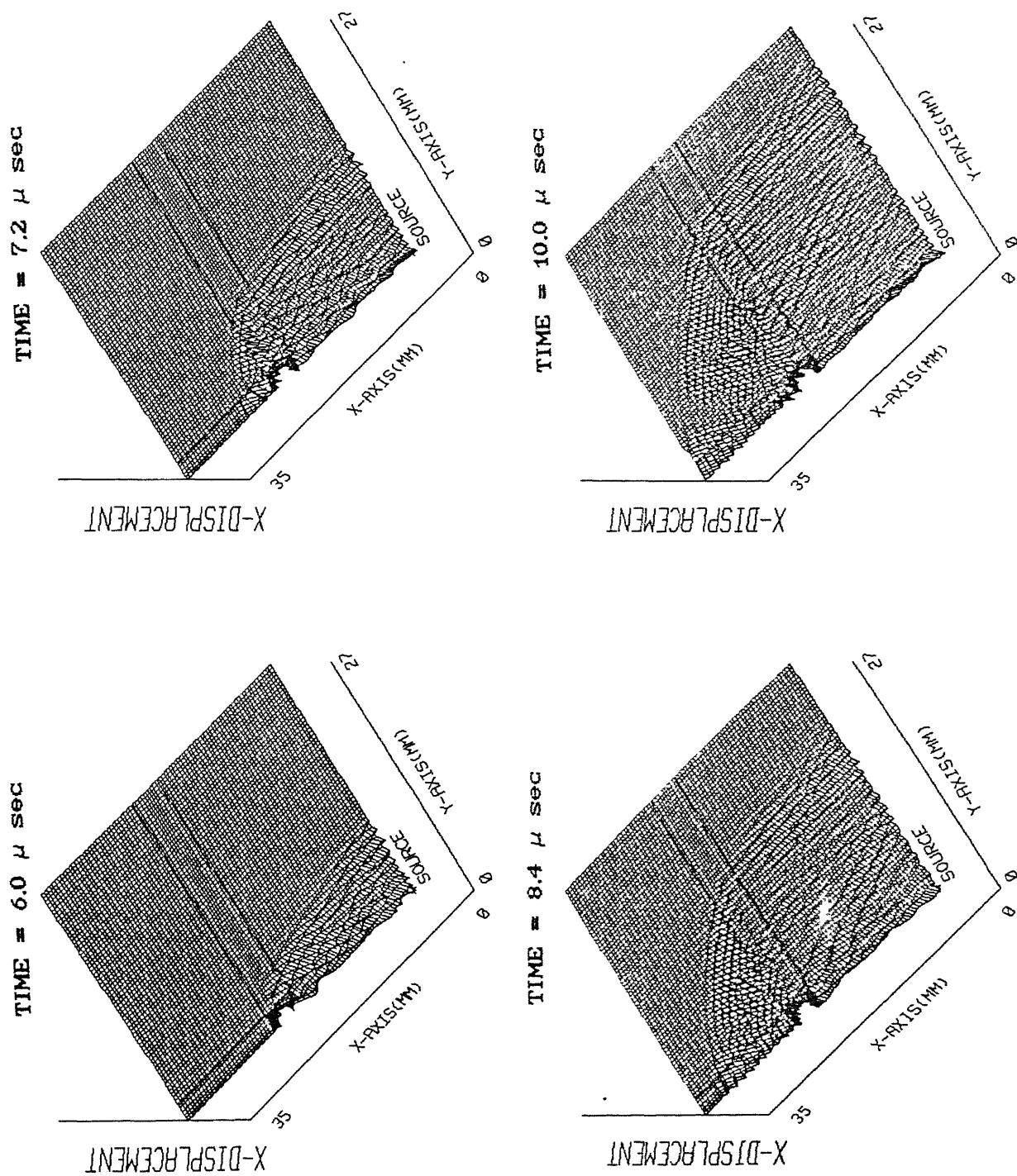


Fig. 4.50 Scattered X- disp. field : plane Shear wave interaction with a hole in Layered Structure.



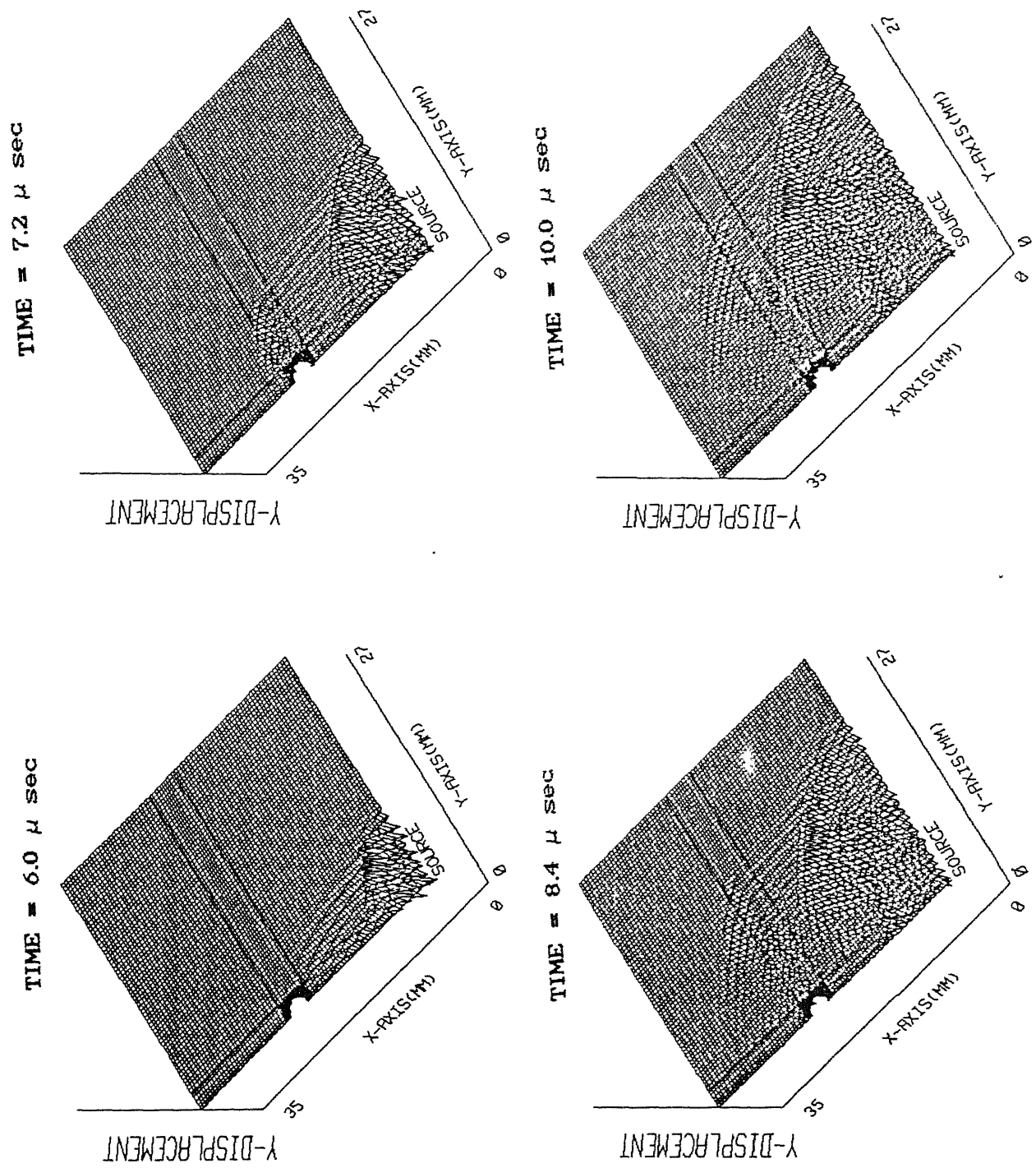


Fig. 4.51 Scattered Y- disp. field : plane Shear wave

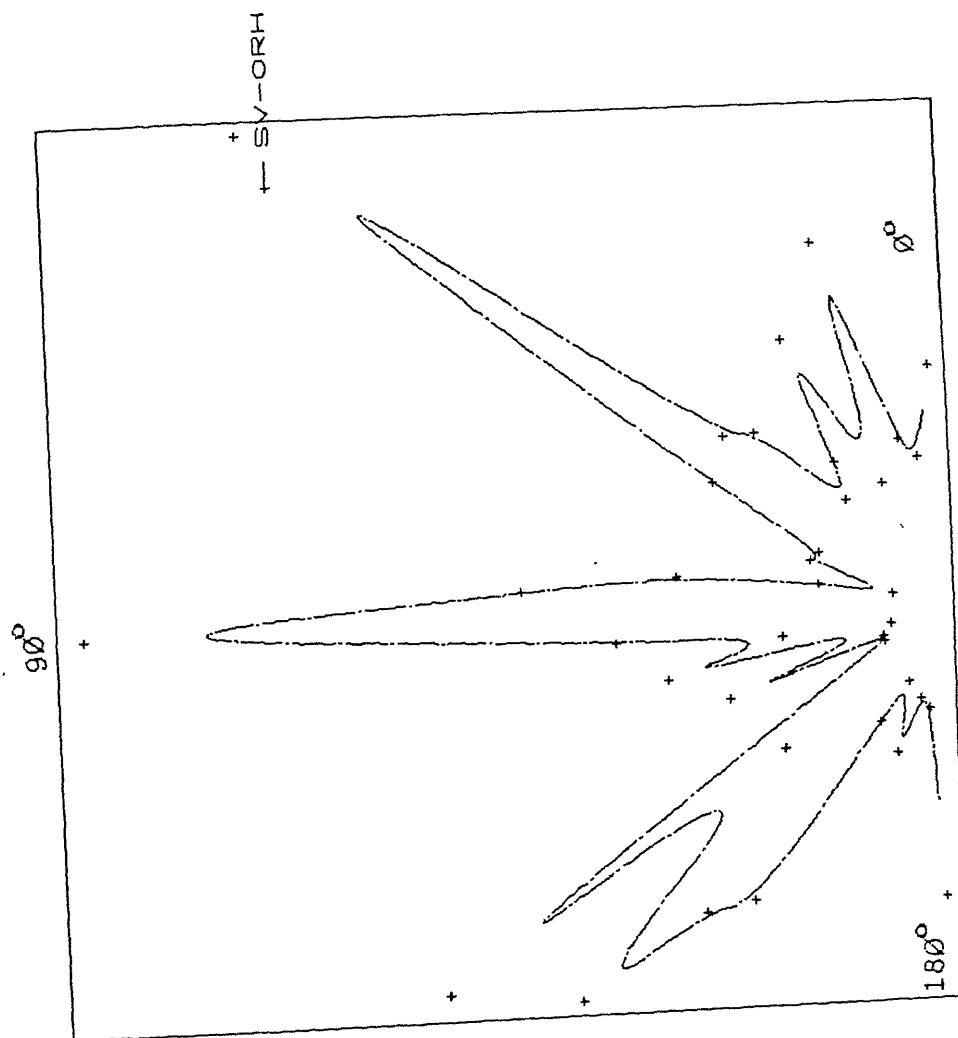


Fig. 4.52 Polar plot of Scattered amplitudes after a Shear wave interacts with a hole in Layered Structure.

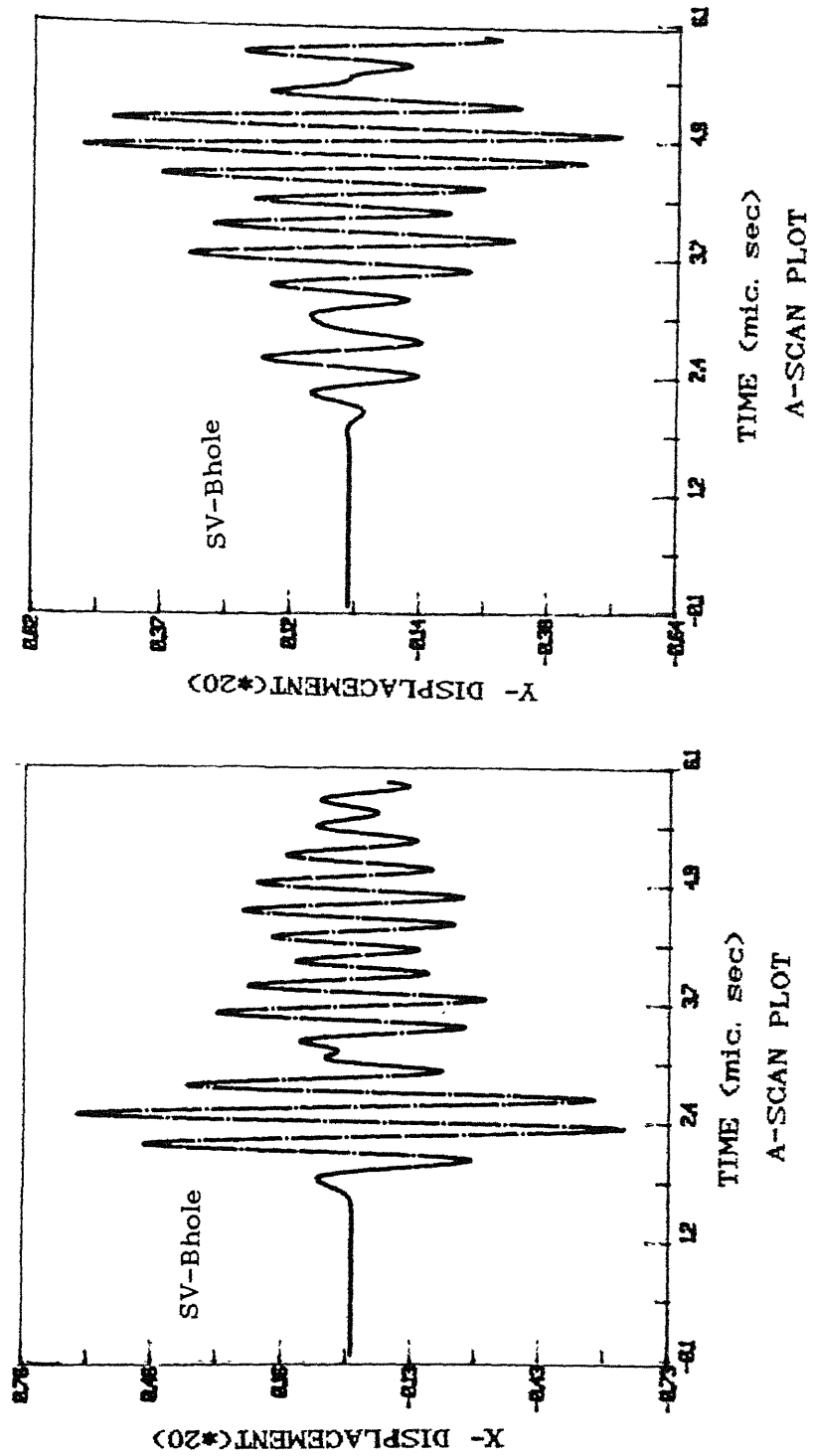


Fig. 4.53 A- Scan plot at a point before the hole in a composite laminate. ( Shear wave interaction)

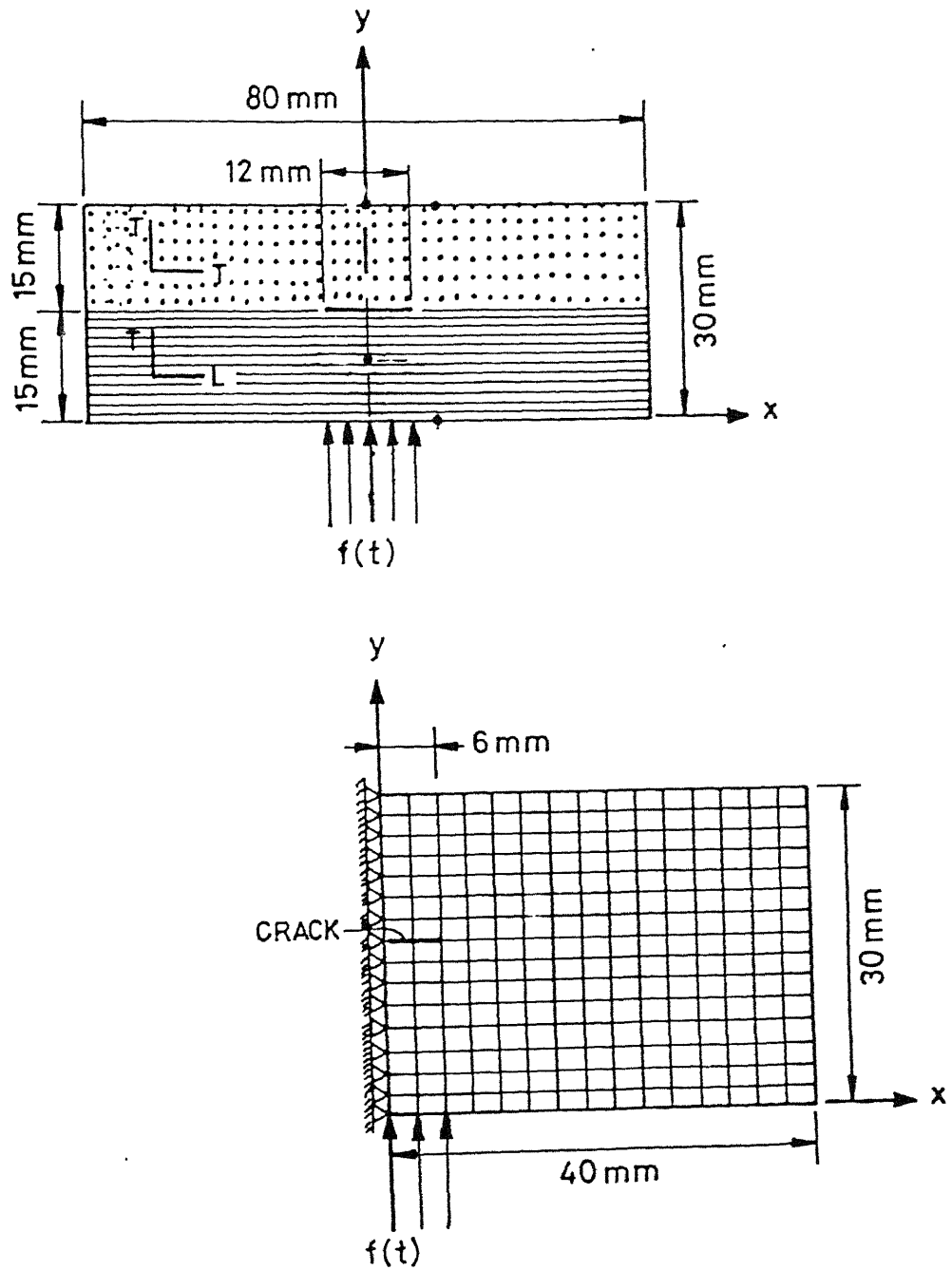


Fig. 4.54 Finite Element Discretization of Layered Composite Structure with an Interface Crack.

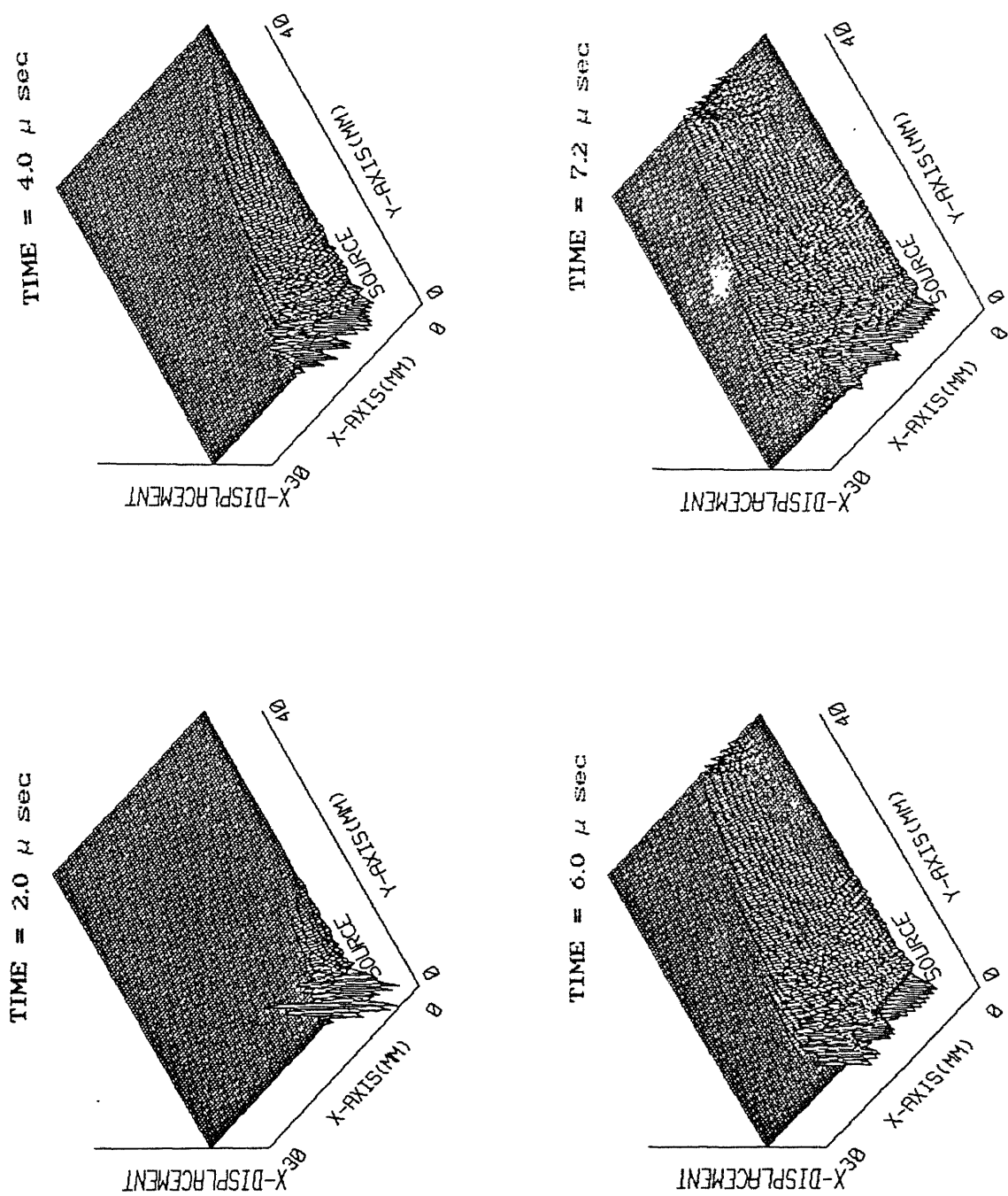


Fig. 4.55 X-displacement field : Plane Compression wave interaction with an Interface Crack in Layered Structure.

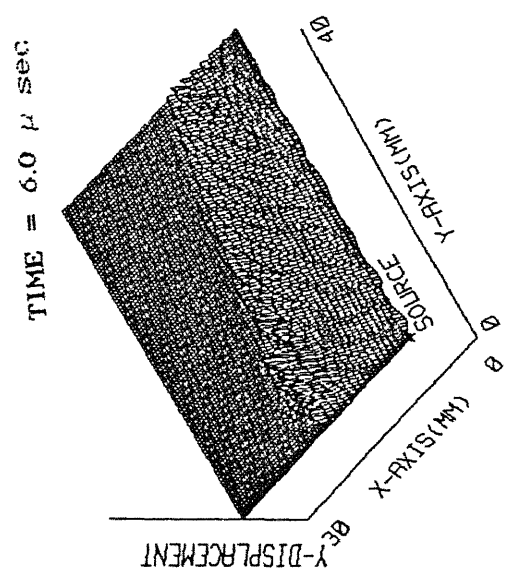
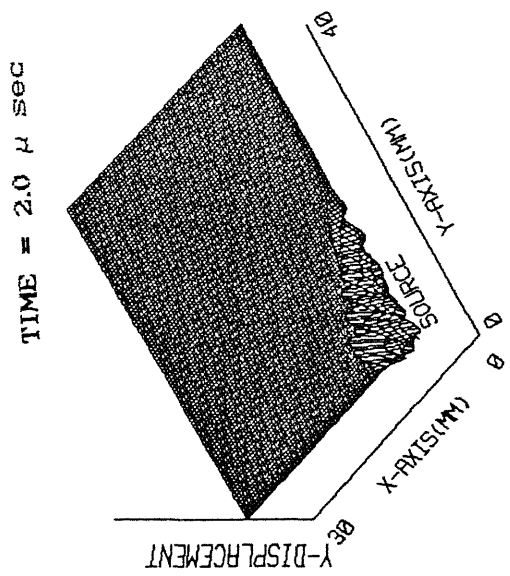
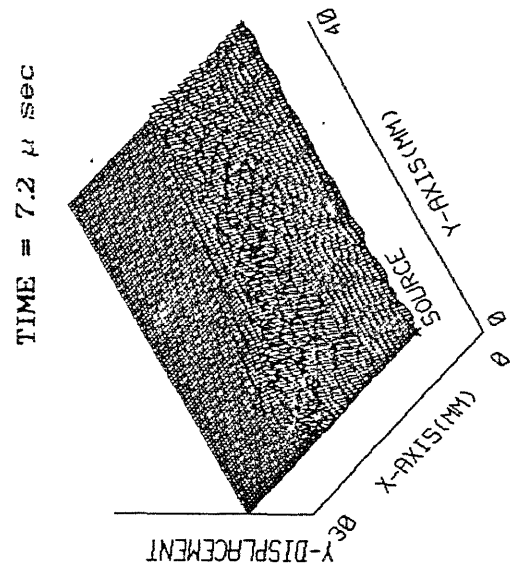
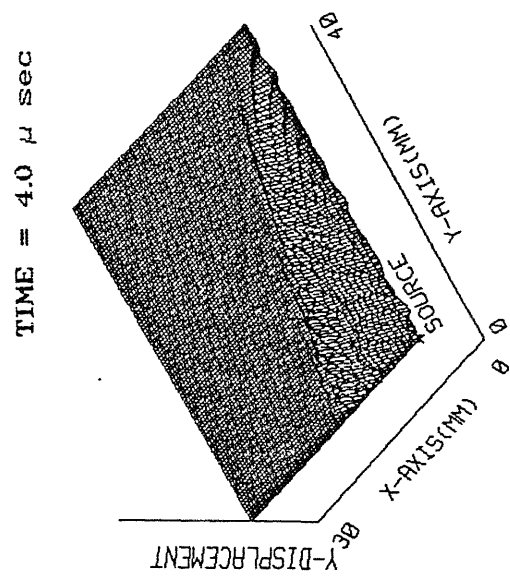


Fig. 4.56 Y-displacement field : Plane Compression wave interaction with an Interface Crack in Layered Structure.

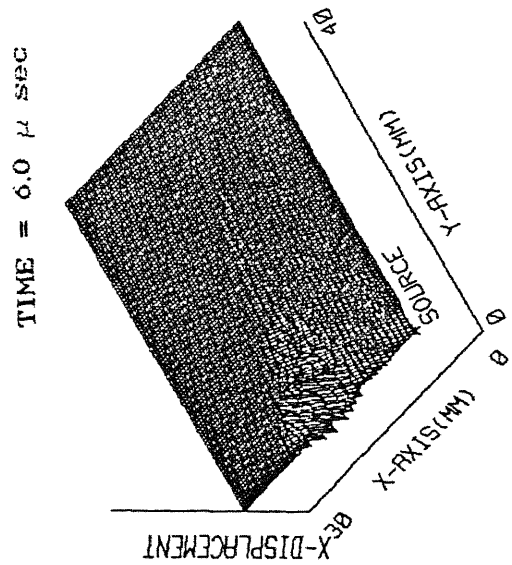
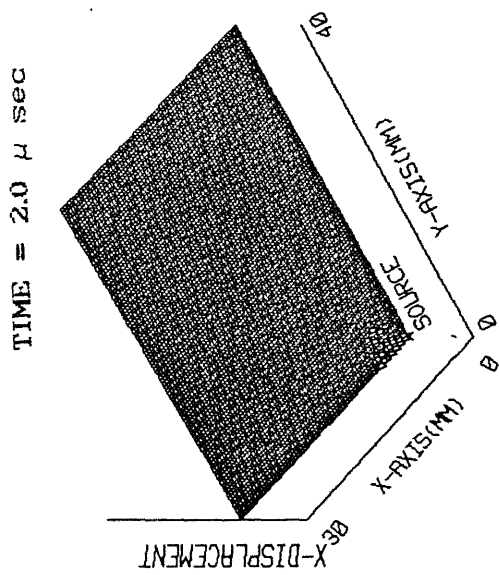
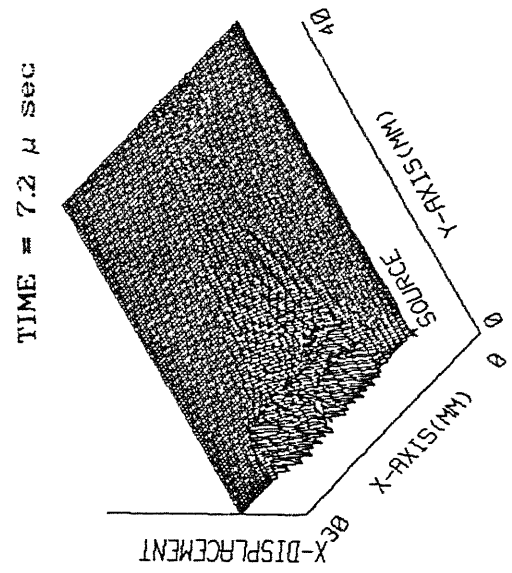
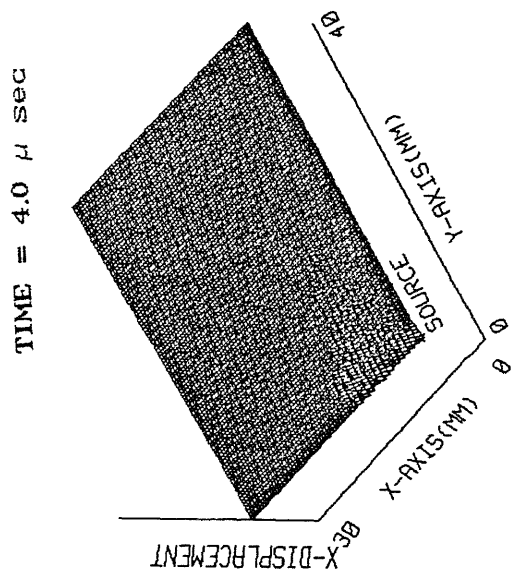


Fig. 4.57 Scattered X- disp. field : plane Compression wave interaction with an Interface Crack in Layered Structure.

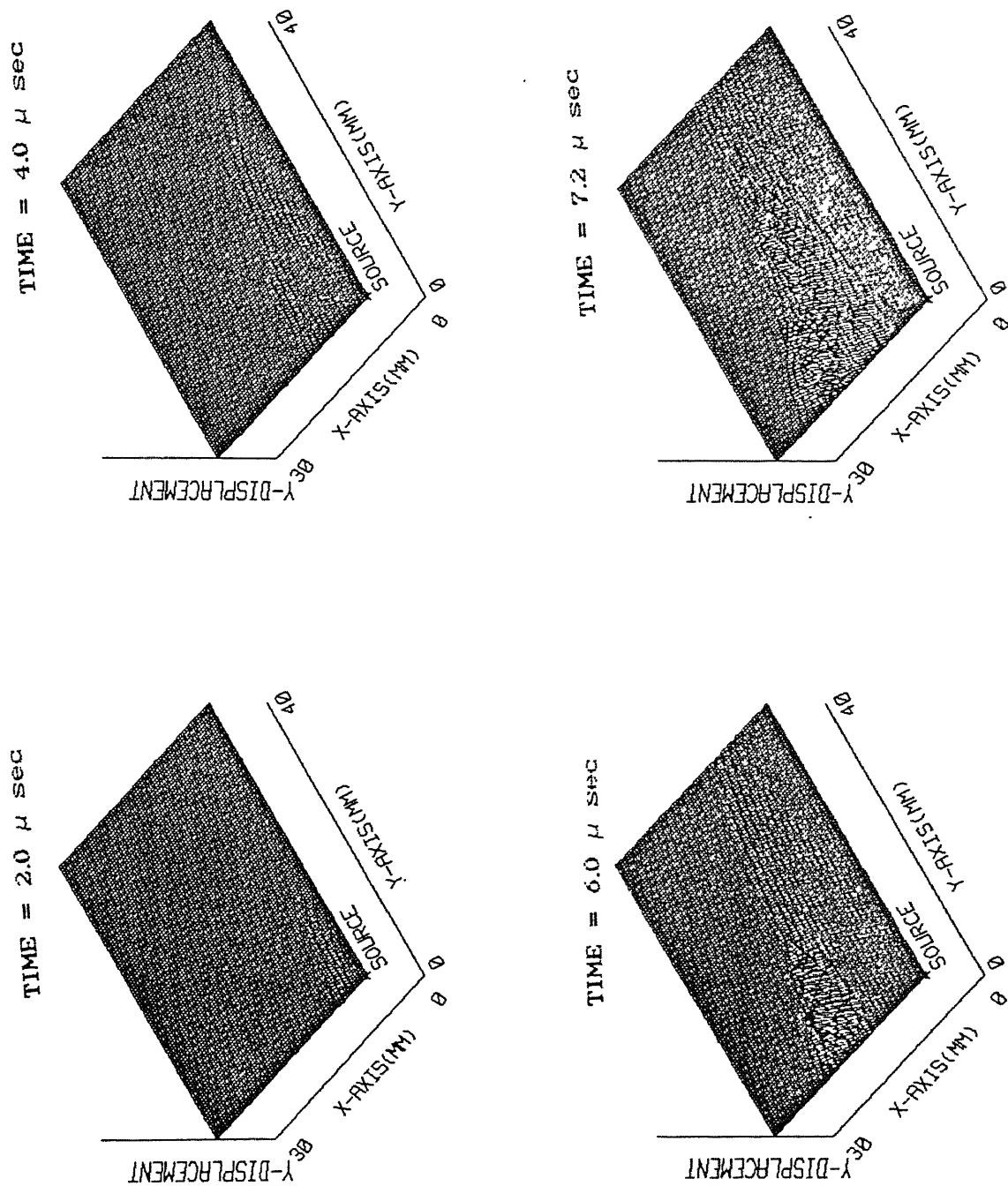


Fig. 4.58 Scattered Y- disp. field : plane Compression wave interaction with an Interface Crack in Layered Structure.



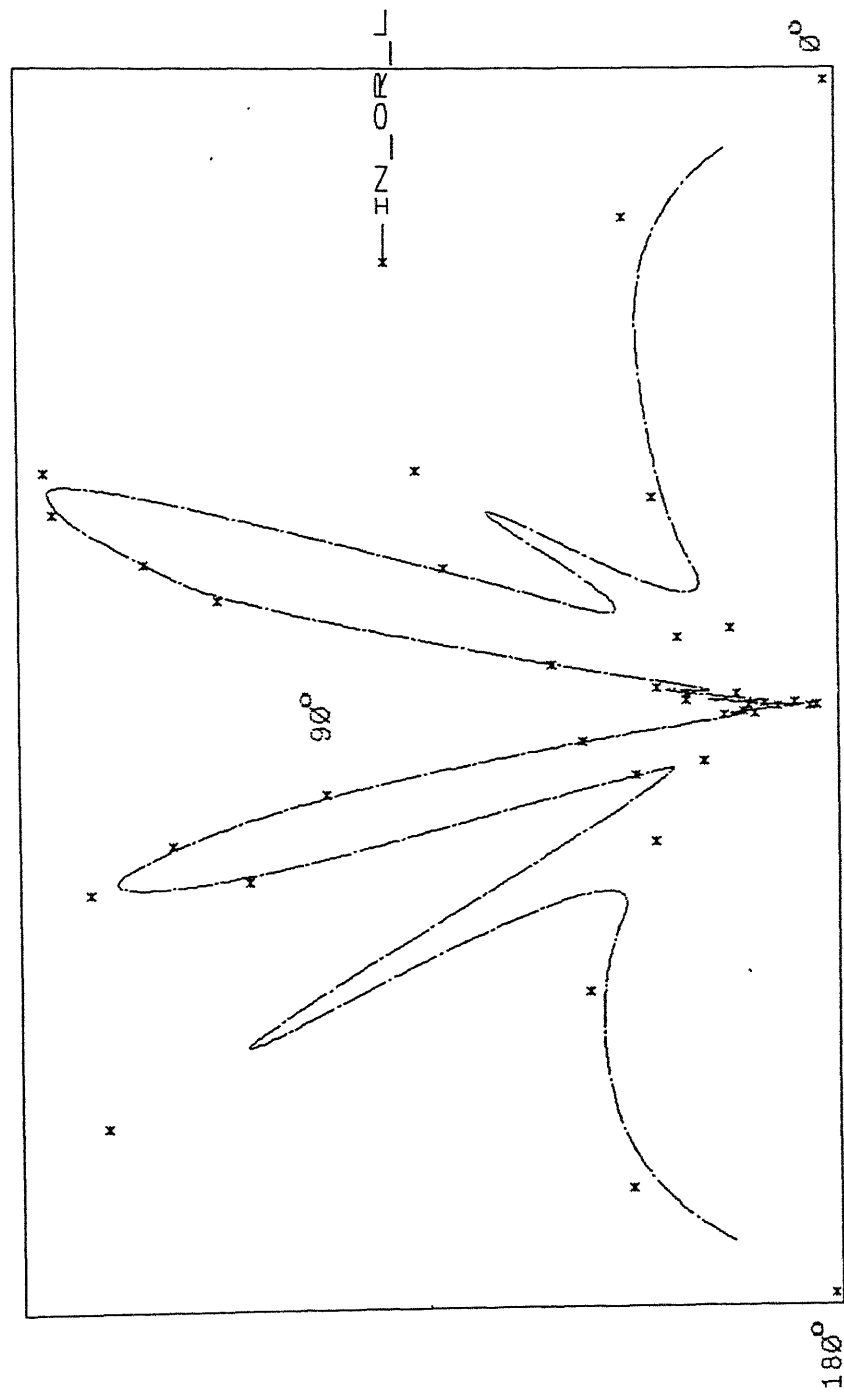


Fig. 4.59 Polar plot of Scattered amplitudes after a Compression wave interacts with an Interface Crack in Layered Structure.

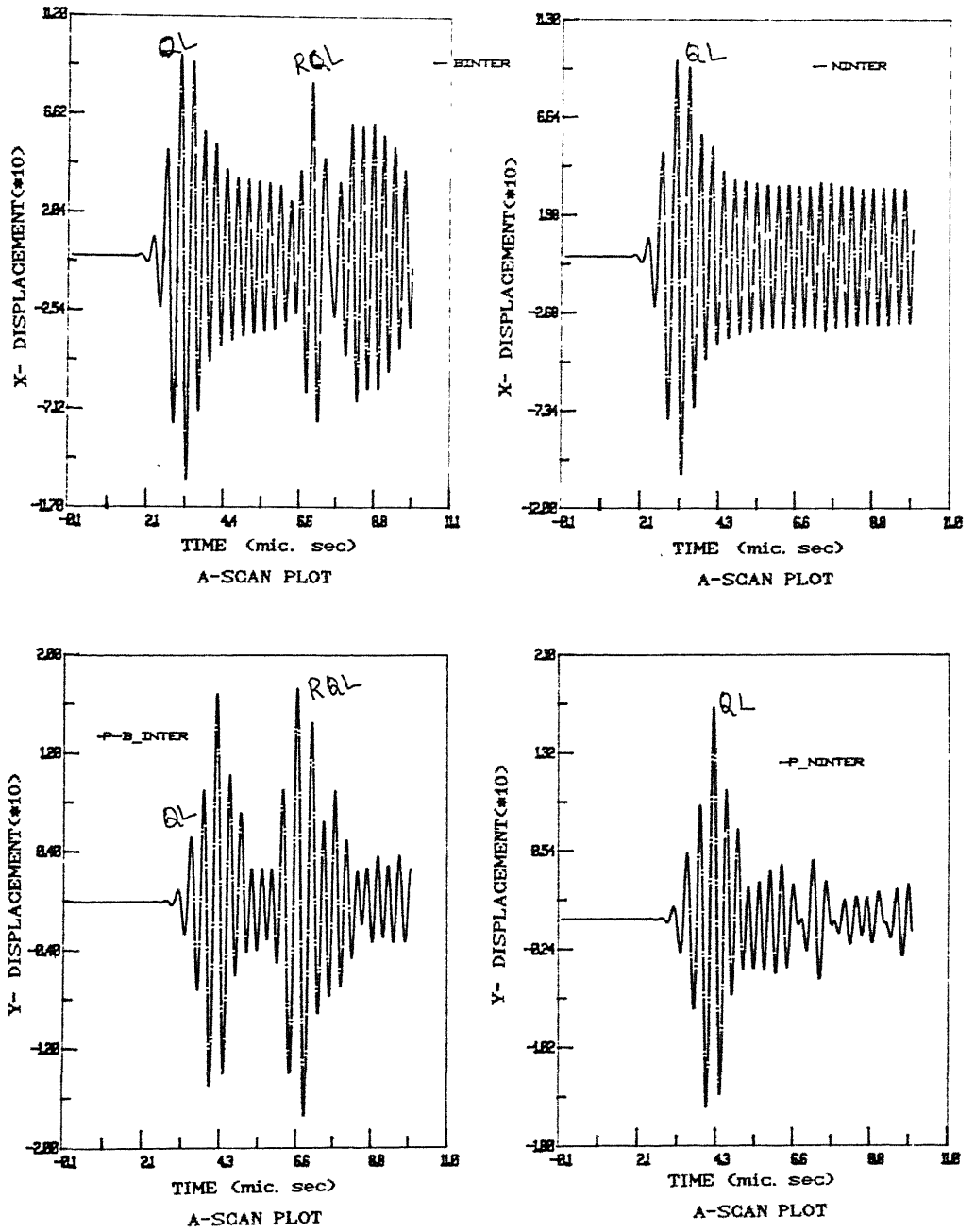


Fig. 4.60 A-Scan plots comparison in a T-L & L-T composite laminate with and without interface crack.

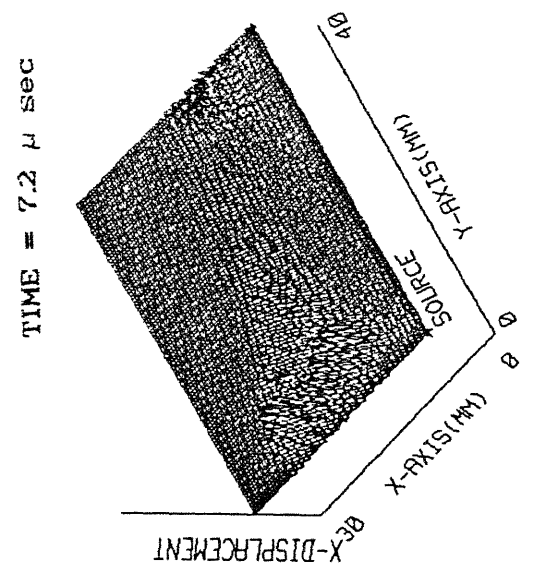
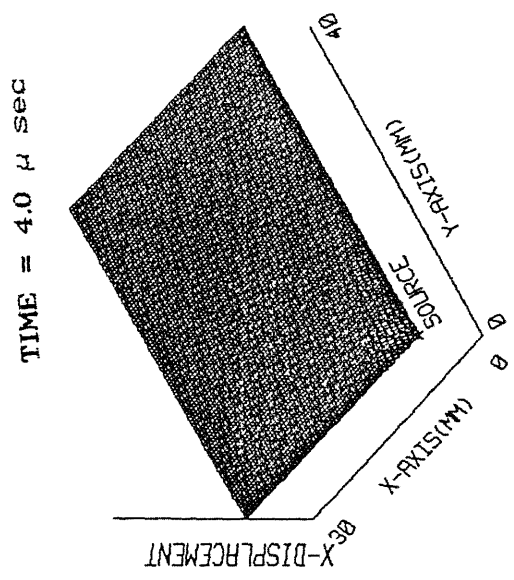
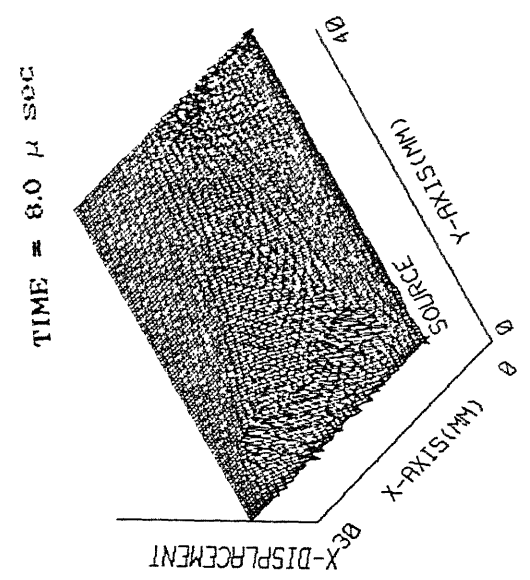
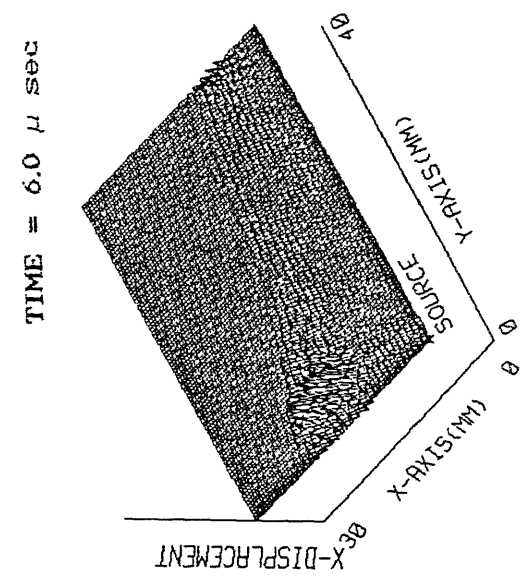


Fig. 4.61 Scattered X- disp. field : plane Shear wave

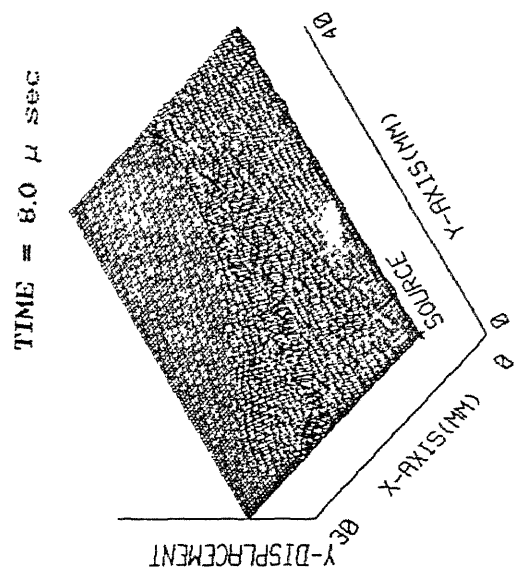
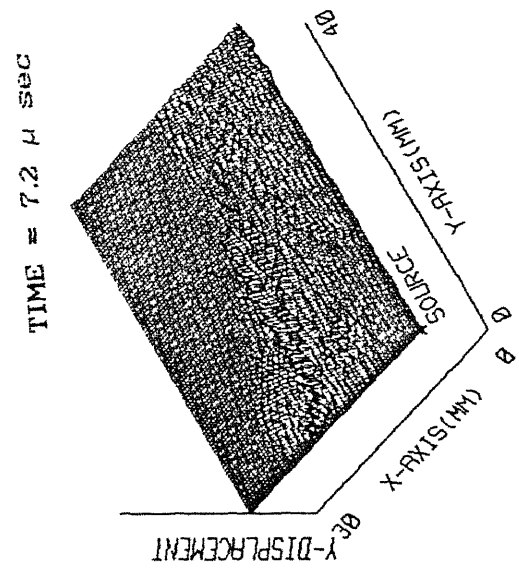
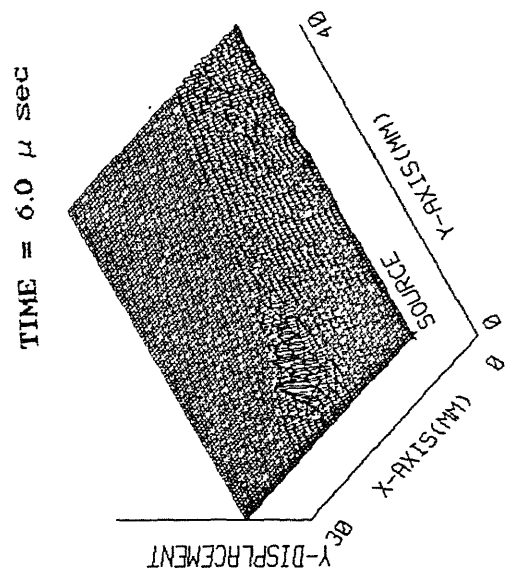
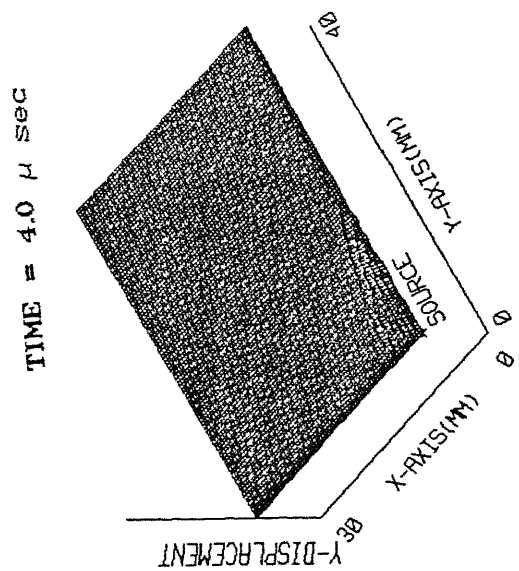


Fig. 4.62 Scattered Y- disp. field : plane Shear wave

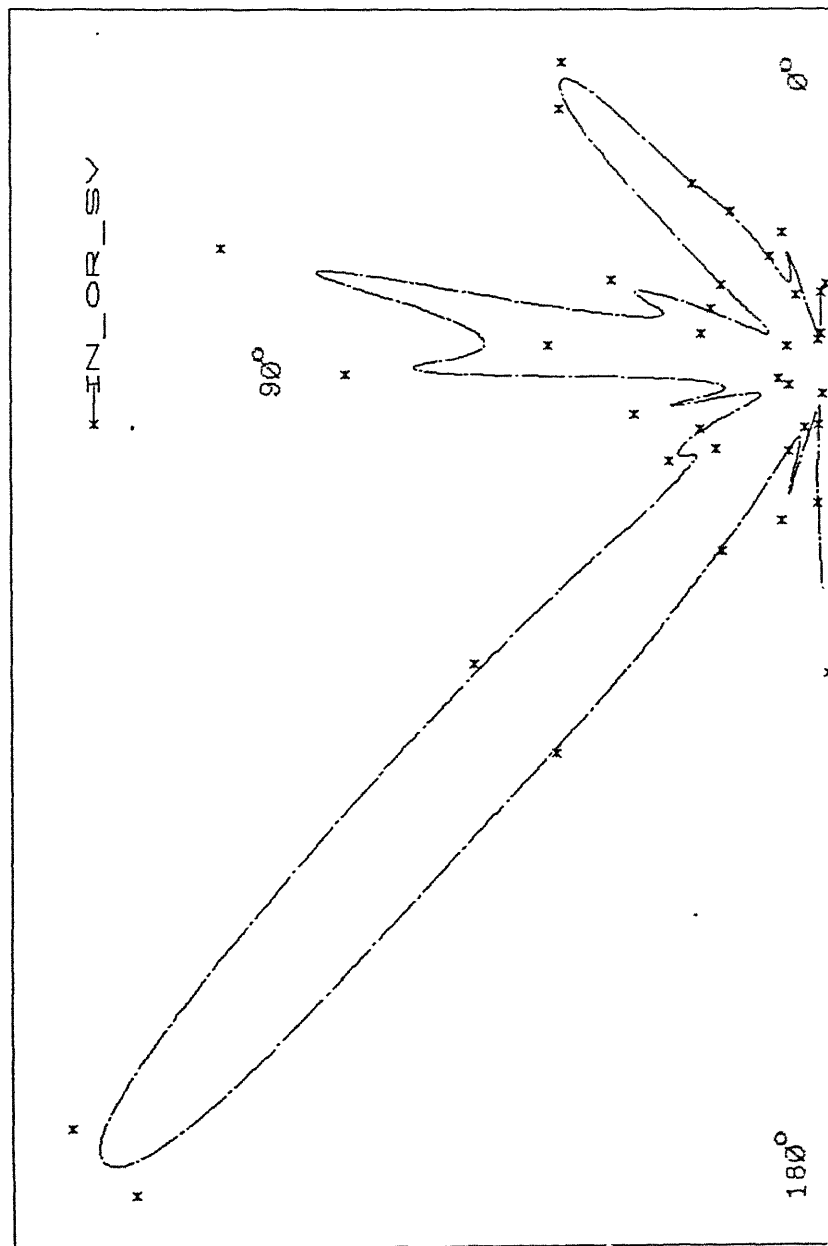


Fig. 4.63 Polar plot of Scattered amplitudes after a Shear wave interacts with an Interface Crack in Layered Structure

## CHAPTER 5

### CONCLUSIONS AND SCOPE FOR FUTURE WORK

#### 5.1 Conclusions

A two-dimensional finite element code has been used to solve the hyperbolic equations governing ultrasonic wave motion and to study the scattering in isotropic (Aluminium) and orthotropic (Graphite/Epoxy) media. A number of simulations have been performed to demonstrate the power of the model in describing the scattering phenomenon by surface and body defects. The "snapshots" of the wave field give insight into the physical process involved. The model can be used to optimize the parameters of a ultrasonic NDT system.

1. A clear picture of the scattered waves by flaws is achieved by subtracting the incident field from the total field.

2. The relation of finite element mesh design dispersion phenomenon of wave propagation is established and its effect was minimised by carefully modelling the flaw free plate domain.

The following conclusions are drawn from the results of isotropic solids:

1. The finite element code is capable of predicting the complex mode conversion of incident waves by surface cracks and body defects. The mode-conversion of Rayleigh wave into a shear and compression waves and their propagation behavior have been exemplified. This understanding of mode- conversion of compression wave by a surface crack helps in the characterization of surface defect.

2. The Rayleigh wave is not clearly seen in the scattered waves by the body defects, this may be due to the less availability of surface area.

3. An estimate of the total energy scattered by the flaws in different directions was made by the differential scattering cross-section. The distribution is seen to be smooth in case of surface cracks and wedge crack. For the case of a hole sharp peak amplitudes were observed in both forward and back-scatter fields, when the wavelength is much larger than the size of the hole. Resonance effect is observed when the wavelength of the input pulse is equal (approx.) to the hole diameter. The effect of wave polarisation on the differential cross-section plots was observed.

A marked difference of the wave scattering in composite material from that of an isotropic material is observed, due to highly anisotropic nature of composite material. The following observations are made for the ultrasonic wave propagation and scattering in orthotropic composite materials:

1. The scattering wave front propagation is clearly seen in the different layers (T-T and L-T; T-T and T-L). It is highly directional dependent. The effect of wave polarisation is also observed.

2. The surface waves in the orthotropic graphite /epoxy is found to be not as prominent as in isotropic media.

3. The complex lobe structure in the different scatter plots helps in detecting the flaw by properly locating the ultrasonic receivers.

## 5.2 SCOPE FOR FUTURE WORK

Future work seems to have a lot of potential, in the following directions :

1. A careful study can be done to find out the transducer parameters like beam steering angle, beam width variation etc.

2. In order to optimise the selection parameters like frequency of pulse etc a study of the variation of scattering cross sections in a particular direction with the variation in the parameter  $ka$  can be done.

3. Efficient absorbing/nonreflecting boundaries should be found to eliminate the spurious reflections from the boundaries. In the investigation of these boundaries one should keep in mind the computational cost and their ease of incorporation into the model.

Other wise, it may be advantageous to combine the boundary element method with the finite element method in an effort to create an optimum hybrid scheme which can be characterised by the FEM solution in the near field and BEM solution for the far field.

4. In the present analysis, the flaws are assumed to be present through out the thickness (because of 2-D plane strain approximation). A three dimensional Finite Element model apart from allowing to model a variety of defects also takes into account their thickness. It also considers the effect of antiplane displacement component  $w$ .

5. The characterisation of the defect/flaw must be done quantitatively to assess its severity as it is an ultimate aim of this work.

6. Laboratory experiments can be carried out using the Ultrasonic scanning equipment in order to validate the results.



3. Efficient absorbing/nonreflecting boundaries should be found to eliminate the spurious reflections from the boundaries. In the investigation of these boundaries one should keep in mind the computational cost and their ease of incorporation into the model.

Other wise, it may be advantageous to combine the boundary element method with the finite element method in an effort to create an optimum hybrid scheme which can be characterised by the FEM solution in the near field and BEM solution for the far field.

4. In the present analysis, the flaws are assumed to be present through out the thickness (because of 2-D plane strain approximation). A three dimensional Finite Element model apart from allowing to model a variety of defects also takes into account their thickness. It also considers the effect of antiplane displacement component  $w$ .

5. The characterisation of the defect/flaw must be done quantitatively to assess its severity as it is an ultimate aim of this work.

6. Laboratory experiments can be carried out using the Ultrasonic scanning equipment in order to validate the results.

## REFERENCES

1. Cantwell, C.J., and Morton, J., "The significance of damage and defects and their detection in Composite Materials", J. Strain Analysis, Vol.27(1), pp 29-42, 1992.
2. Christensen, R.M., "Mechanics of Composite Materials", John Wiley Publications, 1978.
3. Krautkramer, J., and Krautkramer, H., "Ultrasonic testing of materials", Springer-verlag, Fourth edition, 1983.
4. Posakony, G.J., "Engineering aspects of ultrasonic piezoelectric transducer design" in IEEE Ultrasonic symposium proceedings, New York, pp 1-9, 1975.
5. Pao, Y.H., "Elastic waves in solids", J. Appl. Mech., Tr. ASME, Vol.50, pp 1152-1164, 1983.
6. Gubernatis, J.E., "Elastic Waves scattering methods: Assesments and suggestions", In Rev. of progress in Quantitative NDE, 5A, Thompson, D.O., and Chimenti, D.E., eds., Plenum press, NY, pp 21-29, 1986.
7. Bond, L.J., Punjani, M., and Saffari, N., "Ultrasonic Wave propagation and scattering using explicit FDMs", In Math. Modell. in NDT, Blakemore, M., and Georgiou, G.A., eda., Clarendon press, Oxford, pp 81-124, 1988.
8. Coffey, J.M. and Chapman, R.K., "Application of Elastic Wave Scattering Theory for smooth flat cracks to the quantitative prediction of ultrasonic defect detection and sizing", Nuclear Energy, Vol.22, pp 319-331, 1983.
9. Pao, Y.H., and Mow, C.C., "Diffraction of Elastic waves and dynamic stress concentrations", Crane and Russak press, NY, 1973
10. Gubernatis, J.E., Domany, E., Krumhansl, J.A., and Huberman, H., "The Born approximation in the theory of the scattering of elastic waves by flaws", J. Appl. Phys., Vol.48, pp 2812-2819, 1977.
11. Pao, Y.H. and Saches, W., "Theory of Elastic Wave Diffraction I", J. Acoust. Soc. Am., vol.56(5), pp 1478-1486, 1974.
12. Varatharajulu, V. and Pao, Y.H., "Scattering matrix for elastic waves. I Theory", J. Acoust. Soc. Am., Vol.60, pp 556-566, 1976.

13. Visscher, W.M., "A new way to calculate scattering of acoustic and elastic waves 1. They illustrated for scalar waves", J. Appl. Phys., Vol.51, pp825-834, 1980.
14. Achenbach, J.D., Gautesen, A.K., and McMaken, H, "Ray methods for waves in elastic solids-with applications to scattering by cracks", Pitman press, 1982
15. Keller, J.B., "Diffraction by an apperture", J, Appl. Phys, Vol.28, pp 426-444, 1957.
16. Oglivv, J.A., " Ultrasonic beam profile and propagation in an austenitic weld using a theoritical ray tracing model", Ultrasonics, Vol.24, pp 337-347, 1985.
17. Bond, L.J., " Numerical techniques and their use to study wave propagation and scattering - A review", in elastic waves and ultrasonic NDE, Datta, S.K., Achenbach, J.D., and Rajapakse, Y.s., North-Holland, pp 17-27, 1990.
18. Chin, R.C.Y., Hedstrom, G., and Thigpen, L., "Numerical Methods in Seismology", J. Comput. Phys., Vol.54, pp 18-56, 1984.
19. Manolis, G.D., and Bekos, D.E., " Boundary element methods in Elastodynamics", Unwin HYman press, London, 1988.
20. Schafbuch, P.J., Rizzo, F.J., and Thompson, R.B., " BEM solutions for elastic waves scattering in 3D", Int. J. Num. Meth. Eng., Vol.36, pp 436-455, 1993.
21. Hall, W.S., and Robertson, W.H., "BEA of Acoustic wave scattering", in math. meth. in NDT, Blakemore, M., Georgious, G.A., eds., Clarendon press, pp 357-361, 1988.
22. Alterman, Z., and KARal, F.C., " Propagation of elastic waves in layered media by FDM", Bull. Seism. Soc. Ame., Vol.58, pp 367-398, 1968.
23. Boore, D.M., " FDMs for seismic wave propagation in Heterogeneous materials", in methods in computational physics, Bolt, B.A., ed., Academic press, NY, 1972.
24. Blake, R.J., Bond, L.J. and Downie, A.L., "Advances in Numerical Studies of Wave Propagation and scattering", in Review of progress in QNDE. vol.1., Thompson, D.O. and Dale, E.C., ed., pp 157-164, 1981.
25. Sochacki, J., et al, "Absorbing Boundary Conditions and Surface Waves", Geophysics, Vol.52, pp 60-71, 1987.
26. Bond, L., and Saffari, N., "Mode-Conversion Ultrasonic Testing", in Research Techniques in NDE, Vol. 7, Ed. R.S. Sharpe, pp 145-189, 1984.

27. Temple, J.A.G., "Modelling the propagation and scattering of Elastic waves in inhomogeneous and anisotropic media", J. Phys. D:Appl. Phys., Vol.21, pp 859-873, 1988.
28. White, R.M., "Elastic wave scattering at a cylindrical discontinuity in a solid", J. Acoust. Soc. Am., Vol.30, p 771-785, 1958.
29. Kasaburo Harumi, " Computer simulation of ultrasonics in a solid", Materials Evaluation, Vol.44, pp 1086-1110, 1986.
30. Temple, A., and Ogilvy, J.A., " Numerical techniques for wave propagation and scattering in inhomogeneous anisotropic materials", in elastic waves and ultrasonic NDE", Datta, S.K., Achenbach, J.D., Rajapakse, Y.S., eds., North-Holland, 1990.
31. Smith, W.D., " The application of FEA to body wave propagation problems", Geophys. J. R. Astr. Soc., Vol.42, pp 747-768, 1975.
32. Ludwig, R., and Lord, W., " A Finite Element Formulation for the study of ultrasonic NDT systems", IEEE Trans. on Ultrasonics, Ferroelectrics and Frequency control, Vol.35, pp 809-820, 1988.
33. Luidwig, R., Moore, R., and Lord, W., " Transducer models for the Finite Element Simulation of ultrasonic NDT phenomena", in Review of progress in QNDE, Thompson, D.O., and Chimenti, C.E., eds., NY, Plenum press, Vol.6A, pp 649-655, 1987.
34. You, Z., and Lord, W., " Finite Element study of Elastic wave interaction with cracks, in Review of progress in QNDE", Thompson, D.O., and Chimenti, D.E., (editors), NY, Plenum press, Vol.8A, pp 109-116, 1989.
35. Seron, F.J., etal., " Finite Element Method for Elastic wave propagation ", Communications in applied numerical methods, Vol.6, pp 359-368, 1990.
36. You, Z., elal., " Numerical modelling of elastic wave propagation in anisotropic materials", in Review of progress in QNDE", Thompson, D., and Chimenti, C.E., eds., Vol.7A, pp 23-30, 1988.
37. You, Z., and Lord, W., " A Finite Element test bed for diffraction tomography," in Review of progress in QNDE, Thompson, D.O., and Chimenti, C.E., eds., NY, Plenum press, Vol.9, 1991.
38. Jaleel, K.M.A., "Finite Element Modelling of Wave Interactions with Cracks in Composite Materials", M.Tech. Thesis Report, March 1992, IIT Kanpur.
39. Barratt, P.J., and Collins, W.D., "The scattering cross section of an obstacle in an elastic solid for plane harmonic waves", Proc. Camb. Phil. Soc., Vol.61, pp 969-981, 1965.

40. Krenk, S., and Schmidt, H., "Elastic wave scattering by a circular crack", Phil. Trans. R. Soc. Lond., Vol.A308, pp 167-198, 1982.
41. Su, J.H., Vardan, V.V., and Varadan, V.K., "The Unimoment method for elastic wave scattering problems", in Review of progress in QNDEV1, Thompson, D.O., and Chimenti, C.E., eds., pp 137-143, 1981.
42. Goetschel, D.B., Dong, S.B., and Muki, R., "A global local Finite Element Analysis of axisymmetric scattering of elastic waves", J. Appl. Mech., Trns. ASME., Vol.49, pp 816-820, 1982.
43. Karl, F. Graff., "Wave motion in elastic solids", Clarendon press(Oxford), 1975.
44. Achenbach, J.D., "Wave propagation in solids", North-holland, 1970.
45. Musgrave, M.J.P., "Elastic Waves in Anisotropic Media", in Progress in Solid Mechanics Vol. 2, Ed. Sneddon, I.N., and Hill, R.
46. Mal, A.k., and Singh, S.J., "Deformation of Elastic Solids", Prentice Hall Publications, New Jersey, 1991.
47. Hearmon, R.F.S., "An introduction to Applied Anisotropic Elasticity", Oxford University Press, London, 1961.
48. Gubernatis, J.E., Domany, E. and Krumhansl, J.A., "Formal aspects of theory of the scattering of ultrasound by flaws in elastic materials", J. Applied Physics, vol.48, pp 2804 - 2811, 1977.
49. Newmark, N.M., "A method of computation for structural Dynamics", J. Eng. Mech.Div., ASCE, Vol.85, pp 67-94, 1959.
50. Smith, W.D., "A nonreflecting plane boundary for wave propagation problems", J. comp. phys., Vol.15, pp 492-503, 1974.
51. Reynolds, A.C., "Boundary conditions for the numerical solution of wave propagation problems", Geophysics, Vol.43, pp 1099-1110, 1978.
52. Langenberg, K.J. et al, "Numerical Modelling of Ultrasonic Scattering", in Mathematical Modelling in Non-Destructive Testing, Eds. Blakemore, M. and Georgiou, G.A., Clarendon Press, pp 125-174, 1988.
53. Harker, A.H., "Numerical Modelling of the Scattering of Elastic Waves in Plates", J. Nondestructive Evaluation, Vol.4, No.2, pp 89-105, 1984.